INAUGURAL-DISSERTATION
zur Erlangung der Doktorwürde der
Naturwissenschaftlich-Mathematischen
Gesamtfakultät der
Ruprecht-Karls-Universität Heidelberg

vorgelegt von

M. Sc. Yi-Fan Yang

aus Jiangxi, China

Tag der mündlichen Prüfung:

19. Juni. 2020

Electronic States of Fullerene Anions and Endohedral Fullerenes

Gutachter:

Prof. Dr. Dr. h.c. mult. Lorenz S. Cederbaum

Prof. Dr. Jochen Schirmer

This thesis is dedicated to the readers in the future.

Abstract

In recent years, fullerenes, as rising stars in carbon clusters, have been widely applied in various fields of science and technology. The high electron affinity of fullerenes, due to unique geometric and electronic structures, leads to wide applications in many fields, e.g., organic solar cells, supercapacitors, catalyzers, and superconductive materials. Due to the difficulty to synthesize of carbon clusters and to determine their structures experimentally, researchers have paid much attention to the theoretical studies of their geometric and electronic structures. It is only recently that it became possible to apply state-of-the-art theoretical methods, e.g., equation of motion coupled cluster singles and doubles method for electron affinities (EA-EOM-CCSD) to these large molecular systems. With such high cost methods, the full picture of electronic states of the first known fullerene C_{60} has finally been revealed. Study of electronic structures of large molecular systems, such as fullerenes, has become a great challenge for modern theoretical and computational chemistry.

This thesis is devoted to the theoretical study of the electronic states of fullerene anions (e.g., C_{20}^{-}) and fullerene derivatives, utilizing accurate approaches. The latter includes endohedral fullerenes (e.g., Li@C_{20} and Li@C_{60}) and carbon rings (e.g., C_{20}).

To the best of our knowledge, our work is the first study on bound states of the C_{20}^{-} fullerene anion, employing accurate theoretical approaches. We find that the smallest fullerene anion C_{20}^{-}, can form one superatomic and a manifold of valence bound states. It indicates that possessing superatomic bound states is one of the common properties of fullerenes. We hope that this finding sheds light on the study of fullerenes applications in the future. Our theoretically estimated adiabatic electron affinity of the C_{20}^{-} fullerene, is consistent with the electron affinity obtained in the photoelectron experiment. It verifies the validity of the application of high accurate EA-EOM-CCSD method in studying electronic structures of fullerenes.

The endohedral fullerenes, e.g., Li@C_{20} and Li@C_{60}, have attracted great attention due to their enhanced properties compared to the parent fullerenes. Our research on Li@C_{20} shows that the smallest fullerene, i.e., C_{20}, can steal valence electron from the guest Li atom and form a charge separated donor-acceptor system. The Coulomb effect of Li^+ is to stabilize the bound states, both valence and superatomic. Noteworthy, due to their different nature, the stabilizing effect on valence states is stronger than on superatomic states. The extra electron density distribution of superatomic states of the charge separated endohedral system is more compact compared to that of the parent fullerene, while the distribution of valence states does not exhibit this behavior.

Based on our calculations on Li@C_{60}, we have found several excited states. Most of the electronic states are charge separated states, the appearance of Li^+ stabilized the excited states of Li@C_{60} compared to those of the parent isolated anion without changing their characters, similarly to our finding for Li@C_{20}. Importantly, for Li@C_{60} we reported a hitherto unknown non-charge-separated state, which we referred to as the caged-electron state. This state is neither a valence nor a superatomic state, since its extra charge density is mostly distributed at the center of the cage. We demonstrate that the caged-electron state is formed due to the large radius of the C_{60} cage, which reduces the Coulomb attraction effect between Li^+ and the negative carbon cage of the endohedral fullerene. In much larger fullerenes, e.g., Li@C_{180}, this state even becomes the ground state, due to the much weaker Coulomb attraction effect. It is a great example of the impact of the fullerene's size on its electronic structures. Additionally, we have mentioned several possible applications of this new kind of state.

Last but not least, we turn to the carbon ring as the isomer of fullerenes. Carbon rings are intriguing and elegant species, but determining their geometry is an ongoing challenge. We have performed geometry optimization, vibrational frequency calculations and potential energy surface scans, based on EA-EOM-CCSD. Our work reveals that, similar to its fullerene isomer, the C_{20}^- ring can possess several bound states, including one superatomic state. Moreover, our calculation shows a symmetry breaking of the C_{20}^- ring anion structure occurring upon attaching an electron to the neutral ring. The discussion of the possible symmetry breaking mechanisms indicates that the shrinking and distortion of the ring upon electron attachment leading to the symmetry breaking, is a result of the interplay between the symmetry breaking and the totally symmetric modes. The discussion enriches the palette of possible symmetry breaking phenomena in carbon clusters.

Kurzfassung

In den letzten Jahren haben Fullerene, mit ihrer Vorzugsstellung unter den Kohlenstoff-Clustern, vielfältige Anwendungen in unterschiedlichen Wissenschafts- und Technologiefeldern gefunden. Die hohe Elektronenaffinität, als Folge der einzigartigen geometrischen und elektronischen Struktur, eröffnet ein breites Anwendungsspektrum, z.B. in organischen Solarzellen, Katalysatoren, Superkondensatoren und supraleitende Materialien. Angesichts der Schwierigkeit der Synthese von Kohlenstoff-Clustern und einer experimenteller Analyse, kommt theoretischen Untersuchungen ihrer geometrischen und elektronischen Strukturen besondere Bedeutung zu. Erst seit kurzem wurde es möglich, hochentwickelte theoretische Methoden wie z.B. das EA-EOM-CCSD-Verfahren (Equation-Of-Motion Coupled-Cluster Singles and Doubles zur Berechnung von Elektronen-Affinitäten) auf diese großen molekularen Systeme anzuwenden. Mit Hilfe von solch aufwändiger Rechenverfahren konnte ein Gesamtbild der elektronischen Zustände des ersten entdeckten Fullerens, C_{60} , erschlossen werden. Die genaue Behandlung von großen Molekülsystemen wie der Fullerene erweist sich als große Herausforderung für die theoretische und computerbasierte Chemie.

In dieser Arbeit wird eine auf genauer quantenchemischer Berechnung basierende theoretische Untersuchung von Fulleren-Anionen, wie C_{20}^-, und Fulleren-Derivaten vorgelegt, wobei es sich bei letzteren um endohedrale Fullerene, wie $Li@C_{20}$ und $Li@C_{60}$, und Ringe aus Kohlenstoff-Atomen, z.B. C_{20}, handelt.

Die in dieser Arbeit durchgeführte genaue Berechnung der gebundenen Zustände des Fulleren-Anions C_{20}^- ist unseres Wissens die erste derartige Studie überhaupt. Wie sich zeigt, kann das Anion des kleinsten Fullerens einen sogenannten superatomaren Zustand und eine Reihe weiterer Valenz-Zustände ausbilden, die alle elektronisch gebunden sind. Das Auftreten von super-atomaren Zuständen (als Folge induzierter Bildladungen) ist für die Fullerene charakteristisch. Diese Befunde sollten sich, so ist zu hoffen, für zukünftige Anwendungen der

Fullerene klärend erweisen. Der für die adiabatische Elektronenaffinität von C_{20} ermittelte Wert ist in sehr guter Übereinstimmung mit dem experimentellen Ergebnis. Das belegt die Qualität des bei der Berechnung der Elektronen-Struktur der Fullerene eingesetzten EA-EOM-CCSD-Verfahrens.

Endohedrale Fullerene wie $Li@C_{20}$ und $Li@C_{60}$ haben großes Interesse erregt, da diese Systeme Eigenschaften der undotierten Fullerene noch verstärken. Unsere Studie von $Li@C_{20}$ zeigt, dass in diesem kleinsten Fulleren das 2s-Elektron des Lithium-Atoms vom Fulleren "entwendet" wird und sich somit ein ladungsgetrenntes Donor-Akzeptor-System bildet. Dabei stabilisiert die Coulomb-Anziehung des Li^+-Kations die gebunden Zustände, sowohl die Valenz- als auch die superatomaren Zustände, wobei natürlich die Stabilisierung für die Valenz-Zustände größer ist als für die superatomaren Zustände. Die Exzess-Elektronendichte der ladungsgetrennten superatomaren Zustände ist wesentlich kompakter als bei den entsprechenden Zuständen des undotierten Fullerens, während für die Valenz-Zustände kein derartiger Effekt gefunden wird.

Die Rechnungen für $Li@C_{60}$ haben den Grundzustand und angeregte Zustände dieses Systems erschlossen. Bei den meisten Zuständen handelt es sich, wie bei $Li@C_{20}$, um ladungsgetrennte, durch die Wirkung von Li^+ stabilisierte Zustände, vergleichbar mit den Zuständen des C_{60}^--Anions. Höchst bemerkenswert ist das Auftreten eines bisher nicht bekannten Zustands, bei dem keine Ladungstrennung vorliegt, und der entsprechend als Elektronensperr (ES)-Zustand, engl., caged electron state, bezeichnet werden kann. Bei diesem ersten angeregten Zustand von $Li@C_{60}$ ist die Ladungsdichte des zusätzlichen Elektrons, anders als bei den Valenz- und Superatom-Zuständen, im Zentrum des Fulleren-Käfigs verteilt. Dieser Zustand wird möglich, da in dem größeren C_{60}-Gerüst die Coulomb-Wechselwirkung zwischen dem Li^+-Kations und den Elektronen der Kohlenstoff-Atome weniger stark ist. Für noch größere Fullerene, wie $Li@C_{180}$, wird infolge der weiter reduzierten Coulomb-Wechselwirkung der ES-Zustand sogar zum Grundzustand. Das lässt sich als ein Beispiel dafür sehen, wie die Fullerengröße die elektronischen Eigenschaften bestimmt. Mögliche Anwendungen, die sich aus dieser neuen Zustandsart ergeben, werden diskutiert.

Schließlich werden, als Isomere der Fullerene, Ringe aus Kohlenstoff-Atomen betrachtet. Kohlenstoff-Ringe sind faszinierende und ansprechende Gebilde, doch stellt die Ermittlung ihrer räumlichen Anordnung eine anhaltende Herausforderung dar. Unter Einsatz des EA-EOM-CCSD-Verfahrens wurden Geometrieoptimierungen durchgeführt, Schwingungsfrequenzen bestimmt und Punkte auf Energie-Hyperflächen berechnet. Wie die Rechnungen zeigen, weist der C_{20}-Ring, ähnlich wie sein Fulleren-Isomer, eine Reihe elektronisch gebundener Zustände auf, worunter auch ein superatomarer Zustand ist. Darüber hinaus zeigt sich, dass die Anlagerung eines Elektrons an den C_{20}-Ring zu einer Symmetriebrechung der Ringstruktur im C_{20}^{-}-Anion führt. Die genauere Diskussion des Mechanismus der durch Elektronen-Anlagerung bewirkten Verringerung und Verzerrung der Ringstruktur zeigt ein spezifisches Zusammenspiel zwischen symmetriebrechenden und total-symmetrischen Schwingungsmoden. Dieser Befund erweitert die Palette von möglichen Symmetriebrechungs-Phänomenen bei den Kohlenstoff-Clustern.

Contents

Contents

Chapter 1

Introduction

Carbon clusters are clusters formed by carbon atoms only, e.g., fullerenes, carbon chains/rings, graphenes, and carbon nanotubes. As allotropes of carbon, the carbon clusters share some common properties, e.g., ability of accepting extra electrons forming several bound states, ability of encapsulating other atoms, and ability of symmetry breaking. Nowadays, carbon clusters and their derivatives have become the model systems and building blocks of many nanomaterials. However, carbon cluster derivatives are difficult to synthesize. Thus, the theoretical investigation of carbon clusters and their derivatives would be helpful for the developments of their new applications.

The legendary story of fullerenes begins in 1985, when the first fullerene C_{60} was discovered [1]. Now, three decades has pasted, and fullerenes, the simple and complex compounds, have attracted great attentions [2]. They are simple compounds, since they have similar structures formed by carbon atoms only. Moreover, structures of fullerenes are often in high symmetry, i.e., I_h [3] or relatively high symmetry, e.g., D_{5d} [4] and D_{5h} [5]. Due to the symmetry, the structures of fullerenes are much simpler than other carbon clusters. Nevertheless, fullerenes are still complex compounds, due to their rich electronic properties and different sizes. As an example, fullerenes are known as electron-deficient molecules and they can accept an extra electron and form stable anions [6, 7]. Some, like C_{60}, can form a double-charged anion [8]. To the best of our knowledge, small fullerenes like C_{20} cannot form long-lived dianions. To better understand their complicity, a possible approach is to have a closer look at some examples of fullerenes (such as C_{20} and C_{60}), by employing state-of-the-art *ab initio* methods.

When a fullerene molecule accepts one extra electron, it forms a stable singly-charged fullerene anion. The stability results from the fact that this kind of anions possess lower energy than the ground state of the parent fullerenes [9]. In isolated form, stable fullerene anions are difficult to synthesis, control and study, and the theoretical approach is a popular approach to study them [10]. One of the properties of stable fullerene anions interesting researchers is the ability of accepting electrons, described by the electron binding energy (EBE) or electron affinity (EA). Fullerenes are predicted to possess high electron affinities due to their electron-deficient nature. Since the discovery of first fullerene C_{60}, a competition has started between researchers, to accurately compute electron affinities of fullerenes, employing density function theory (DFT) [11-13] and first-principles many-body theories [14, 15]. The error of DFT or first principles results compared to experiment can be more than 0.4 eV. One can reduce the error, if proper *ab initio* methods are employed along with proper basis sets. However, applying *ab initio* method, especially post-Hartree-Fock methods to such large molecules (such as fullerenes) are still very challenging, in particular, due to high and often prohibitively high computational cost [16]. In this thesis, we will show our attempts of applying accurate *ab initio* methods to large carbon clusters, such as fullerenes.

Fullerenes not only have large electron affinities but also have the ability to form several bound electronic states [17]. Most of these bound states are so-called valence states, which bind the extra electron on the carbon cage. Interestingly, another type of bound states can also be supported by fullerenes, a fact which was unrevealed until 2008 [18]. The highest occupied molecular orbital of this kind bound state is referred to as superatom molecular orbital (SAMO). SAMO is ‘elegant’ diffuse orbital describing an extra electron which is mostly distributed outside the carbon cage. Despite its beauty, it also has promising applications in several fields, such as charge transfer [19], which encourages researchers to understand its nature.

Due to their diffuse nature, the bound states corresponding to SAMOs can be mistaken to be Rydberg states [20]. However, these states are different from typical Rydberg states, since considerable amount of the extra electron is located in the middle of the cages. It is because of the hollow space inside the fullerene cages, which provides image charge and potentials forming a SAMO [18]. Hence, SAMO is a universal property with sufficient hollow space forming a cage [21].

Interestingly, researchers have also found SAMO in carbon nanotubes [22]. However, the question arises whether small fullerenes, such as C_{20}, can support a SAMO? We will answer this question in chapter 3.

Fullerene anions are not the only derivatives of neutral fullerenes. By definition, all fullerenes are cages formed by carbon only. Naturally, one may wonder whether such a cage cluster has the ability to encapsulate any atoms in the space inside cage. Since the discovery of La@C_{60} in 1985 [23], researchers have synthesized an expanded family of those compounds and named them *endohedral* fullerenes [24]. This term originates from the Greek words "*endo*" (within) and "*hedra*" (face of a geometrical figure). Nowadays, as one of the most important derivatives of fullerenes, endohedral fullerenes have been applied to broad range of fields, e.g., organic photovoltaic devices [25], catalyzer [26] and biological and medical fields [27].

Among the growing endohedral fullerene family, we are particularly interested in the alkali endohedral fullerenes. Alkali atoms have low ionized potentials (IP) [28], indicating that their valence electrons can ionize easily. Meanwhile, as mentioned above, one of the well-known properties of fullerenes is their high electron affinities. When one injects an alkali atom into a fullerene cage, they will play the role of electron donor and acceptor, respectively, resulting in a donor-acceptor (DA) system [29]. Due to the loss of a valence electron, the alkali atom becomes positive, and the fullerene is negative charged. This kind of electronic states are referred to as charge separated (CS) states [30]. Apart from the wide range of applications of charge separated states [31], we are interested in the impact the extra positive charge of guest alkali cation (Lithium, as an example) exerts on the valence and superatom molecular orbitals of the now negatively charged fullerene cage. Unlike counterparts in their parent fullerenes, in Li endohedral fullerenes, there is a complex effect arising from the combination of image and real charge at the interior of the fullerenes. The respective change of the valence and superatom molecular orbitals compared to those in parent fullerenes is an interesting and rich topic.

In some endohedral fullerenes, e.g., alkaline earth atoms as guest atoms (Ca@C_{60}) [32], the valence electrons cannot fully migrate to the fullerene cage and different types of charge separated states arise. This is due to the high second IP of alkaline earth atoms and the low second EA of C_{60}. In the case of alkali endohedral fullerenes (such as $Li@C_{60}$), due to the low first IP, it has been well accepted that all the states of neutral $Li@C_{60}$ are charge separated states. However, at the center of the cage, the Coulomb attraction between the positive charge on the alkali and negative charge on the cage decreases with radius of cage, while the electron affinities of fullerenes increase only slowly [33]. With increasing the fullerene radius, the ability of the fullerene to strip off an electron from the guest atom would decrease. For large endohedral fullerenes, it may thus become possible that the charge separated states are not those favored in energy. In chapter 5, we will present our theoretical computational results for this state in Li endohedral fullerenes, referred to as caged-electron state. We indeed find a new kind of state which we named caged-electron state. To the best of our knowledge, this kind of novel low-lying non-charge-separated states of alkaline endohedral fullerenes have not been reported before.

Among all carbon allotropies, the carbon ring family is a tricky but interesting topic. Symmetry breaking effects, such as the Jahn-Teller effect or vibronic coupling effects, play the important role in determining the geometry of carbon clusters with high symmetry, including fullerenes and carbon rings [34-37]. Additionally, due to high reactivity of carbon rings, isolation or structural characterization of carbon rings is difficult. Only recently, carbon rings C_{18} have been synthesized and structure determined experimentally [38]. Thus, a high level theoretical approach is currently more favorable for the study of carbon rings. As carbon rings are planar molecules, even number carbon rings C_m can be classified as m=4n+2 and m=4n families, where n is a natural number. The former family is predicted to possess aromaticity, as rings in this form satisfy Hückel's rule, a matter which attracted great attention. The latter family lacks aromaticity. To fulfill the requirement of four bonds per carbon atom, the ring can be either polyynic (with alternate single and triple bonds) or cumulenic (with only double bonds), resulting in $D_{n/2h}$ symmetry or D_{nh} symmetry. There are several discussions in the literature, including both theoretical and experimental reports on the geometry of C_m rings, and most claim that the polyynic form is energetically favorable providing $D_{n/2h}$ symmetry for antiaromatic or nonaromatic carbon rings [38-41]. However, one still cannot safely draw the conclusion that $D_{n/2h}$ symmetry is the symmetry of carbon ring molecules and anions. For instance, due to vibronic coupling effect of the extra electron of ring anions, there might be a symmetry breaking resulting in lower symmetry, e.g., $C_{n/2h}$ symmetry [37]. Investigating the symmetry breaking of ring anions by employing high level computations, would enrich our knowledge of carbon clusters and shade light on the process of symmetry breaking in other anions.

The thesis is organized as follows. In chapter 2, we will have a short overview of the *ab initio* methods utilized in this thesis. Those methods provide accurate description of correlation effects to the electronic states, which are helpful in the case of studying valence and superatom molecular orbitals. In chapter 3, we present our results on the bound states of smallest fullerene anion C_{20}^{-}. We will show that even the smallest fullerene C_{20}^{-} anion can form bound states corresponding to SAMO as well as several valence bound states. In chapter 4, the study of charge separated states of Li@C_{20} are investigated. The results support the idea that the positive charge of guest cation stabilizes the valence CS states considerably while having only little effect to superatomic CS states. In chapter 5, an interesting hitherto unknown low-lying non-charge-separated state of Li@C_{60} is identified and discussed. It is unique as the charge is mostly distributed at the center of the endohedral fullerenes. It is demonstrated that this new kind of state can be the ground state and indicates promising applications. In chapter 6, we exhibit our results of symmetry breaking research on the C_{20}^{-} ring anion. It is interesting to see how one extra electron can change the structure of the ring and to show excited states of the anion. Finally, in chapter 7 we have a short outlook of future research in carbon clusters, summarizing our results and concluding.

Chapter 2

Theoretical Methodology

By definition, bound (stable) anions are energetically lower than their neutral molecule counterparts on the potential energy surface (PES). To obtain reliably such small binding energies, one needs state-of-the-art methods to calculate the energies of both the anions and the molecules. The coupled cluster (CC) method [42], as one of the most successful wavefunction approximations for many electron systems, is suitable for the calculation of ground states. Its robustness and size-consistency establishes its potential for application to middle size molecules (10-20 atoms) and even larger size molecules with high symmetry, such as, C_{60} with I_h symmetry. However, for the excited states of anions, especially open-shell anions, the traditional coupled cluster method is not adequate. In those cases, one can employ *the equation of motion coupled cluster for electron affinities* (EA-EOM-CC) [43], using closed-shell states as reference states.

This section is organized as follows. The core concepts of the *Schrödinger equation* [44], the *Born-Oppenheimer* approximation [45], and *second quantization* [46] are introduced in section 2.1. A short overview of the fundamental *Hartree-Fock* (HF) approximation [47] and *configuration interaction* (CI) method [48] is given in section 2.2. As an alternative approach to CI, *coupled cluster* theory is described in section 2.3. As a method based on coupled cluster wavefunctions, the *equation of motion coupled cluster for electron affinity* (EA-EOM-CC) method is described in section 2.4. One of the applications of CC methods, i.e., analytical energy gradient, is described in section 2.5.

Chapter 2

2.1 Basic concepts of quantum chemistry

2.1.1 The Schrödinger equation

For the bound anions and the parent molecules, time-independent Schrödinger equation is appropriate, as these states are stationary states with properties independent of time. The time-independent Schrödinger equation is

$$\hat{H}\psi(\mathbf{r}) = \mathrm{E}\psi(\mathbf{r}) \tag{2.1}$$

where $\psi(\boldsymbol{r})$ is time-independent wavefunction and $\hat{H}$ is the Hamiltonian. In Eq. (2.1) **r** stands collectively for the coordinates of the system.

The Hamiltonian for a system with N electrons and M nuclei includes the kinetic energy of electrons and nuclei, as well as repulsion effect between electrons and nuclei. The Hamiltonian in atomic units reads

$$\hat{H} = -\frac{1}{2}\sum_{i=1}^{M}\nabla_i^2 - \sum_{a=1}^{M}\frac{1}{2M_a}\nabla_a^2 + \sum_{i=1}^{N}\sum_{j>i}^{N}\frac{1}{r_{ij}} + \sum_{a=1}^{M}\sum_{b>a}^{M}\frac{Z_a Z_b}{R_{ab}} - \sum_{i=1}^{N}\sum_{a=1}^{M}\frac{Z_a}{r_{ia}} \tag{2.2}$$

where ∇_i^2 and ∇_a^2 denote the Laplace operators for the electrons and nuclei, respectively. M_a and Z_a are the mass and charge, respectively, of corresponding nucleus. The third and fourth term stand for the Coulomb repulsion of electrons and nuclei, respectively. The last term is the operator for Coulomb attraction between electrons and nuclei. r_{ij}, r_{ia} and R_{ab} are short-hand notations $r_{ij} = |\boldsymbol{r_i} - \boldsymbol{r_j}|$, $r_{ia} = |\boldsymbol{r_i} - \boldsymbol{R}_a|$, and $R_{ab} = |\boldsymbol{R}_a - \boldsymbol{R}_b|$.

An anti-symmetrized product of state wavefunctions can be also written in the form of a determinant. It is by definition possess antisymmetric, and it is referred to as *Slater determinant*,

$$\Psi_{\boldsymbol{q_1}\ldots\boldsymbol{q_N}}(\boldsymbol{\zeta_1}\boldsymbol{\zeta_2}\ldots\boldsymbol{\zeta_N}) = \frac{1}{\sqrt{N!}}\begin{vmatrix} \psi_{q_1}(\boldsymbol{\zeta_1})\,\psi_{q_1}(\boldsymbol{\zeta_2})\ldots\psi_{q_1}(\boldsymbol{\zeta_N}) \\ \psi_{q_2}(\boldsymbol{\zeta_1})\,\psi_{q_2}(\boldsymbol{\zeta_2})\ldots\psi_{q_2}(\boldsymbol{\zeta_N}) \\ \ldots \\ \psi_{q_N}(\boldsymbol{\zeta_1})\,\psi_{q_N}(\boldsymbol{\zeta_2})\ldots\psi_{q_N}(\boldsymbol{\zeta_N}) \end{vmatrix} \tag{2.3}$$

One can also write this determinant in the shorthand notation form,

$$\Psi_{q_1 \dots q_N}(\zeta_1 \zeta_2 \dots \zeta_N) = \left| \psi_{q_1}(\zeta_1)\, \psi_{q_2}(\zeta_2) \dots \psi_{q_N}(\zeta_N) \right| \tag{2.4}$$

here $\boldsymbol{\zeta_i} \equiv \mathbf{r}_i \sigma_i$ comprises both the spatial and spin coordinates of the i-th electron.

2.1.2 Born-Oppenheimer approximation

According to Eq. (2.2), the Hamiltonian is of the form,

$$\hat{H} = \hat{T}_e + \hat{T}_n + \hat{V}_{ee} + \hat{V}_{en} + \hat{V}_{nn} \tag{2.5}$$

Where the $\hat{V}_{ee}$, $\hat{V}_{en}$, $\hat{V}_{nn}$ terms stand for the electron-electron, electron-nuclei, and nuclei-nuclei interactions, respectively. Moreover, $\hat{T}_e$ and $\hat{T}_n$ are the kinetic energy operators for the electrons and nuclei, respectively.

Due to the much faster velocities of the electrons than those of the nuclei, the electron wavefunction can always adapt to the motion of the nuclei, so that the nuclear positions R can be treated as parameters in the electron wavefunction $\Psi_m^e(\boldsymbol{r}; \boldsymbol{R})$. To solve the Schrödinger equation for both the electronic and nuclear degrees of freedom, one can invoke the *Born-Oppenheimer* approximation in which the total wavefunction can be written as the product.

$$\Psi_{mv}(\boldsymbol{r}, \boldsymbol{R}) = \Psi_m^e(\boldsymbol{r}; \boldsymbol{R}) \cdot \chi_{mv}(\boldsymbol{R}) \tag{2.6}$$

where $\Psi_m^e(\boldsymbol{r}; \boldsymbol{R})$ is solution of the electronic *Schrödinger equation* (for a given nuclear conformation **R**) and $\chi_{mv}(\boldsymbol{R})$ is the nuclear wavefunctions.

With the Hamiltonian in Eq. (2.5) and wavefunction in Eq. (2.6), the time-independent electronic *Schrödinger equation* can be written as

$$\hat{H}_e \Psi_m^e(\boldsymbol{r}; \boldsymbol{R}) = \left(\hat{T}_e + \hat{V}_{ee} + \hat{V}_{en} + \hat{V}_{nn}\right) \Psi_m^e(\boldsymbol{r}; \boldsymbol{R}) = W_m(\boldsymbol{R}) \Psi_m^e(\boldsymbol{r}; \boldsymbol{R}) \tag{2.7}$$

where $W_m(\boldsymbol{R})$ is the energy of the m-th state as a function of the nuclear coordinates.

Using the ansatz Eq. (2.6) and Eq. (2.7) in the total *Schrödinger equation*,

$$\hat{H} \Psi_{mv}(\boldsymbol{r}, \boldsymbol{R}) = E_{mv} \Psi_{mv}(\boldsymbol{r}, \boldsymbol{R}) \tag{2.8a}$$

gives

$$\left(\hat{T}_n + \hat{H}_e\right)\Psi_m^e(\boldsymbol{r};\boldsymbol{R})\chi_{mv}(\boldsymbol{R}) = \left(\hat{T}_n + W_m(\boldsymbol{R})\right)\Psi_m^e(\boldsymbol{r};\boldsymbol{R})\chi_{mv}(\boldsymbol{R}) = E_{mv}\Psi_m^e(\boldsymbol{r};\boldsymbol{R})\chi_{mv}(\boldsymbol{R}) \quad (2.8b)$$

Neglecting in Eq. (2.8b) derivatives of the electronic wave function with respect to the nuclear coordinates, that is,

$$\frac{\partial}{\partial R}\Psi_m^e(\boldsymbol{r};\boldsymbol{R}) = 0$$

the *Schrödinger equation*,

$$\left(\hat{T}_n + W_m(\boldsymbol{R})\right)\Psi_{mv}(\boldsymbol{R}) = E_{mv}\Psi_{mv}(\boldsymbol{R}) \quad (2.9)$$

for the nuclear motion in the electronic state m is obtained. Here the energy $W_m(\boldsymbol{R})$ establishes the potential energy for the nuclear motion.

The Born-Oppenheimer approximation can reduce the cost of computation by employing fixed nuclear coordinates **R** and simplify the equations by reducing the degrees of freedom. This ansatz is valid in most cases. However, if potential energy surfaces get close to each other or even intersect, forming a conical intersection, the Born-Oppenheimer approximation may become poor or even break down completely [49]. We will discuss one example in Chapter 6.

2.1.3 Second quantization

The so-called *second quantization* notation is widely used in the field of many-body quantum chemistry. Comparing to a wave function notation in terms of Slater determinants, second quantization has a great advantage, as it can transfer the anti-symmetry property onto algebraic properties. Moreover, the application of creation and annihilation operators simplifies the notations of states and operators. In quantum field theory, researchers originally introduced the electron creation and annihilation operators for the phenomenon with actual creation or destruction of particles. In chemistry, those creation and annihilation operators are employed for convenient and practical device. Unlike wavefunctions, second quantization is not restricted to a given number of electrons. Thus, it is an elegant tool for quantum chemistry.

In second quantization notations, a state corresponding to an N-electron slater determinant with N electrons can be written as

$$|\boldsymbol{q}\rangle = |q_1, q_2 \dots q_N\rangle = \hat{a}^+_{q_N} \dots \hat{a}^+_{q_1}|\emptyset\rangle \tag{2.10}$$

where $\hat{a}^+_q$ is a creation operator associated with the one-particle state φ_q and $|\emptyset\rangle$ denotes the vacuum state (zero particle).

The creation operator is defined by their action

$$\hat{a}^+_q|\boldsymbol{q}\rangle = \hat{a}^+_q|q_1, q_2 \dots q_N\rangle = |q_1, q_2 \dots q_N, q\rangle \tag{2.11}$$

on basis states Slater determinants of 0, 1, 2, … electrons.

To each creation operator $\hat{a}^+_q$ there is an annihilation operator $\hat{a}_q$ defined as the Hermitian conjugate

$$\hat{a}_q = (\hat{a}^+_q)^+ \tag{2.12}$$

According to

$$\hat{a}_q|\boldsymbol{q}\rangle = \hat{a}_q|q_1, q_2 \dots q_N\rangle = \delta_{qq_N}|q_1, q_2 \dots q_{N-1}\rangle - \delta_{qq_{N-1}}|q_1, q_2 \dots q_{N-2}, q_N\rangle + \cdots \tag{2.13}$$

The annihilation operator removes the orbital q from the product state if the orbital φ_q is contained in the product.

For arbitrary creation and annihilation operators, there is anticommutation relation,

$$\{\hat{a}^+_p, \hat{a}_q\} = \hat{a}^+_p\hat{a}_q + \hat{a}_q\hat{a}^+_p = \delta_{pq} \tag{2.14}$$

where δ is the Kronecker delta.

The creation and annihilation operator also simplify the notation of operators. In second quantization, a *one-electron* $\hat{T}$ and a *two-electron* $\hat{G}$ operators can be written in the following forms respectively,

$$\hat{T} = \sum_{pr} t_{pr}\hat{a}^+_p\hat{a}_r \tag{2.15}$$

where,

$$t_{pr} = \langle\varphi_p|\hat{t}|\varphi_r\rangle = \sum_{\sigma}\int d\boldsymbol{r}\varphi^*_p(\boldsymbol{r},\sigma)\varphi_r(\boldsymbol{r},\sigma)$$

and,

$$\hat{G} = \frac{1}{2}\sum_{pqrs} g_{pqrs}\hat{a}_p^+\hat{a}_q^+\hat{a}_s\hat{a}_r \tag{2.16}$$

where,

$$g_{pqrs} = \sum_{\sigma,\sigma'}\iint \frac{d\boldsymbol{r}\,d\boldsymbol{r}'}{|\boldsymbol{r}-\boldsymbol{r}'|}\varphi_p^*(\boldsymbol{r},\sigma)\varphi_r(\boldsymbol{r},\sigma)\varphi_q^*(\boldsymbol{r},\sigma')\varphi_s(\boldsymbol{r},\sigma')$$

In second quantization the molecular electronic Hamiltonian reads,

$$\hat{H} = \sum_{rs} t_{rs}\hat{a}_r^+\hat{a}_s + \frac{1}{2}\sum_{pqrs} g_{pqrs}\hat{a}_p^+\hat{a}_q^+\hat{a}_s\hat{a}_r \tag{2.17}$$

where t_{rs} are the matrix elements of the one-particle part of the Hamiltonian Eq. (2.2) comprising the kinetic energy of the electrons and the electron-nuclei attraction, and g_{pqrs} are the two-electron Coulomb integral.

In the following sections, we will describe Hartree-Fock, configuration interaction and coupled cluster methods with the second quantization notations.

2.2 Hartree-Fock and Configuration Interaction methods

In this section, we give a short overview of the Hartree-Fock (HF) approximation and the configuration interaction (CI) method. HF is the lowest-cost and simplest wavefunction approximation for many-electron system. It can be applied to systems with hundreds of atoms without too much of computational cost. It is a simple approximation, establishing the one-particle picture and providing the starting point for more elaborated methods, such as, configuration interaction, and coupled cluster method.

In principle, configuration interaction provides exact solutions to the many-electron Schrödinger equation within a given basis. Usually we apply approximations by truncating the CI expansion manifold for excited state calculations. The full configuration interaction (FCI) can reach the limit of the space spanned by the single-particle basis sets. It is a highly reliable method and its result can be used as benchmark energies to evaluate other methods, especially other post-HF methods. However, due to its high cost of computation resources, the applications of FCI is still limited to small molecules and ions.

2.2.1 Hartree-Fock approximation

In the HF approximation, an N electron system is described by a single Slater determinant.

$$|\Phi_0\rangle = |\varphi_1\varphi_2 \dots \varphi_N\rangle \tag{2.18}$$

where, $|\varphi_i\rangle$, i=1,2,…N, represent the N energetically lowest spin orbitals. The energy of this state is,

$$E_0^{HF} = \langle\Phi_0|\hat{H}|\Phi_0\rangle = \sum_k^N \langle k|\hat{t}|k\rangle + \frac{1}{2}\sum_{kl}^N g_{klkl} - \frac{1}{2}\sum_{kl}^N g_{kllk} \tag{2.19}$$

where,

$$\hat{t} = -\frac{1}{2}\nabla^2 - \sum_A \frac{Z_A}{|\boldsymbol{r} - \boldsymbol{R}_a|} \tag{2.20}$$

is the one-electron Hamiltonian corresponding to the kinetic energy and the electron-nuclear attraction.

The HF equations are obtained by choosing the orbitals such that E_0^{HF} is minimal under the constraints, that the orbitals are orthogonal, $\langle\varphi_i|\varphi_j\rangle = \delta_{ij}$.

This leads to the eigenvalue problem

$$\hat{f}\varphi_k = \varepsilon_k\varphi_k, \qquad k = 1,2,\dots \tag{2.21a}$$

where $\hat{f}$ is a one particle operator, referred to as *Fock operator*. In spin-free form $\hat{f}$ is given by

$$\hat{f} = -\frac{1}{2}\nabla^2 - \sum_a \frac{Z_A}{|\boldsymbol{r} - \boldsymbol{R}_a|} + \sum_{\mathrm{i}}^{\frac{\mathrm{N}}{2}}\left(2\hat{\mathrm{J}}_{\mathrm{i}} - \hat{\mathrm{K}}_{\mathrm{i}}\right) \tag{2.21b}$$

where $\hat{\mathrm{J}}_{\mathrm{i}}$ and $\hat{\mathrm{K}}_{\mathrm{i}}$ are the Coulomb and exchange operator for the orbital φ_i, respectively. The Coulomb operator results from the electron-electron repulsion between electrons. The exchange operator reflects the anti-symmetry of the electronic wavefunction.

Now we introduce linear combination of atomic orbitals (LCAO),

$$\varphi_i(\boldsymbol{r}) = \sum_{\nu} c_{\nu_i} \chi_{\nu}(\boldsymbol{r}) \tag{2.22}$$

in which the molecular orbitals are expanded as linear combinations of atomic basis functions, $\chi_{\nu}(\boldsymbol{r})$.

With this ansatz, the Hartree-Fock equations (2.21a) can be written as an algebraic eigenvalue problem,

$$\boldsymbol{Fc} = \boldsymbol{ESc} \tag{2.23}$$

where **F** is the matrix representation of Fock operator, with elements $F_{\mu\nu} = \langle \chi_\mu | \hat{f} | \chi_\nu \rangle$. **E** is the diagonal matrix of orbital energies. In the overlap matrix **S**, the elements are $S_{\mu\nu} = \langle \chi_\mu | \chi_\nu \rangle$. **c** is the matrix of expansion coefficients.

The Fock operator depends on the occupied orbitals via $\hat{\mathrm{J}}_{\mathrm{i}}$ and $\hat{\mathrm{K}}_{\mathrm{i}}$, so that Eq. (2.21a) and Eq. (2.21b) establish a fixed-point iteration scheme. By using an iterative procedure, one can solve Eq. (2.21a) repeatedly and obtain upon convergence the HF orbitals, the orbital energies and via Eq. (2.19) the HF energy.

The original HF approximation is formulated for the ground state. One can still calculate the properties of excited states (such as excitation energies). By exchanging the occupied orbitals with virtual orbitals, $|\Phi_{ak}\rangle = \hat{a}_a^{+} \hat{a}_k |\Phi_0\rangle$, one can describe target excited states in zeroth order, and their energies through first order by employing this Slater determinant. One may also apply the SCF procedure to selected excited states, freezing here the occupation numbers according to an initial Slater determinant. Thereby, one can obtain excited energies by calculating the energy differences between target states and the ground state. The procedure including two SCF calculations is referred to as ΔSCF [50, 51]. We will apply this procedure in Chapter 5.

The energy difference between the HF energy and the exact energy for a given basis is the correlation energy.

$$E_{corr} = E_{HF} - E_{exact} \tag{2.24}$$

To obtain accurate correlation energy, post-HF methods employing the HF wavefunction as reference wavefunction have been developed, i.e., configuration interaction and coupled cluster theory. By increasing the LCAO basis sets, one can extrapolate to the so-called HF limit, which is the HF approximation for a complete basis set.

2.2.2 Configuration interaction method

The electronic wave function in the CI approach is given as a linear combination of all possible determinants, including the ground state and excited states determinants.

$$|\Psi\rangle = \sum_{I} C_I|\Phi_I\rangle = C_0|\Phi_0\rangle + \left(\frac{1}{1!}\right)^2 \sum_{ai} c_i^a \hat{a}_a^+ \hat{a}_i|\Phi_0\rangle + \left(\frac{1}{2!}\right)^2 \sum_{abij} c_{ij}^{ab} \hat{a}_a^+ \hat{a}_i \hat{a}_b^+ \hat{a}_j|\Phi_0\rangle + \cdots \tag{2.25}$$

Here, $|\Phi_0\rangle$ is the reference wavefunction, usually obtained from HF calculations. The second term and third term are single and double excited determinants, respectively. The factor $\left(\frac{1}{n!}\right)^2$ accounts for repetitions of the same excitations in Eq. (2.25). Here the indices i, j, k,… and a, b, c,… refer to occupied and unoccupied orbitals with respect to the HF reference state $|\Phi_0\rangle$.

A single reference configuration often dominates the CI wavefunction. For the ground state, usually it is the Hartree-Fock ground state.

By applying the variational principle, one can optimize the expectation value of the N electron system with suitable coefficients.

$$E = min\frac{\langle\Psi|\hat{H}|\Psi\rangle}{\langle\Psi|\Psi\rangle} \tag{2.26}$$

The eigenvalue equation for CI takes on the form,

$$\boldsymbol{HX} = \boldsymbol{XE} \tag{2.27}$$

where the elements of Hamilton matrix are $H_{IJ} = \langle\phi_I|\hat{H}|\phi_J\rangle$. $\boldsymbol{X}$ is the matrix of the eigenvectors, satisfying the orthonormalization conditions $\boldsymbol{X}^+\boldsymbol{X} = \mathbf{1}$, and $\mathbf{E}$ is the diagonal matrix of eigenvalues.

Due to the limitation of computational resources, in actual applications a truncated CI expansion has to be used.

According to *Brillouin's Theorem*, singly excited determinants $a_a^+ a_i|\Phi_0\rangle$ cannot directly couple to the HF reference state. Thus, the simplest truncated CI model for the ground state is configuration interaction doubles (CID) expansion,

$$|\Psi_0^{CID}\rangle = [1 + \left(\frac{1}{2!}\right)^2 \sum_{abij} c_{ij}^{ab} \hat{a}_a^+ \hat{a}_i \hat{a}_b^+ \hat{a}_j]|\Phi_0\rangle \tag{2.28}$$

Here the CI eigenvalue equation takes on the form,

$$\begin{pmatrix} E_0^{HF} & \boldsymbol{A} \\ \boldsymbol{A}^+ & \boldsymbol{B} \end{pmatrix} \begin{pmatrix} 1 \\ \boldsymbol{c} \end{pmatrix} = E_0^{CID} \begin{pmatrix} 1 \\ \boldsymbol{c} \end{pmatrix} \tag{2.29}$$

where $E_0^{HF} = \langle \phi_0 | \hat{H} | \phi_0 \rangle$ is the HF energy of ground state. $\boldsymbol{A}$ is a row vector of elements $\langle \Phi_0 | \hat{H} \hat{a}_a^+ \hat{a}_i \hat{a}_b^+ \hat{a}_j | \Phi_0 \rangle$ and B is a matrix of elements $\langle \Phi_0 | \hat{a}_i^+ \hat{a}_a \hat{a}_j^+ \hat{a}_b \hat{H} \hat{a}_c^+ \hat{a}_k \hat{a}_d^+ \hat{a}_l | \Phi_0 \rangle$.

Eq. (2.29), leads to the implicit equation

$$E_{corr}^{CID} = E_0^{HF} - E^{CID} = -\boldsymbol{A}(E_0^{CID}\boldsymbol{1} - \boldsymbol{B})^{-1}\boldsymbol{A}^+ \approx -\boldsymbol{A}(\boldsymbol{1}E_0^{HF} - \boldsymbol{B})^{-1}\boldsymbol{A}^+ \tag{2.30}$$

for the correlation energy, which can be approximated as in the last term on the right hand side.

For excited states calculations, CID is not appropriate, since here the single excited determinants become the dominant contributions. Here, the simplest approximation is configuration interaction singles (CIS)

$$|\Psi^{CIS}\rangle = c_0|\Phi_0\rangle + \sum_{ai} c_i^a \hat{a}_a^+ \hat{a}_i |\Phi_0\rangle \tag{2.31}$$

The standard model of CI for quantum chemistry computations is configuration interaction singles and doubles (CISD). The configuration space comprises the 1p-1h states, $\hat{a}_a^+ \hat{a}_i |\Phi_0\rangle$ and the 2p-2h states, $\hat{a}_a^+ \hat{a}_i \hat{a}_b^+ \hat{a}_j |\Phi_0\rangle$. However, it is not *size-extensive* for the ground states, which undermines its applicability for large molecule systems. For excited states, the CISD is not accurate enough due to the absence of the triple excitations.

In practice, different determinants may be dominant in different regions of the molecular PES, such as near conical intersections. Single reference methods may fail when there are two or more dominant configurations in the ground-state expansion. In those cases, one can turn to *multireference configuration interaction* (MRCI) method, e.g., MRCI with *active space* ansatz [52, 53]. As a multi-reference method, MRCI is computationally more costly than single reference methods, which restricts its applications to large molecules. As an alternative method, traditional CC for ground states and EOM-CC for excited states can be employed to study conical intersection problems, as a single-reference methods with lower cost than multi-reference methods [54].

2.3 Coupled cluster theory for ground state

Nowadays, the most accurate and widely applied post-HF method is the coupled cluster theory. With the developing of theory, software and computational resources, the coupled cluster method can be applied to large closed-shell systems with hundreds of atoms, e.g., single-walled carbon nanotubes [55, 56]. Comparing to the CI method, e.g., CISD, traditional CC method (such as coupled cluster with singles and doubles CCSD [57]) is *size-extensive*. A size-extensive method provides results for total energies that scale linearly with the size of the system [58]. This property assures that the quality of the results is independent from the size of the system, which establishes its importance in the application to large molecules and ions.

CCSD also has better performance in treating the correlation effect than CISD, which will be discussed in the following section. Moreover, Pople and co-workers [59] suggested an augmented technique which can significantly improve the CCSD results. This augmented CC method is named CCSD(T) and employs a perturbative consideration of the triple excitations in the interaction with both singles and doubles from CCSD. Due to its outstanding accuracy, it is accepted as “gold standard” in quantum chemistry [60-63]. However, applying CCSD(T) to large molecular systems is still unfeasible due to the high computational cost. In the computations on the large anions reported in this thesis, only the CCSD method could be applied.

2.3.1 Ansatz of the coupled cluster method

Now we turn to the coupled cluster approximation. Here we introduce an operator $\widehat{K}$, which converts the zero-order wavefunction Φ_0 to the exact wavefunction Ψ_0,

$$\Psi_0 = \widehat{K}\Phi_0 \tag{2.32}$$

using the exponential ansatz,

$$\widehat{K} = e^{\hat{T}} \tag{2.33}$$

here $\hat{T}$ denotes the sum of excitation operators,

$$\hat{T} = \hat{T}_1 + \hat{T}_2 + \hat{T}_3 \ldots \tag{2.34}$$

where the operators $\hat{T}_1$, $\hat{T}_2$, $\hat{T}_3 \ldots$ are single, double, triple, … excitation operators of the form,

$$\hat{T}_1 = \sum_{ai} t_i^a (\hat{a}_a^+ \hat{a}_i) \tag{2.35}$$

$$\hat{T}_2 = \left(\frac{1}{2!}\right)^2 \sum_{abij} t_{ij}^{ab} \left(\hat{a}_a^+ \hat{a}_i \hat{a}_b^+ \hat{a}_j\right) \tag{2.36}$$

$$\hat{T}_3 = \left(\frac{1}{3!}\right)^2 \sum_{abcijk} t_{ijk}^{abc} (\hat{a}_a^+ \hat{a}_i \hat{a}_b^+ \hat{a}_j \hat{a}_c^+ \hat{a}_k) \tag{2.37}$$

$$\cdots$$

The coefficients t_i^a, t_{ij}^{ab}, t_{ijk}^{abc} … are referred to as CC amplitudes.

We may expand the exponential wave operator into a Taylor series,

$$e^{\hat{T}} = 1 + \hat{T} + \frac{1}{2!}\hat{T}^2 + \frac{1}{3!}\hat{T}^3 + \cdots \tag{2.38}$$

and use this expansion in Eq. (2.32), yielding the expression

$$\Psi_0 = (1 + \widehat{T}_1 + \frac{1}{2}\widehat{T}_1{}^2 + \widehat{T}_2 + \widehat{T}_3 + \widehat{T}_1\widehat{T}_2 + \frac{1}{3!}\widehat{T}_1{}^3 + \widehat{T}_4 + \frac{1}{2}\widehat{T}_2{}^2 + \frac{1}{2}\widehat{T}_1{}^2\widehat{T}_2 + \frac{1}{2}\widehat{T}_1\widehat{T}_2{}^2 + \cdots)\Phi_0 \tag{2.39}$$

for the CC wavefunction.

The doubly excited term of the wavefunction is given by $\hat{T}_2 + \frac{1}{2}\hat{T}_1^{\,2}$, and the triply excited term is given by $\hat{T}_3 + \hat{T}_1\hat{T}_2 + \frac{1}{3!}\hat{T}_1^{\,3}$, etc. It indicates that at the same truncation level, e.g., singles and doubles, the CC ansatz yields a better description of the exact wavefunction than the CI ansatz. The CC ansatz parameterizes the exact solution.

The CC equations for the energy and the amplitudes are obtained by using the ansatz (2.32) and (2.33) in the Schrödinger equation,

$$\hat{H}e^{\hat{T}}\Phi_0 = E_0^{CC}e^{\hat{T}}\Phi_0 \tag{2.40}$$

and multiplying from the left with the operator $e^{-\hat{T}}$,

$$e^{-\hat{T}}\hat{H}e^{\hat{T}}\Phi_0 = e^{-\hat{T}}E_0^{CC}e^{\hat{T}}\Phi_0 = E_0^{CC}\Phi_0 \tag{2.41}$$

The projection of this equation on the reference state gives the expression

$$E_0^{CC} = \langle\Phi_0|e^{-\hat{T}}\hat{H}e^{\hat{T}}|\Phi_0\rangle \tag{2.42}$$

for the CC ground state energy.

The amplitude equations are obtained by projecting Eq. (2.41) on the excited HF excitations,

$$\langle\Phi_P|e^{-\hat{T}}\hat{H}e^{\hat{T}}|\Phi_0\rangle = 0, \qquad P\epsilon\{S, D, T \dots\} \tag{2.43}$$

We can introduce the Baker-Campbell-Hausdorff expansion,

$$e^{-\hat{T}}\hat{H}e^{\hat{T}} = \hat{H} + [\hat{H},\hat{T}] + \frac{1}{2!}\left[[\hat{H},\hat{T}],\hat{T}\right] + \cdots \tag{2.44}$$

and use it in Eq. (2.42),

$$E_0^{CC} = \langle\Phi_0|\hat{H}|\Phi_0\rangle + \langle\Phi_0|[\hat{H},\hat{T}]|\Phi_0\rangle + \left\langle\Phi_0\left|\frac{1}{2!}\left[[\hat{H},\hat{T}],\hat{T}\right]\right|\Phi_0\right\rangle + \cdots \tag{2.45}$$

Since the $\langle\Phi_0|[\hat{H},\hat{T}_1]|\Phi_0\rangle$ term vanishes due to *Brillouin's Theorem* and $\langle\Phi_0|[\hat{H},\hat{T}_n]|\Phi_0\rangle = 0$ for n>2, the energy expression simplifies according to

$$E_0^{CCSD} = \langle\Phi_0|\hat{H}|\Phi_0\rangle + \langle\Phi_0|[\hat{H},\hat{T}_2]|\Phi_0\rangle + \left\langle\Phi_0\left|\frac{1}{2!}\left[[\hat{H},\hat{T}_1],\hat{T}_1\right]\right|\Phi_0\right\rangle \tag{2.46}$$

This means that only the singles and doubles of the CC amplitudes enter the computation of the ground state energy.

2.3.2 Size-consistent property

The quality of the computational results of a size-consistent method is independent of the size of the system, which ensures the applicability of this method to large systems. In this section, we will discuss the size-consistency of the CI and CC methods for ground states.

Consider a system consisting of two non-interacting subsystems A and B. The total energy of the system should be the sum of the fragment energies,

$$E_0^{AB} = E_0^A + E_0^B \tag{2.47}$$

and the wavefunction should be given as a product,

$$\Psi_0^{AB} = \hat{A}\Psi_0^A\Psi_0^B \tag{2.48}$$

where $\hat{A}$ denotes the inter-fragment anti-symmetrizer operator. The inter-fragment anti-symmetry has no practical relevance and may be skipped in the following.

In the CID approximation, the wavefunction is

$$\Psi_0^{CID} = (1 + \hat{C}_D^A + \hat{C}_D^B)\Phi_0^A\Phi_0^B \tag{2.49}$$

However, the full wavefunction is

$$\begin{aligned} \Psi_0^{AB} = \Psi_0^A\Psi_0^B &= \{(1 + \hat{C}_D^A)\Phi_0^A\}\{(1 + \hat{C}_D^B)\Phi_0^B\} \\ &= (1 + \hat{C}_D^A + \hat{C}_D^B + \hat{C}_D^A\hat{C}_D^B)\Phi_0^A\Phi_0^B \end{aligned} \tag{2.50}$$

Obviously, in the CID wavefunction, the quadruple excitation term $\hat{C}_D^A\hat{C}_D^B\Phi_0^A\Phi_0^B$ is missing. Moreover, the CID ground state energy for the complete system differs from the sum of the CID energies for the fragments. This indicates that the CID (and CISD) methods are not size-consistent. Now we turn to the size-consistent property of coupled cluster theory, for the non-interacting system. The reference (zeroth order) state, is given by the product of the fragment reference states,

$$\Phi_0^{AB} = \Phi_0^A\Phi_0^B \tag{2.51}$$

The $\hat{T}$ operator is additive, $\hat{T}^{AB} = \hat{T}^A + \hat{T}^B$, and $\hat{T}^A$ and $\hat{T}^B$ commute, so that $e^{\hat{T}^A+\hat{T}^B} = e^{\hat{T}^A} \cdot e^{\hat{T}^B}$.

According to

$$\Psi_0^{AB} = e^{\hat{T}^A+\hat{T}^B}\Phi_0^{AB} = e^{\hat{T}^A+\hat{T}^B}\Phi_0^A\Phi_0^B$$
$$= e^{\hat{T}^A}\Phi_0^A e^{\hat{T}^B}\Phi_0^B = \Psi_0^A\Psi_0^B \tag{2.52}$$

the product form of the CC ground state can be established.

Moreover, the energy is also additive:

$$\begin{aligned}E_0^{AB} &= \langle\Phi_0^{AB}|e^{-\hat{T}^A-\hat{T}^B}(\hat{H}^A+\hat{H}^B)e^{\hat{T}^A+\hat{T}^B}|\Phi_0^{AB}\rangle \\ &= \langle\Phi_0^{AB}|e^{-\hat{T}^A-\hat{T}^B}\hat{H}^A e^{\hat{T}^A+\hat{T}^B}|\Phi_0^{AB}\rangle + \langle\Phi_0^{AB}|e^{-\hat{T}^A-\hat{T}^B}\hat{H}^B e^{\hat{T}^A+\hat{T}^B}|\Phi_0^{AB}\rangle \\ &= \langle\Phi_0^{A}|e^{-\hat{T}^A}\hat{H}^A e^{\hat{T}^A}|\Phi_0^{A}\rangle + \langle\Phi_0^{B}|e^{-\hat{T}^B}\hat{H}^B e^{\hat{T}^B}|\Phi_0^{B}\rangle \\ &= E_0^A + E_0^B\end{aligned} \tag{2.53}$$

This shows that coupled cluster approximation possesses size-consistent property.

2.4 Equation of motion coupled cluster theory for electron affinities

As mentioned in the last section, traditional CC schemes have been widely applied to ground states calculations of many closed-shell systems and have proved to be very successful, especially some truncated forms, such as CCSD(T). However, traditional CC methods are not suitable for the treatment of excited states, including excitations in the (N-1)-electron, N-electron and (N+1)-electron systems, that is cations, molecules and anions. In the thesis, the anions, which we are interested in, are open-shell doublet radicals. Here, traditional CC schemes are suffering from the fact that the dominant reference wavefunction inadequately describes the electronic states. The open-shell reference wavefunctions (based on UHF or ROHF) for coupled cluster theory [64], are not always pure spin eigenfunctions, which undermines the reliability of those methods. Moreover, traditional coupled cluster method is computational costly. In the case of more than one excited electronic states of anions, the traditional coupled cluster would treat each state separately, which is very inefficient and often not even feasible. Thus, for large anion systems in the later chapters, one needs a reliable, low-cost and accurate theory.

To obtain accurate results for excited states, one can use coupled cluster response theory [65-68], equation of motion coupled cluster (EOM-CC) [43, 69-72], symmetry-adapted cluster CI [73, 74], and Green function theory, such as ADC [75-77]. Among these methods, EOM-CC is a generally applied, low-cost approach affording a balanced description of general electronic excitations. Moreover, being a single-reference method, the computational cost of EOM-CC is lower than multi-reference methods, recommending it for applications to large molecular systems.

2.4.1 Equation of motion Ansatz

We introduce an ansatz that there is an operator $\hat{R}$,

$$|\Psi_{exe}\rangle = \hat{R}|\Psi_0\rangle \tag{2.54}$$

where $|\Psi_{exe}\rangle$ and $|\Psi_0\rangle$ are the wavefunction of an excited state and the ground state, respectively. The operator $\hat{R}$ is referred to as the excitation operator, associated with a specific excited state.

Similarly, one can insert the equation of motion ansatz into the Schrödinger equation,

$$\hat{H}\hat{R}|\Psi_0\rangle = E_{exc}\hat{R}|\Psi_0\rangle \tag{2.55}$$

where E_{exc} is the total energy of the excited state. Applying $\hat{R}$ to Schrödinger equation for the ground state gives

$$\hat{R}\hat{H}|\Psi_0\rangle = \hat{R}E_0|\Psi_0\rangle \tag{2.56}$$

which can be combined with Eq. (2.55)

$$(\hat{H}\hat{R} - \hat{R}\hat{H})|\Psi_0\rangle = \Delta E_{exc}\hat{R}|\Psi_0\rangle \tag{2.57}$$

where $\Delta E_{exc} = E_{exc} - E_0$ denotes the excitation energy.

Eq. (2.57) can also be written as

$$[\hat{H}, \hat{R}]|\Psi_0\rangle = \Delta E_{exc}\hat{R}|\Psi_0\rangle \tag{2.58}$$

As this procedure is similar to the *Heisenberg Equation of Motion* for operators, this formulation is referred to as equation of motion (EOM) approach. With the help of Eq. (2.58), one can obtain the excitation energies of excited states without repetitive calculating owing to treating each state separately, like in the traditional coupled cluster method. The procedure of determining the operators $\hat{R}$ will be discussed in section 2.4.2.

2.4.2 Equation of motion coupled cluster theory

Now, we apply the EOM ansatz to coupled cluster theory. Let us first consider the case of excitations in the N-electron system. For the excited state wavefunction, Eq. (2.54) can be written as,

$$|\Psi_{exe}\rangle = \hat{R}|\Psi_{cc}\rangle = \hat{R}e^{\hat{T}}|\Phi_0\rangle \tag{2.59}$$

Similar to the cluster operator $\hat{T}$, one can write the excitation operator in the form

$$\hat{R} = \hat{R}_0 + \hat{R}_1 + \hat{R}_2 + \cdots \tag{2.60}$$

$$\hat{R}_0 = r_0 \tag{2.61}$$

$$\hat{R}_1 = \sum_{ai} r_i^a (\hat{a}_a^+ \hat{a}_i) \tag{2.62}$$

$$\hat{R}_2 = \left(\frac{1}{2!}\right)^2 \sum_{abij} r_{ij}^{ab} \left(\hat{a}_a^+ \hat{a}_i \hat{a}_b^+ \hat{a}_j\right) \tag{2.63}$$

$$\cdots$$

Note that r_0 vanishes, if the excited state symmetry differs from that of the ground state.

Similar to the procedure in section 2.4.1, one can insert the EOM ansatz into the Schrödinger equation,

$$\hat{H}\hat{R}e^{\hat{T}}|\Phi_0\rangle = E_{exc}\hat{R}e^{\hat{T}}|\Phi_0\rangle \tag{2.64}$$

Commuting the operator $\hat{R}$ with $e^{\hat{T}}$, and multiplying by $e^{-\hat{T}}$ from the left side, gives

$$e^{-\hat{T}}\hat{H}e^{\hat{T}}\hat{R}|\Phi_0\rangle = e^{-\hat{T}}E_{exc}e^{\hat{T}}\hat{R}|\Phi_0\rangle = E_{exc}\hat{R}|\Phi_0\rangle \tag{2.65}$$

Eq. (2.65) is similar to the CI eigenvalue equation, where however the original Hamiltonian is replaced by the similarity-transformed Hamiltonian.

$$\hat{\bar{H}} = e^{-\hat{T}}\hat{H}e^{\hat{T}} \tag{2.66}$$

As $\hat{\bar{H}}$ is non-Hermitian, the right eigenvalue problem Eq. (2.65) is supplemented by an equivalent left problem,

$$\langle \Phi_0 | \, \hat{L} \, \hat{\bar{H}} = \langle \Phi_0 | \, \hat{L} \, E_{exc} \tag{2.67}$$

where the right and left expansion operators are biorthogonal and can be normalized according to

$$\left\langle \Phi_0 \middle| \hat{L}^n \hat{R}^m \middle| \Phi_0 \right\rangle = A\delta_{nm} \tag{2.68}$$

Here n, m are state labels, and A can be chosen to be 1. Now the EOM-CC energy expression is,

$$E_{exc} = \left\langle \Phi_0 \middle| \hat{L}\hat{\bar{H}}\hat{R} \middle| \Phi_0 \right\rangle = E_0^{CC} + \left\langle \Phi_0 \middle| \hat{L}\hat{\bar{H}}_N\hat{R} \middle| \Phi_0 \right\rangle \tag{2.69}$$

where E_0^{CC} is the coupled-cluster energy of ground state and

$$\hat{\bar{H}}_N = \hat{\bar{H}} - \left\langle \Phi_0 \middle| \hat{\bar{H}} \middle| \Phi_0 \right\rangle \tag{2.70}$$

For $\hat{R} = 1$, the right-side eigenvalue problem recovers the CC equation for the ground state,

$$\left\langle \Phi_P \middle| e^{-\hat{T}} \hat{H} e^{\hat{T}} - E_0^{CC} \middle| \Phi_0 \right\rangle = 0 \tag{2.71}$$

The corresponding left ground state equation reads,

$$\left\langle \Phi_0 \middle| (1 + \hat{\Lambda})(e^{-\hat{T}} \hat{H} e^{\hat{T}} - E_0^{CC}) \middle| \Phi_P \right\rangle = 0 \tag{2.72}$$

Here $\hat{\Lambda}$ is an operator expansion,

$$\begin{gathered} \hat{\Lambda} = \hat{\Lambda}_1 + \hat{\Lambda}_2 + \cdots \\ \langle \Phi_0 | \hat{\Lambda} e^{-\hat{T}} = \sum_P \lambda_P \langle \Phi_P | e^{-\hat{T}} \end{gathered} \tag{2.73}$$

and $\langle \Phi_0 | \, (1 + \hat{\Lambda}) e^{-\hat{T}}$ is referred to as the dual ground state.

To obtain secular equations we project the eigenvalue equation Eq. (2.65) to the excitation space,

$$\left\langle \Phi_P \middle| \hat{\bar{H}}\hat{R} \middle| \Phi_0 \right\rangle = E_{exc} \langle \Phi_P | \hat{R} | \Phi_0 \rangle \tag{2.74}$$

where $|\Phi_P\rangle$ denote ground and excited HF configurations. Introducing the resolution of the identity

$$\sum_Q |\Phi_Q\rangle\langle\Phi_Q| = 1 \tag{2.75}$$

into Eq. (2.74), we obtain

$$\sum_Q \langle \Phi_P | \hat{\bar{H}} | \Phi_Q \rangle \langle \Phi_Q | \hat{R} | \Phi_0 \rangle = E_{exc} \langle \Phi_P | \hat{R} | \Phi_0 \rangle \tag{2.76}$$

Eq. (2.76) can also be written in matrix form,

$$\bar{\mathbf{H}}\boldsymbol{r} = E_{exc}\boldsymbol{r} \tag{2.77}$$

where, $\bar{\mathbf{H}}$ is the matrix of elements

$$\bar{\mathrm{H}}_{\mathrm{PQ}} = \left\langle \Phi_P \middle| \hat{\bar{H}} \middle| \Phi_Q \right\rangle \tag{2.78}$$

The elements of the eigenvector matrix **r** are

$$r_P = \langle \Phi_P | \hat{R} | \Phi_0 \rangle \tag{2.79}$$

Similarly, the left eigenvalue problem reads

$$\boldsymbol{l}^T \widehat{\overline{\boldsymbol{H}}} = \boldsymbol{l}^T E_{exc} \tag{2.80}$$

where the elements of $\boldsymbol{l}^T$ are given by

$$l_P = \langle \Phi_0 | \hat{L} | \Phi_P \rangle \tag{2.81}$$

The right and left eigenvectors for the final states n, m are biorthogonal,

$$\boldsymbol{l}^{m^T} \boldsymbol{r}^n = \boldsymbol{\delta}_{mn} \tag{2.82}$$

Moreover, the expression for the energy is,

$$E_{exc} = \boldsymbol{l}^T \overline{\mathbf{H}} \mathbf{r} \tag{2.83}$$

Eq. (2.77)-(2.83) are the matrix representations of the EOM-CC secular equations.

Similar to truncated CI, in practice, also truncated versions of the full EOM-CC have to be used, such as, EOM-CCSD [71]. The cluster operator and excitation operator of EOM-CCSD are both truncated and projected on the space of singles and doubles excitations,

$$\hat{T} = \hat{T}_1 + \hat{T}_2 \tag{2.84}$$

$$\hat{R} = \hat{R}_0 + \hat{R}_1 + \hat{R}_2 \tag{2.85}$$

Comparing to the CISD method, EOM-CCSD includes higher order contribution for excited states and it should perform better than CISD. Moreover, it is an suitable approach to study vibronic coupling problems, such as Jahn-Teller effect and pseudo-Jahn-Teller problem, near canonical intersection of the potential energy surface [78].

The EOM-CC approach is quite general and can readily be transferred to the excitation of N-1 electrons (IP) or N+1 electrons (EA). In the N+1 system, the excitation operators are 1p, 2p-1h, 3p-2h… operators, as follows,

$$\hat{R}_1^{EA} = \sum_a r^a \hat{a}_a^+ \tag{2.86}$$

$$\hat{R}_2^{EA} = \frac{1}{2} \sum_{abi} t_i^{ab} (\hat{a}_a^+ \hat{a}_i \hat{a}_b^+) \tag{2.87}$$

$$\hat{R}_3^{EA} = \frac{1}{12}\sum_{abcij} t_{ij}^{abc}\left(\hat{a}_a^{+}\hat{a}_i\hat{a}_b^{+}\hat{a}_j\hat{a}_c^{+}\right) \tag{2.88}$$

…

In general, truncation of the EOM-CCSD expansions (including EE-EOM-CCSD, EA-EOM-CCSD and IP-EOM-CCSD) are not always adequate for the single excited states. If the contribution of double excitation to the target single excited state is large, the EOM-CCSD expansions are not accurate enough [79-81]. Additionally, for the states with more than one excited electrons, such as, doubly excited states, the EOM-CCSD expansions cannot treat the excited states correctly. One can either expand truncated CC wavefunction, e.g., EOM-CCSDT [82], or add perturbative triples correction [83]. However, the methods beyond EOM-CCSD are yet too expensive to be applied to the systems considered in this work.

2.5 Analytical energy gradients for traditional coupled cluster theory and equation of motion coupled cluster theory

In most quantum chemistry methods, calculating energy derivatives is an indispensable requirement [84], e.g., determining minima or saddle points on the PES requires the computation of molecular energy gradients. Compared to the numerical computation of gradients, analytical energy gradient techniques are powerful tools. The cost is roughly twice the cost required to evaluate energies, irrespective of the number of degrees of freedom of the system. Here, we give a short overview of analytical energy gradients concepts within the traditional CC and EOM-CC theory, which have been applied in the present work.

2.5.1 Analytical energy gradients of traditional coupled cluster singles and doubles method

In the literature, there is a detailed description of the analytical gradients for the traditional coupled cluster theory, i.e., CCSD [85, 86], to which we refer in the following.

Noteworthy, truncated CC theory is not variational as the CC equations for the CC amplitudes are obtained in terms of a projection of the Schrödinger equation. Since CC theory is nonvariational, the direct differentiation of the CC energy is not an appropriate starting point for developing analytical gradient equations. Instead, one can turn to the CC Lagrangian formulation of the excitation energy,

$$L = \langle \Phi_0 | e^{-\hat{T}} \hat{H} e^{\hat{T}} | \Phi_0 \rangle + \sum_I \lambda_I \langle \Phi_I | e^{-\hat{T}} \hat{H} e^{\hat{T}} | \Phi_0 \rangle = \langle \Phi_0 | (1 + \hat{\Lambda}) e^{-\hat{T}} \hat{H} e^{\hat{T}} | \Phi_0 \rangle \qquad (2.89)$$

here $\hat{\Lambda}$ is given by Eq. (2.73) utilized in section 2.4.2.

The stationarity conditions for L are as follows,

$$\frac{\partial L}{\partial \lambda_I} = 0 = \langle \Phi_I | e^{-\hat{T}} \hat{H} e^{\hat{T}} | \Phi_0 \rangle \qquad (2.90)$$

$$\frac{\partial L}{\partial t_I} = 0 = \langle \Phi_0 | (1 + \hat{\Lambda}) e^{-\hat{T}} \hat{H} e^{\hat{T}} - E_0^{CC} | \Phi_I \rangle \qquad (2.91)$$

Eq. (2.90) and Eq. (2.91) are the CC equations for the t-amplitudes (Eq. (2.43)) and the $\hat{\Lambda}$ coefficients of the dual ground state, respectively.

As a consequence, the derivative of the energy is of the simple form,

$$\frac{\partial E}{\partial x} = \sum_I \frac{\partial L}{\partial \lambda_I} \frac{\partial \lambda_I}{\partial x} + \sum_I \frac{\partial L}{\partial t_I} \frac{\partial t_I}{\partial x} + \left\langle \Phi_0 \left| (1 + \hat{\Lambda}) e^{-\hat{T}} \frac{\partial \hat{H}}{\partial x} e^{\hat{T}} \right| \Phi_0 \right\rangle$$

$$= \left\langle \Phi_0 \left| (1 + \hat{\Lambda}) e^{-\hat{T}} \frac{\partial \hat{H}}{\partial x} e^{\hat{T}} \right| \Phi_0 \right\rangle \qquad (2.92)$$

where x is an external perturbation parameter. By introducing (effective) density matrices, as described by Gauss and co-workers [86], one can simplify Eq. (2.91) as,

$$\frac{\partial E}{\partial x} = \sum_{pq} D_{pq} \frac{\partial f_{pq}}{\partial x} + \frac{1}{4} \sum_{pqrs} \Gamma_{pqrs} \frac{\partial \langle pq || rs \rangle}{\partial x} \tag{2.93}$$

where f_{pq} are the Fock matrix elements and $\langle pq||rs \rangle$ denote the anti-symmetric Coulomb integrals of the Hamiltonian, $\langle pq||rs \rangle = g_{pqrs} - g_{pqsr}$. D_{pq} and Γ_{pqrs} are reduced one- and two- particle density matrices, respectively.

2.5.2 Analytical energy gradients of the equation of motion coupled cluster singles and doubles method

As EOM-CC calculations for excited states of larger systems are time-consuming, so that a numerical computation of energy gradients is not viable. To apply the EOM-CC methods to large systems, one needs analytical energy gradients. In the literature, there is a detailed description of how to deduce analytical gradients for the equation of motion coupled cluster method [87-89]. In the following, we give a short overview of analytical gradients of EOM-CCSD.

Fortunately, EOM-CC is bivariational with respect to the excitations operator $\hat{R}$ and $\hat{L}$, while it is not variational for the cluster operator $\hat{T}$. One can start from the straightforward differentiation of Eq. (2.69)

$$\begin{aligned}\frac{\partial \Delta E}{\partial x} = {} & \langle \Phi_0 | \hat{L} \hat{\bar{H}} \frac{\partial \hat{R}}{\partial x} | \Phi_0 \rangle + \langle \Phi_0 | \frac{\partial \hat{L}}{\partial x} \hat{\bar{H}} \hat{R} | \Phi_0 \rangle + \langle \Phi_0 | \hat{L} \left[\hat{\bar{H}}, \frac{\partial \hat{T}}{\partial x} \right] \hat{R} | \Phi_0 \rangle \\ & + \langle \Phi_0 | \hat{L} e^{-\hat{T}} \frac{\partial \hat{H}_N}{\partial x} e^{\hat{T}} \hat{R} | \Phi_0 \rangle \end{aligned} \tag{2.94}$$

where $\hat{H}_N$ is given by Eq. (2.70).

The first two terms of Eq. (2.94) cancel each other as can be easily seen according to

$$\begin{aligned}\langle \Phi_0 | \hat{L} \hat{\bar{H}} \frac{\partial \hat{R}}{\partial x} | \Phi_0 \rangle + \langle \Phi_0 | \frac{\partial \hat{L}}{\partial x} \hat{\bar{H}} \hat{R} | \Phi_0 \rangle &= \Delta E \{ \langle \Phi_0 | \hat{L} \frac{\partial \hat{R}}{\partial x} | \Phi_0 \rangle + \langle \Phi_0 | \frac{\partial \hat{L}}{\partial x} \hat{R} | \Phi_0 \rangle \} \\ &= \Delta E \left(\frac{\partial \langle \Phi_0 | \hat{L} \hat{R} | \Phi_0 \rangle}{\partial x} \right) = 0 \end{aligned} \tag{2.95}$$

Next we consider the third term in Eq. (2.94) referred to as T3, containing derivatives of the $\hat{T}$ operator,

$$T3 = \langle \Phi_0 | \hat{L} \left[\hat{\bar{H}}, \frac{\partial \hat{T}}{\partial x} \right] \hat{R} | \Phi_0 \rangle = \langle \Phi_0 | \hat{L} \hat{\bar{H}} \frac{\partial \hat{T}}{\partial x} | \Phi_0 \rangle - \langle \Phi_0 | \hat{L} \frac{\partial \hat{T}}{\partial x} \hat{\bar{H}} | \Phi_0 \rangle \tag{2.96}$$

Inserting the resolution of the identity Eq. (2.74) after the operator $\hat{\bar{H}}$ in the first term and left of the $\hat{\bar{H}}$ in the second term one obtains,

$$\begin{aligned} T3 = & \{ \langle \Phi_0 | \hat{L} \hat{\bar{H}} | \Phi_0 \rangle \langle \Phi_0 | \frac{\partial \hat{T}}{\partial x} \hat{R} | \Phi_0 \rangle - \langle \Phi_0 | \hat{L} \frac{\partial \hat{T}}{\partial x} | \Phi_0 \rangle \langle \Phi_0 | \hat{\bar{H}} \hat{R} | \Phi_0 \rangle \} \\ & + \sum_{P \epsilon \{S,D\}} \{ \langle \Phi_0 | \hat{L} \hat{\bar{H}} | \Phi_P \rangle \langle \Phi_P | \frac{\partial \hat{T}}{\partial x} \hat{R} | \Phi_0 \rangle - \langle \Phi_0 | \hat{L} \frac{\partial \hat{T}}{\partial x} | \Phi_P \rangle \langle \Phi_P | \hat{\bar{H}} \hat{R} | \Phi_0 \rangle \} \\ & + \sum_{Q \epsilon \{T,Q \ldots\}} \{ \langle \Phi_0 | \hat{L} \hat{\bar{H}} | \Phi_Q \rangle \langle \Phi_Q | \frac{\partial \hat{T}}{\partial x} \hat{R} | \Phi_0 \rangle - \langle \Phi_0 | \hat{L} \frac{\partial \hat{T}}{\partial x} | \Phi_Q \rangle \left\langle \Phi_Q \middle| \hat{\bar{H}} \hat{R} | \Phi_0 \right\rangle \Big\} \end{aligned} \tag{2.97}$$

where the sums have been split into an S, D part and a T, Q… part. Using the EOM-CC secular equations (2.77) and (2.80) in the CCSD formulation, Eq. (2.97) can be further simplified to

$$T3 = \sum_{Q \epsilon \{T,Q,\ldots\}} \{ \langle \Phi_0 | \hat{L} \hat{\bar{H}} | \Phi_Q \rangle \langle \Phi_Q | \frac{\partial \hat{T}}{\partial x} \hat{R} | \Phi_0 \rangle - \langle \Phi_0 | \hat{L} \frac{\partial \hat{T}}{\partial x} | \Phi_Q \rangle \langle \Phi_Q | \hat{\bar{H}} \hat{R} | \Phi_0 \rangle \} \tag{2.98}$$

Since

$$\langle \Phi_0 | \hat{L} \frac{\partial \hat{T}}{\partial x} | \Phi_Q \rangle = 0$$

as $\hat{L}$ is restricted to single and double excitations, while $|\Phi_Q\rangle$ is at least a triple excitation, the second term on the right-hand side vanishes yielding,

$$T3 = \sum_{Q \epsilon \{T,Q,\ldots\}} \langle \Phi_0 | \hat{L} \hat{\bar{H}} | \Phi_Q \rangle \langle \Phi_Q | \frac{\partial \hat{T}}{\partial x} \hat{R} | \Phi_0 \rangle \tag{2.99}$$

Since both $\frac{\partial \hat{T}}{\partial x}$ and $\hat{R}$ are excitation operators, they commute so that Eq. (2.99) can be written as

$$T3 = \sum_{Q \epsilon \{T,Q,\ldots\}} \langle \Phi_0 | \hat{L} \hat{\bar{H}} | \Phi_Q \rangle \langle \Phi_Q | \hat{R} \frac{\partial \hat{T}}{\partial x} | \Phi_0 \rangle \tag{2.100}$$

Using once again Eq. (2.75), the second factor in the product of matrix elements can be decomposed according to

$$\langle \Phi_Q | \hat{R} \frac{\partial \hat{T}}{\partial x} | \Phi_0 \rangle = \sum_{P \epsilon \{S,D\}} \langle \Phi_Q | \hat{R} | \Phi_P \rangle \langle \Phi_P | \frac{\partial \hat{T}}{\partial x} | \Phi_0 \rangle \tag{2.101}$$

where the restriction of the configurations $|\Phi_P\rangle$ to single and double excitations is due to the fact that in the CCSD approach the $\hat{T}$ operator (and then also $\frac{\partial \hat{T}}{\partial x}$) is confined to single and double excitations.

For a more compact notation we introduce the row vectors

$$\langle \Phi_0 | \hat{L} \widehat{\bar{H}} \boldsymbol{\Xi} \hat{R} | \boldsymbol{P} \rangle$$

with elements

$$\langle \Phi_0 | \hat{L} \widehat{\bar{H}} \boldsymbol{\Xi} \hat{R} | \Phi_P \rangle = \sum\nolimits_{Q \epsilon \{T,Q,\ldots\}} \langle \Phi_0 | \hat{L} \widehat{\bar{H}} | \Phi_Q \rangle \langle \Phi_Q | \hat{R} | \Phi_P \rangle, \qquad P \epsilon \{S,D\} \tag{2.102}$$

and the column vector $\langle \boldsymbol{P} | \frac{\partial \hat{T}}{\partial x} | \Phi_0 \rangle$ of the elements $\langle \Phi_P | \frac{\partial \hat{T}}{\partial x} | \Phi_0 \rangle$.

This allows one to write Eq. (2.96) as a scalar product,

$$T3 = \langle \Phi_0 | \hat{L} \widehat{\bar{H}} \boldsymbol{\Xi} \hat{R} | \boldsymbol{P} \rangle \langle \boldsymbol{P} | \frac{\partial \hat{T}}{\partial x} | \Phi_0 \rangle \tag{2.103}$$

The derivatives of the $\hat{T}$ operator can be expressed in terms of derivatives of the Hamiltonian, $\frac{\partial \hat{H}}{\partial x}$. As the first step towards this end, the ground state CCSD equations,

$$\langle \Phi_P | \widehat{\bar{H}} | \Phi_0 \rangle = 0, \qquad P \epsilon \{S,D\} \tag{2.104}$$

can be differentiated with respect to x, yielding

$$0 = \frac{\partial}{\partial x} \langle \Phi_P | \widehat{\bar{H}} | \Phi_0 \rangle = \langle \Phi_P | \widehat{\bar{H}} \frac{\partial \hat{T}}{\partial x} | \Phi_0 \rangle - \langle \Phi_P | \frac{\partial \hat{T}}{\partial x} \widehat{\bar{H}} | \Phi_0 \rangle + \langle \Phi_P | e^{-\hat{T}} \frac{\partial \hat{H}_N}{\partial x} e^{\hat{T}} | \Phi_0 \rangle \tag{2.105}$$

Note that in the last term $\hat{H}$ could be replaced by $\hat{H}_N$. Using once again the resolution of the identity Eq. (2.75) truncated after the double excitations (but including $|\Phi_0\rangle$) in the first and second term leads, after some algebra, to the following expression for the vector of $\langle \Phi_P | \frac{\partial \hat{T}}{\partial x} | \Phi_0 \rangle$ matrix elements,

$$\langle \boldsymbol{P} | \frac{\partial \hat{T}}{\partial x} | \Phi_0 \rangle = -\langle \boldsymbol{P} | \widehat{\bar{H}}_N | \boldsymbol{P} \rangle^{-1} \langle \boldsymbol{P} | \widehat{\bar{H}}_N^x | \Phi_0 \rangle \tag{2.106}$$

where $\langle \boldsymbol{P} | \widehat{\bar{H}}_N | \boldsymbol{P} \rangle$ is the matrix of elements $\langle \Phi_P | \frac{\partial \widehat{\bar{H}}_N}{\partial x} | \Phi_{P'} \rangle$, $\mathrm{P}, P' \epsilon \{S,D\}$, for the operator

$$\hat{\hat{H}}_N^x = e^{-\hat{T}} \frac{\partial \hat{H}_N}{\partial x} e^{\hat{T}} \tag{2.107}$$

Combining Eq. (2.106) and Eq. (2.103) yields the expression

$$T3 = -\langle \Phi_0 | \hat{L} \hat{\hat{H}} \Xi \hat{R} | \boldsymbol{P} \rangle \, \langle \boldsymbol{P} | \hat{\hat{H}}_N | \boldsymbol{P} \rangle^{-1} \langle \boldsymbol{P} | \hat{\hat{H}}_N^x | \Phi_0 \rangle \tag{2.108}$$

in which the original derivative of the $\hat{T}$ operator has been eliminated.

Now we introduce the row vector

$$\langle \Phi_0 | \boldsymbol{Z} | \boldsymbol{P} \rangle = -\langle \Phi_0 | \hat{L} \hat{\hat{H}} \Xi \hat{R} | \boldsymbol{P} \rangle \langle \boldsymbol{P} | \hat{\hat{H}}_N | \boldsymbol{P} \rangle^{-1} \tag{2.109}$$

being the result of applying the inverse of the matrix $\langle \boldsymbol{P} | \hat{\hat{H}}_N | \boldsymbol{P} \rangle$ to the vector $-\langle \Phi_0 | \hat{L} \hat{\hat{H}} \Xi \hat{R} | \boldsymbol{P} \rangle$. Eq. (2.109), referred to as Z-vector equation, is completely independent of the respective derivative $\frac{\partial}{\partial x}$.

The third term in Eq. (2.94) can now compactly rewritten as

$$T3 = \langle \Phi_0 | \boldsymbol{Z} | \boldsymbol{P} \rangle \langle \boldsymbol{P} | \hat{\hat{H}}_N^x | \Phi_0 \rangle \tag{2.110}$$

that is as a scalar product of the general Z-vector and a vector of elements depending explicitly on the respective derivative in the form of $\frac{\partial}{\partial x} \hat{\hat{H}}$.

The final form for Eq. (2.94), obtained by adding the third and fourth term, reads

$$\frac{\partial \Delta E}{\partial x} = \langle \Phi_0 | \boldsymbol{Z} | \boldsymbol{P} \rangle \langle \boldsymbol{P} | \hat{\hat{H}}_N^x | \Phi_0 \rangle + \langle \Phi_0 | \hat{L} \hat{\hat{H}}_N^x \hat{R} | \Phi_0 \rangle \tag{2.111}$$

In both terms the derivatives enter in the form of derivatives of the Hamiltonian.

This means that, as discussed in ref. 87 and 88, similar to Eq. (2.91), the derivative of EOM-CCSD excitation energy can be written in the form

$$\frac{\partial E}{\partial x} = \sum_{pq} \gamma_{pq} \frac{\partial f_{pq}}{\partial x} + \frac{1}{4} \sum_{pqrs} \Gamma_{pqrs} \frac{\partial \langle pq || rs \rangle}{\partial x} \tag{2.112}$$

as a linear combination of the matrix elements of the differentiated Hamiltonian, and effective one- and two- particle densities γ_{pq} and Γ_{abij},

$$\gamma_{pq} = \langle \Phi_0 | \hat{L} \left[a_p^+ a_q e^{\hat{T}} \right]_c \hat{R} | \Phi_0 \rangle + \langle \Phi_0 | \boldsymbol{Z} \left[a_p^+ a_q e^{\hat{T}} \right]_c | \Phi_0 \rangle \tag{2.113}$$

$$\Gamma_{abij} = \langle \Phi_0 | \hat{L} \left[a_p^+ a_q a_r^+ a_s e^{\hat{T}} \right]_c \hat{R} | \Phi_0 \rangle + \langle \Phi_0 | \boldsymbol{Z} \left[a_p^+ a_q a_r^+ a_s e^{\hat{T}} \right]_c | \Phi_0 \rangle \tag{2.114}$$

The process of calculating analytical gradient is a) solving the reference state CC equations, b) solving eigenvalue equation for $\hat{R}$ and $\hat{L}$, c) solving linear equation for $\boldsymbol{Z}$, d) computing the density matrices and the desired derivatives. The cost is about twice the cost of the EOM-CC energy computation.

Chapter 3

Valence and Superatomic states of C_{20}^{-}: Bound states of the Smallest Fullerene Anion

3.1 Background and motivation

Due to the unique and remarkable structure and physicochemical properties, researchers have paid much attention to fullerenes in various fields of science and technology. High electron affinity (EA) is one of their most important properties, which is the ability of attracting extra electrons and forming bound mono- or polyanions. Buckminsterfullerene C_{60} is the most well-known example [90-94]. In the past, the C_{60}/C_{60}^{n-} species were studied extensively, owning to their various intriguing features, including superconducting properties [95-97], Jahn–Teller distortions [98-100], and endohedral complexes [101-105]. Interestingly, although researchers have predicted the high electron affinity of C_{60} decades ago [106-111], it has been unknown until recently that C_{60} has several stable anionic states [112-115]. After analyzing the result from unprecedentedly large, high-level ab initio calculations and a corresponding simple heuristic model, it has been revealed that C_{60} has at least five bound anion states [115]. They include four valence states, namely, $^2T_{1u}$, $^2T_{1g}$, $^2T_{2u}$ and ^2H_g, as well as one so-called superatomic (SA) state, ^2A_g. To form the SA state, the proper description of a superatom molecular orbital (SAMO), as special feature of C_{60}, is necessary [116, 117]. The SA state in C_{60} is significantly different in nature from the valence states [114, 115, 118].

Based on the knowledge of bound states of the C_{60}^{-} anion, one may wonder whether one can expect a manifold of bound valence state and even superatomic anion states to exist in other fullerenes. To try to elucidate the question, we turned to C_{20}, the smallest fullerene. A previous study revealed that C_{20} possesses a relatively high positive electron affinity, ~2.25 eV [119], comparable to C_{60} (~2.69 eV) [94]. Thus, one can reasonably expect the C_{20}^{-} anion possessing several bound states, similarly to C_{60}^-. To the best of our knowledge, there were only a few previous studies mentioning C_{20}^- anion excited states [120-123]. Noteworthy, the question of the most favorable structure of the neutral C_{20} has drawn controversies (see discussions in ref. 120, 121, 123 and 124). Thus, the thermodynamically most favorable form of C_{20} fullerene is still unknown.

The chapter is organized as follows. In section 3.2, we briefly discuss the computational details of our calculations. In section 3.3, we study the ground state structure of the neutral C_{20}. In section 3.4, based on this optimized geometry, we present results of state-of-the-art calculation for the C_{20}^- anion. Here we employed the equation of motion coupled cluster singles and doubles method for electron affinities (EA-EOM-CCSD) [43]. In section 3.5, we analyze radial and angular density distributions for excess electrons of all C_{20} bound states. In section 3.6, we apply a heuristic charge model, which was previously successfully used for C_{60} [115], to estimate the bound states in the C_{20}^- anion. In section 3.7, we compare our results obtained at the largest possible basis set level to the experimental electron affinity of the C_{20}^- anion. Finally, in section 3.8, we summarize the results and conclude.

3.2 Computational details

We have carried out ground state geometry optimizations for C_{20} in different symmetry configurations, and the thermodynamically favored geometry obtained coincides with the one reported in ref. 124. We performed the calculations at Dunning's double- and triple-ζ basis set level [125], using MP2 [126] and DFT/B3LYP [127] procedures provided by the Gaussian 09 program package [128]. We also have performed a full ground state geometry optimization of C_{20} strictly within D_{3d} symmetry using the coupled cluster singles and doubles (CCSD) method [57] and Dunning's double-ζ basis set (cc-pVDZ). For the latter computations, the Molpro package [129] was utilized. To save computational expense, we applied the frozen core approximation to the 20 carbon core orbitals.

Based on the geometry obtained at CCSD/cc-pVDZ level, we searched for bound states of C_{20}^{-} employing the EA-EOM-CCSD method [43], and basis sets of different quality, in particular, the double and triple-ζ basis sets of Roos and co-workers [130]. Furthermore, these basis sets were augmented with 10 s-, 10 p-, and 10 d-type diffuse functions (denoted as 10spd) placed at the center of C_{20}. The exponents of the diffuse functions were generated using an even-tempered series $a_{n+1} = a_n/3.5$, starting with $a_0 = 1.0$. The diffuse functions have proven indispensable for the description of the SA state. In the following, we will refer to the double and triple-ζ basis sets as DZ and TZ, respectively. We excluded one d-function, as well as one or two f-functions in the excited states calculations. These basis sets, in this chapter, vary from 460 to 770 molecular orbitals. In the coupled cluster calculations, the carbon core orbitals were not frozen for technical reasons in obtaining the CCSD and EA-EOM-CCSD wavefunctions. Based on the wavefunctions, electron densities and singly occupied molecular natural orbitals (SONO) could be computed and analyzed. The CCSD and EA-EOM-CCSD calculations of electron densities were carried out with the CFOUR package [131]. We analyzed bound states of C_{20} employing density-difference distributions of the excess electron. This "Δρ analysis" was performed in previous studies [114, 115]. The approach is based on the analysis of the difference of two charge densities:

$$\Delta\rho(r) = \rho_A(r) - \rho_N(r)$$

Here $\rho_N(r)$ is the density of the neutral ground state and $\rho_A(r)$ is the density of the bound anion state.

The quantity Δρ(r) reflects the change of the total charge density in the electronic state of C_{20}^{-} with respect to the charge density of the neutral ground state. Δρ(r) can be both positive and negative. Positive values are indicative of the presence of the "attached" electron, while the negative values point out to a decrease in the electron density of a neutral state compared to the initial neutral state. In the following, we will analyze the radial density

$$\rho(\mathrm{r}) = \iiint_0^r \Delta\rho(\mathbf{r}) r^2 \sin\theta \, dr d\theta d\varphi$$

and the angular density distributions

$$\rho(\theta,\varphi) = \int_0^\infty \Delta\rho(\mathbf{r}) r^2 dr$$

for the bound anion states of C_{20}^{-}.

To better compare with the experimental data, we optimized the C_{20}^{-} ground state geometry at the EA-EOM-CCSD/cc-pVTZ level strictly within D_{2h} symmetry without applying the frozen core approximation. Similarly, we employed the CCSD method and the cc-pVTZ basis set to optimize the neutral C_{20} ground state conformation. Based on this high-level geometry optimization, we employed EA-EOM-CCSD (for the anion ground state) and CCSD (for the neutral ground state), using the full Roos triple-ζ basis set to calculate the adiabatic electron affinity of C_{20}^{-}.

3.3 Ground state structure of neutral C_{20}

In the literature, there has been a lively discussion on the C_{20} ground state structure considering cage, bowl and ring forms (see ref. 120, 121, 123, 124 as well as references therein). In this section, we only discuss the fullerene (cage) form of C_{20}, and there will be a further discussion of the ring form in Chapter 6. The C_{20} fullerene can be seen as being "dropped" from a highly symmetric I_h dodecahedral structure, since it has an open-shell electronic configuration in I_h. In fact, the occupation numbers of three highest occupied Hartree–Fock (HF) molecular orbitals (MO) are $(t_{1u})^6(h_g)^{10}(g_u)^2$. The highest occupied molecular orbital (HOMO) g_u, being four-fold degenerate, is only occupied by two electrons. Hence, C_{20} (I_h) could possibly be distorted to D_{5d}, D_{3d} or D_{2h} forms, since it is Jahn–Teller unstable [132]. Recently, Bartlett and co-workers reported a slightly distorted D_{3d} form as the thermodynamically most stable form of the neutral C_{20} cage, based on their results of CCSD/cc-pVTZ geometry optimization [124]. We performed C_{20} geometry optimization in different forms. Our results also suggest that the C_{20} cage with D_{3d} symmetry is the most favorable structure for neutral C_{20}, as shown in Table 3.1.

Table 3.1 Total (a.u.) and relative (kcal/mol) energies, and the type of stationary points (minimum or saddle point) for the different ground state structures of C_{20} obtained from a full geometry optimization using different methods and basis sets.

Methods & Basis sets	Symmetry	Total Energy (a.u.)	Relative Energy (kcal/mol)	Type
MP2/cc-pVDZ	D_{3d}	-759.3403888	0.00	Minimum
MP2/cc-pVDZ	D_{2h}	-759.3390249	0.86	Saddle
MP2/aug-cc-pVDZ	D_{3d}	-759.449050	0.00	Minimum
MP2/aug-cc-pVDZ	D_{2h}	-759.447680	0.86	Saddle
B3LYP/cc-pVDZ	C_{2h}	-761.500943	0.95	Minimum
B3LYP/cc-pVDZ	D_{3d}	-761.501033	0.99	Minimum
B3LYP/cc-pVDZ	D_{2h}	-761.502525	0.00	Minimum
B3LYP/cc-pVTZ	C_{2h}	-761.670525	0.11	Minimum
B3LYP/cc-pVTZ	D_{3d}	-761.670692	0.00	Minimum
B3LYP/cc-pVTZ	D_{2h}	-761.670566	0.08	Saddle

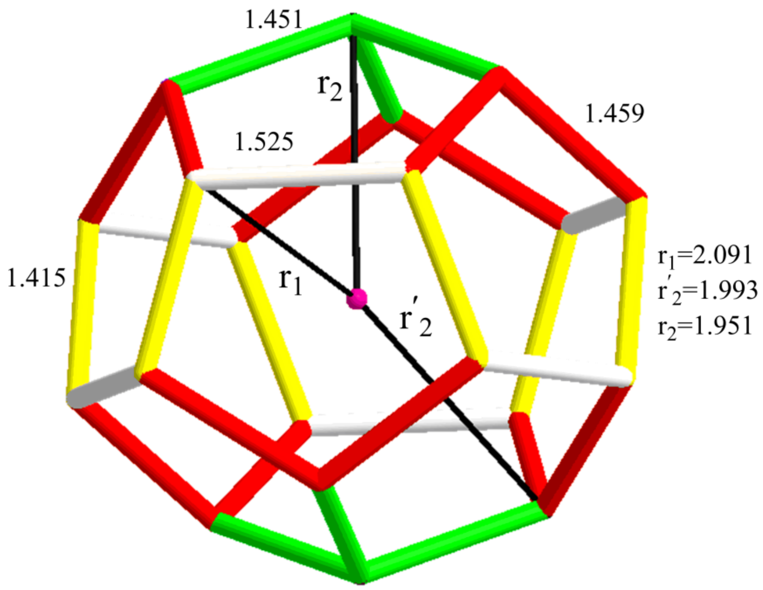

Figure 3.1. Ground state D_{3d} structure of neutral C_{20} obtained from CCSD/cc-pVDZ geometry optimization. The equivalent (symmetric) bonds are indicated by the same color. r_1, r_2' and r_2 are three characteristic radii from the center. All units are in Å.

The equilibrium geometry of C_{20} (D_{3d}) at the CCSD/cc-pVDZ level is shown in Fig. 3.1 along with structural parameters. The D_{3d} structure of C_{20} obtained at the CCSD/cc-pVDZ level, was used in the subsequent EA-EOM-CCSD calculations of the anion states. While the result of Bartlett and co-workers is slightly distorted from the D_{3d} symmetry, we chose our geometry optimized with symmetry restriction in the subsequent EA computations. The application of the state-of-the-art CCSD and EA-EOM-CCSD methods to C_{20} system is computationally utmost demanding or even unfeasible without the presence of symmetry (in this case C_{2h}, which is an abelian subgroup of D_{3d}).

3.4 Bound states of the C_{20}^{-} anion

As can be seen from the results of the EA-EOM-CCSD calculations presented in Fig. 3.2, there are five bound electronic states of C_{20}^{-} anion, comprising two ^2E_u, two $^2A_{2u}$ and one $^2A_{1g}$ state. The ground state of C_{20} is the 1^2E_u state with the highest binding energy. The remaining four states are excited states. The four low-lying states can be grouped into two pairs. There is a pair of strongly bound $^2E_u/^2A_{2u}$ states, namely 1^2E_u and 1^2A_{2u}, with binding energies 2.05 eV and 1.77 eV, respectively, and a weakly bound $^2E_u/^2A_{2u}$ states pair, with small binding energies 0.73 eV and 0.42 eV, respectively. The highest excited state, $^2A_{1g}$, is predicted with very small binding energy, being ~0.3 meV. At the HF (Koopmans' theorem) level, combined with large TZ(-1d1f) + 10spd basis set, only the first $^2E_u/^2A_{2u}$ pair appears as bound states, with binding energies 0.68 eV and 0.55 eV, respectively. At the HF level the binding energies are much lower than the EA-EOM-CCSD results, showing the importance of treating electron correlation effects and orbital relaxation/polarization effects properly. The orbital relaxation/polarization effects corresponding to the geometry change, because of extra electron attachment, are expected to be small, ~0.2 eV, similarly to C_{60} [113]. Moreover, for the second $^2E_u/^2A_{2u}$ and $^2A_{1g}$ state, which are unbound at the HF level, the electron correlation effects are critical. The discrepancy of about 1.4 eV between the HF and the EA-EOM-CCSD energies is to a large part due to the polarization effect, that is, the response of the C_{20} charge distribution to the attachment of an extra electron. Obviously, the HF binding energies, given as the (negative) orbital energies of a ground state HF calculation, correspond to a static picture and do not account for dynamical effects such as the polarization effect**.** Thus, we refer those states as electron-correlation bound states.

The binding energy of the C_{20} ground state (2.05 eV) is qualitatively comparable to the experimental value of 2.25 eV [119]. It should be noted that the experimental and theoretical values refer to the adiabatic electron affinity (AEA) and vertical electron affinity (VEA), respectively [133], which may partly explain the 0.2 eV discrepancy. By optimizing the geometry of the C_{20}^{-} anion and calculating the ground state energy using the large Roos full triple-ζ basis, one can obtain an accurate value for the adiabatic electron affinity, as will be discussed in section 3.7.

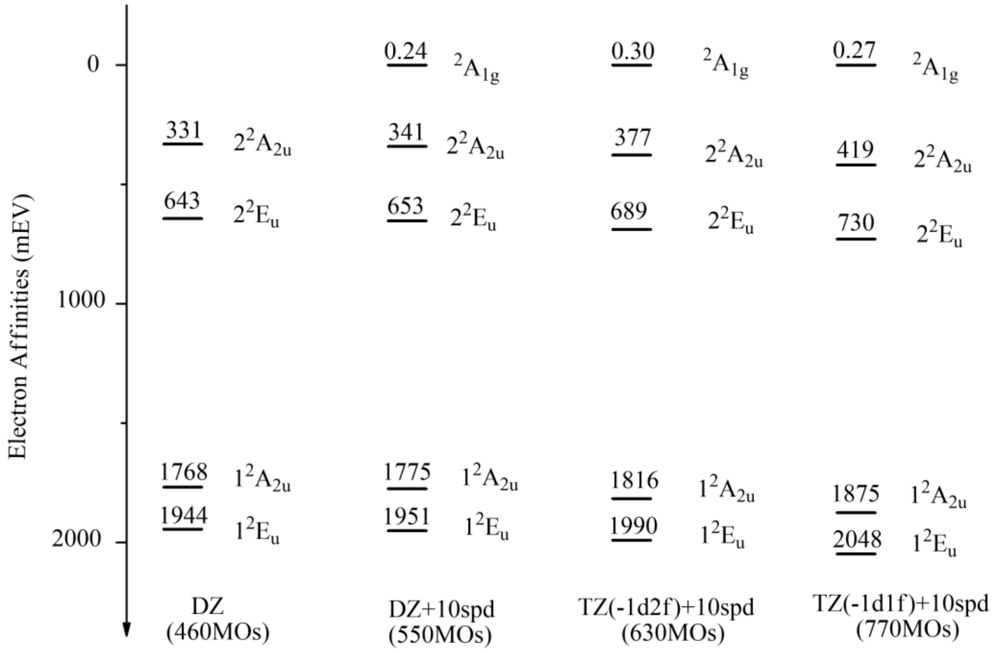

Figure 3.2. The binding energies (meV) of the C_{20} states calculated using the EA-EOM-CCSD method and different basis sets. The $^2A_{1g}$ state is not present in the case of the DZ basis set, since it cannot be described with this basis set due to its lack of diffuse functions.

As shown in Fig. 3.2, one can also infer the basis set effect on the binding energies. With the DZ basis set, both $^2E_u/^2A_{2u}$ pairs are seen to be fairly well described already. The extra basis function of TZ(-1d2f) leads to a moderate increase (by ~50 meV) in the binding energies of the $^2E_u/^2A_{2u}$ pairs. Similarly, there is another ~50 meV increase in binding energy of the $^2E_u/^2A_{2u}$ pairs states, when one employs higher angular momentum f-functions. Thus, we can conclude that the diffuse functions have little effect on the $^2E_u/^2A_{2u}$ pairs. By contrast, the $^2A_{1g}$ state behaves differently. Diffuse functions seem to play the primary role for this state, and without diffuse functions one cannot even recover this state. On the other side, the increase of the atomic basis set from DZ to TZ has almost no effect to this state. Adding f-functions results in a negligible (0.03 meV) decrease of the $^2A_{1g}$ binding energy, although it very likely leads to a somewhat better description of the neutral electronic state. As there are only s-, p- and d-type diffuse function at the center and only weakly bound $^2A_{1g}$ state found, one can expect that adding diffuse f-function will further stabilize the $^2A_{1g}$ state. Referring to the discussion in ref. 115, we are confident that at the complete basis set limit, the $^2A_{1g}$ state will remain bound.

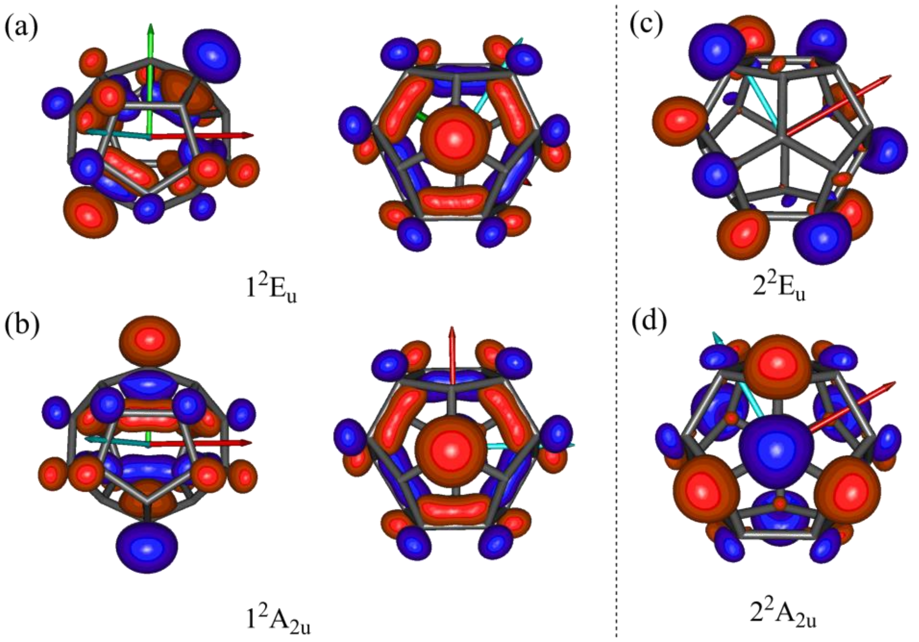

Figure 3.3. Singly occupied natural orbitals (SONOs) associated with the 1^2E_u (a), 1^2A_{2u} (b), 2^2E_u (c) and 2^2A_{2u} (d) states. For the ^2E_u states, the SONO of only one component is shown. For the 1^2E_u and 1^2A_{2u} states two different orientations of the SONOs are shown. In (a) and (b), we presents two figures from different views to show the similarity and difference of 1^2E_u and 1^2A_{2u} states. The red, cyan and green arrows are X, Y and Z axes, respectively. The surfaces enclose 50% of the orbital density.

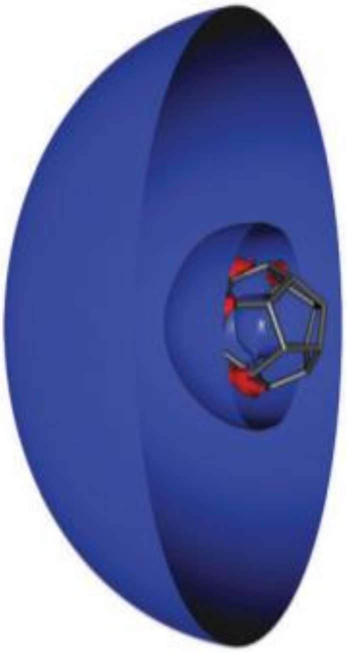

Figure 3.4. The SONO of the $^2A_{1g}$ state. Only one symmetric half of the orbital is shown, with the cutting plane coinciding with the mirror plane of C_{2h} point group used in the calculations. The surface encloses 50% of the orbital density.

According to the above discussion, there are two classes of bound states, namely, the two $^2E_u/^2A_{2u}$ pairs and the $^2A_{1g}$ state, being of different nature. According to the nomenclature applied in the previous work [113–115], the former are referred to as anionic valence states, whereas the latter is a SA state. The different nature of the valence and SA states is clearly seen in the SONO images shown in Fig. 3.3 and 3.4. The valence $^2E_u/^2A_{2u}$ state SONOs are mostly localized around the carbon cage, whereas the a_{1g} orbital of the SA state exhibits a very diffuse and extended pattern, with only some electron density being inside the cage. It can be inferred from the shape of the a_{1g} SONO that the $^2A_{1g}$ state is an s-type SA state, similar to the SA state in C_{60}. However, the a_{1g} SONO of C_{20} has even more diffuse character than the a_g counterpart in C_{60} [113]. This correlates with a much smaller binding energy of the C_{20} SA state (<1 meV) as compared to the C_{60} SA state (~0.13 eV) [112-115].

Interestingly, the SONOs of the first ^2E_u and $^2A_{2u}$ states share a very similar pattern, as shown in Fig 3.3(a) and Fig 3.3(b). Upon a closer inspection of the $^2E_u/^2A_{2u}$ SONO patterns, one can easily find certain differences between two $^2E_u/^2A_{2u}$ pairs. The first $^2E_u/^2A_{2u}$ SONOs exhibit clear p(π) character, while the SONOs of the second pair apparently have some s-type admixtures, resembling sp-hybridized orbitals, with more density outside the cage than inside, as shown in Fig 3.3(c) and Fig 3.3(d). The different character of the two valence state $^2E_u/^2A_{2u}$ pairs, as well as the $^2A_{1g}$ state will be discussed in some detail below.

3.5 Radial and angular distribution of the attached extra electron

The radial density difference distributions $\Delta\rho(r)$ of the five bound anion states of C_{20} are presented in Fig. 3.5. Clearly, the $\Delta\rho(r)$ curves of the $^2E_u/^2A_{2u}$ pairs and the $^2A_{1g}$ state exhibit a different nature. The $\Delta\rho(r)$ curve of the valence states have sharp maxima just beyond the carbon cage. Comparing to $\Delta\rho(r)$ of the valence states, the density of the $^2A_{1g}$ state is distributed over a range one order of magnitude larger. Due to its diffuse nature, $\Delta\rho(r)$ of the $^2A_{1g}$ state is distributed in a ~500 Bohr broad "band". One can also note smaller features of the $^2A_{1g}$ $\Delta\rho(r)$ curve inside the cage (see the inset of Fig. 3.5(b)). In agreement with to our previous discussion, the $\Delta\rho(r)$ analysis unambiguously displays the valence nature of the $^2E_u/^2A_{2u}$ pairs and the SA character of the $^2A_{1g}$ state.

One can have a closer look at the $\Delta\rho(r)$ curves of the valence states i.e., the two $^2E_u/^2A_{2u}$ pairs. Although there is an overall similarity between these two pairs, their $\Delta\rho(r)$ curves show distinctions. Within each pair, the density-difference distributions share a similar pattern, as shown in Fig 3.5. The 1^2E_u and 1^2A_{2u} state of the first pair have almost identical density-difference distributions. Noteworthy, in the fullerene counterpart C_{60}, the $\Delta\rho(r)$ curves of all the four valence states are virtually identical. Apparently the different behavior of the valence states reflects the "non-spherical" C_{20} cage. The non-spherical shape is a result of the lower (D_{3d}) C_{20} symmetry, contrasting the quasi-spherical I_h symmetry of C_{60}. As a consequence, there are 3 distinguished distances (radii) of the C_{20} cage, rather than only one in C_{60}, as shown in Fig. 3.1. One can easily see, r_1, as the largest radius of C_{20}, can be associated with the 1^2E_u and 1^2A_{2u} states (first pair), whereas, r_2' and r_2, as the shorter radii, can be attributed to features in the second $^2E_u/^2A_{2u}$ pair.

The density distributions of the valence states inside the cage are another interesting topic. The different pattern between the first and second $^2E_u/^2A_{2u}$ pairs can be clearly observed, in the region inside the cage. The first pair shares the same pattern in that their Δρ(r) first increases near the cage and then decreases to the minimum at the cage. By contrast, the density of second pair decreases near the cage and little effect to the distribution on the shell. This difference can be explained by the different nature of two pairs of valence states. The similarity between the first pair states of C_{20}^- and the valence states of C_{60}^- indicates that these states are p-type valence states. The second pair states are sp-type rather than p-type, resulting in a different pattern, as discussed in section 3.4.

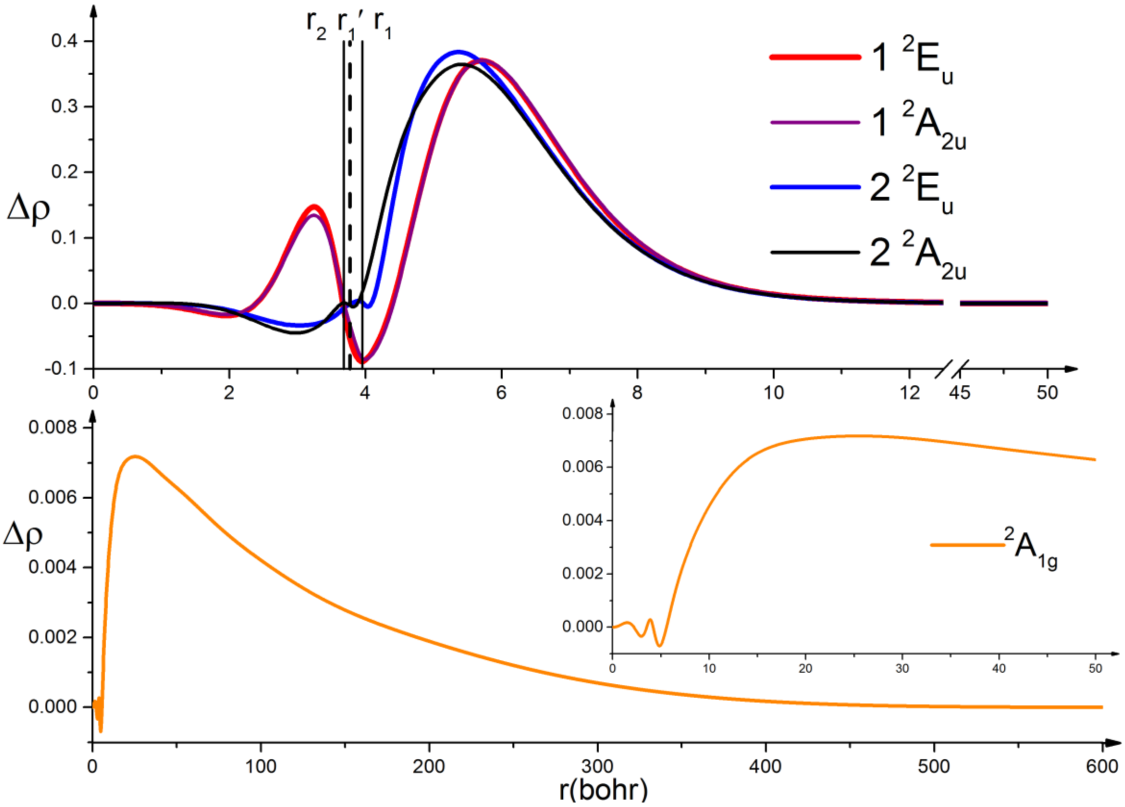

Figure 3.5. Radial distributions of the excess electron density for (a) the four bound valence states, 1^2E_u, 1^2A_{2u}, 2^2E_u and 2^2A_{2u}, and (b) the bound superatomic state, $^2A_{1g}$, of C_{20}. r_1, r_2' and r_2 are the three characteristic radii of C_{20} (see Fig. 3.1).

As shown in Fig. 3.5, the SONO of the superatomic $^2A_{1g}$ state is diffusely distributed over a range of around 500 Bohr. The density maximum is much smaller than in the valence states. Noteworthy, one can observe a tiny amount of electron density distributed inside the cage, which indicates it is superatom molecular orbital and not a Rydberg orbital.

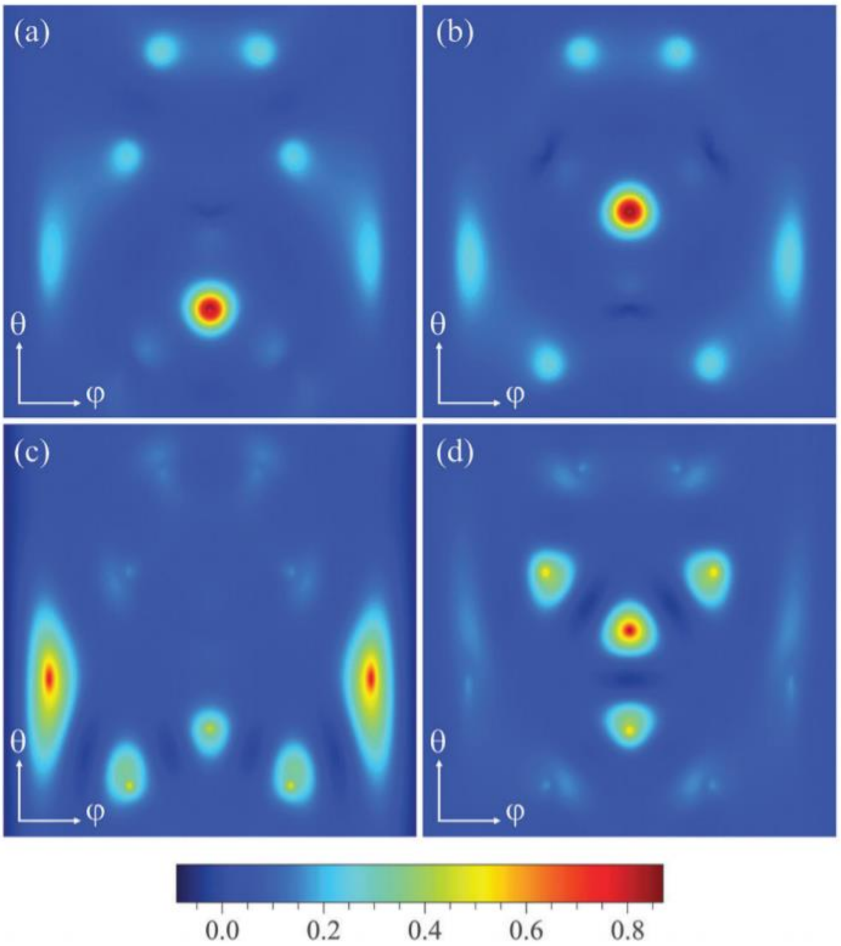

Figure 3.6. Angular distributions of the excess electron density for the four valence states of C_{20}, 1^2E_u (a), 1^2A_{2u} (b), 2^2E_u (c), and 2^2A_{2u} (d). The range of both the azimuthal (θ) and polar (φ) angles is from 0 to π. For the degenerate states, only one component of double degenerate ^2E_u is presented. The corresponding distribution for $\pi \leq \varphi \leq 2\pi$ is identical, since the density is symmetric with respect to φ.

In Fig. 3.6, we show the angular density distributions of the excess electron for the four valence states, that is, the two $^2E_u/^2A_{2u}$ pairs. One can readily see that, the $\Delta\rho(\theta, \varphi)$ distribution of the first pair is more compact than that of the second pair, which, of course, reflects the fact that the second pair possesses smaller binding energies than the first pair. Noteworthy, the similarity of the 1^2E_u and 1^2A_{2u} SONOs appears in the $\Delta\rho(\theta, \varphi)$ pattern as well. The 1^2E_u and 1^2A_{2u} states possess almost identical $\Delta\rho(r)$ and similar $\Delta\rho(\theta, \varphi)$ distributions, being consistent with the similar binding energies of these two states.

In contrast to the first $^2E_u/^2A_{2u}$ pair, the $\Delta\rho(\theta, \varphi)$ distributions of the second pair differ distinctly.

Interestingly, the excess electron of the 2^2E_u state is localized within the lower half of the C_{20} cage, that is between $0 \leq \theta \leq \pi/2$. For the $^2A_{2u}$ state, most of the excess electron is located near the C_3 axis. This is in agreement with the pattern of the 2^2A_{2u} SONO shown in Fig. 3.3(d).

3.6 Applying the charge model to the C_{20}^- anion

To check if there might be further bound states missed in our previous computations, we considered a simple charge model, as applied in a previous study on C_{60}^- [115]. The charge model allows one to survey the manifold of potentially bound anionic states. We applied the charge model to C_{20}^- anion in a similar way is placed as in the C_{60}^- study. Here a variable positive charge is placed at the center of neutral C_{20} cage, supposing here D_{3d} symmetry. In the following, we refer to this model as $C_{20}(+q)$, with the charge varying from 0.0 to +1.0. The binding energies are obtained, according to Koopmans' theorem, as virtual HF orbital energies. The HF computations were performed utilizing the full quadruple-ζ basis set of Dunning (cc-pVQZ) [125], employing the Turbomole program package[134].

In Fig 3.7, we present several lowest electron affinities of $C_{20}(+q)$ as a function of the charge value, based on HF calculations using Koopmans' theorem approximation. One can assess seven valence bound anion states, based on the $C_{20}(+q)$ model. Among them, there are four states corresponding to the two $^2E_u/^2A_{2u}$ pairs discussed above. In addition, there are three other orbitals, $3a_{2g}$, $11e_g$, and $10a_{1g}$, corresponding to $^2A_{2g}$, ^2E_g, and $^2A_{1g}$ states, respectively. These three additional states form of "group", which is energetically well separated from other valence states. While the latter three states are bound for q=1, they soon become unbound when the positive charge is scaled down. To check if any of these three states predicted by the $C_{20}(+q)$ model for q=1, we carried out complementary EA-EOM-CCSD calculations with full triple-ζ (cc-pVTZ) basis set. However, these calculations show that none of these three states is bound at such high computational level.

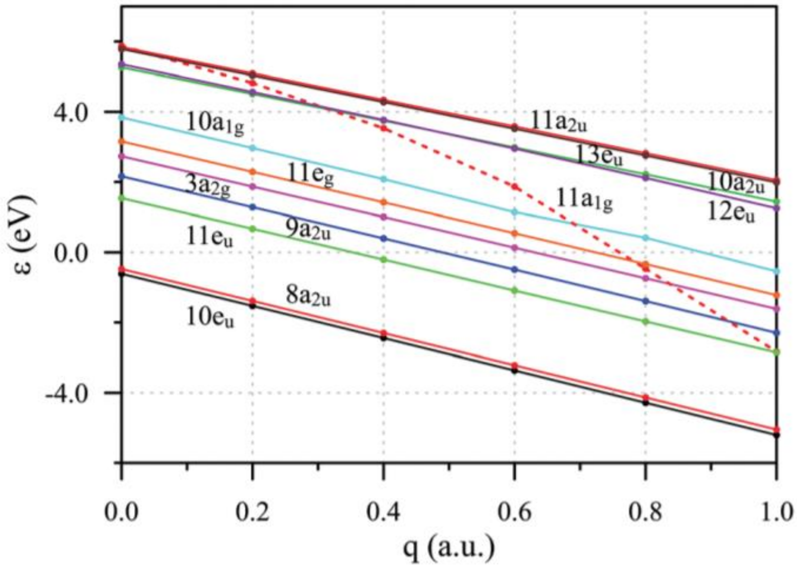

Figure 3.7. Electron affinities (ε) at the HF (Koopmans' theorem) level for the $C_{20}(+q)$ model as functions of the positive charge q at the center of the C_{20} cage calculated using the cc-pVQZ basis set. The full lines correspond to the valence states, the dashed line corresponds to the SA state.

The charge model allows one to assess and characterize all potential bound atomic states by inspecting the manifold of bound HF orbitals for q=1 and tracking their behavior as q is scaled down to zero. HF states had become unbound at q=0 may still have exact bound counterparts as a result of the polarization effect, e.g. electron correlation, etc. This can be checked by performing post-HF computations for the respective candidates.

These remarks apply both to valence and SA states. As an interesting additional feature, the charge model allows for a clear distinction of the valence and SA states. While the valence states in Fig. 3.7 show a uniform linear dependence on the charge parameter, the curve of the single SA state is strikingly different. It suggests that one can use the $C_{20}(+q)$ model predict bound SA state and survey the entire manifold of possible bound anion states.

3.7 Comparison with experiment

One may wonder to what extent our results are consistent with experiment. The experimental data based on photoelectron spectroscopy, report the adiabatic electron affinity (AEA). Thus, the comparison with experiment requires an accurate description of the ground state energies of C_{20} and C_{20}^{-} at their respective optimized geometries.

Due to the high computational cost, we only calculate the AEA of the ground state. Before one can start the calculation, some considerations concerning the basis sets are required. Although the results based on Dunning's double-ζ basis set have well described the bound states of C_{20}^{-} anion, an increase of the basis set still results in a considerable binding energy increase, as discussed above. Thus, to obtain a sufficiently accurate electron affinity, comparable to experiment, a much better basis set than Dunning's double-ζ basis set is needed. Moreover, since calculations with different basis sets result in different PES minima high-level basis sets have to be used in the geometry optimization as well to reduce the error. In the case of adiabatic electron affinities this means to optimize the geometries of both the neutral and anion ground states with reliable methods.

Here, we employed the cc-pVTZ basis set associated with CCSD (for the neutral geometry) and EA-EOM-CCSD (for the anion geometry) optimizing geometry, based on analytical gradients of total energies, using the CFOUR program package. The equilibrium geometries are shown in Fig 3.8, with parameters. The bond lengths are similar to those obtained at CCSD/cc-pVTZ level in ref. 124. Comparing to the equilibrium geometry shown in Fig. 3.1, the bond lengths are moderately decreased by ~0.02 Å. For the C_{20}^{-} anion, we optimized the geometry within both the D_{3d} and D_{2h} conformations at the EA-EOM-CCSD/cc-pVTZ level, and found that the D_{2h} form is energetically more favorable. The parameters of ground states geometry are shown in Fig 3.8.

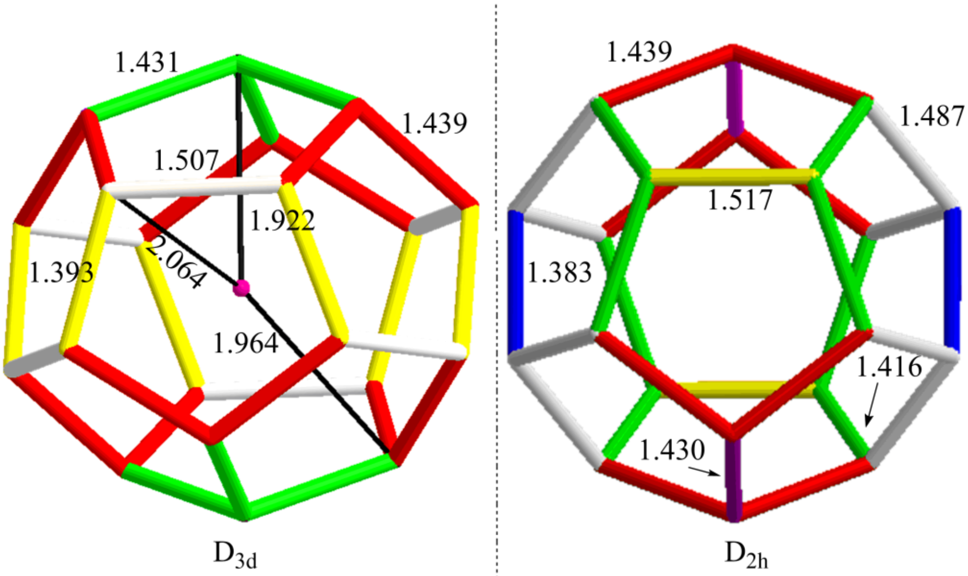

Figure 3.8. Ground state D_{3d} structure of the neutral C_{20} and D_{2h} structure of the C_{20}^{-} anion, obtained from CCSD/cc-pVTZ and EOM-CCSD/cc-pVTZ geometry optimization, respectively. The equivalent (symmetric) bonds are indicated by the same color. All units are in Å.

After geometry optimization, we also calculated the vertical electron affinity utilizing the larger Roos full triple-ζ basis set. The results are shown in Table 3.2. As one can see, the VEA (1.97 eV) is smaller than the largest binding energy in Fig 3.2. This is due to the improved C_{20} ground state geometry obtained using the cc-pVTZ basis rather than the cc-pVDZ. The AEA result (2.23 eV) is in remarkably good agreement with the experimental value (2.25 eV) [119]. It proves the validity of our methods and geometry optimization.

Table 3.2. The adiabatic and vertical electron affinities of the C_{20}^{-} anion, obtained with Roos triple-ζ basis sets, based on CCSD/cc-pVTZ (neutral) and EOM-CCSD/cc-pVTZ (anion) calculations, respectively.

equilibrium geometry	Total energy of C_{20} (a.u.)	Total energy of C_{20}^{-} (a.u.)	VEA(eV)	AEA(eV)
at neutral ground state geometry	-760.441850	-760.514234	1.97	
at anionic ground state geometry	-760.431983	-760.523793		2.23

3.8 Conclusions

By employing the state-of-the-art EA-EOM-CCSD method and using reliable basis sets, a thorough study of the smallest fullerene C_{20}^{-} anionic bound states has been performed. Based on calculations of the C_{20} neutral ground state in D_{3d} equilibrium configuration, we found that the C_{20}^{-} anion exhibits five bound electronic states. Also, with the help of larger basis sets, we obtained an AEA in excellent agreement with the experimental results, which validates the quality of our approach. Among the bound states, 1^2E_u, 1^2A_{2u}, 2^2E_u and 2^2A_{2u}, known as the valence states, possess relatively strong binding energies (from 2.05 eV to 0.4 eV). Similar to the C_{60}^{-} anion, there is one superatomic state $^2A_{1g}$, but it is weakly bound (~1 meV binding energy). Analyzing with radial and angular density distributions of the excess electron, one can easily identify those states. Comparing to the compact valence states, the extra electron density of the SA state is distributed over a long range (as much as ~500 Bohr), resulting in an broad band. Although the valence states have similar the radial distributions, the first and second $^2E_u/^2A_{2u}$ pairs feature notable differences, due to the non-spherical form of C_{20}. Analogously, other non-spherical fullerenes, e.g., C_{70}, can be expected to have similar pattern. Moreover, the two $^2E_u/^2A_{2u}$ pairs exhibit different characters, as the first and second pairs are with p(π) and sp character, respectively.

The charge model in C_{20} is not as successfully as its application in C_{60} [115]. Here it can predict the SA states and provide a survey for entire manifold of possible bound anion states. It predicted three additional bound valence states, which are not bound states based on our EA-EOM-CCSD calculation, at the neutral ground state equilibrium geometry. Of course, it is possible that these three states are ‘‘adiabatically bound’’, and become bound states at different geometries. Apart from the failure of overestimating the bound valence states, the prediction of the charge model on the SA state is correct, and the $^2A_{1g}$ state has been successfully identified by our EA-EOM-CCSD calculations.

Chapter 3

Chapter 4

Charge Separated States of Li@C_{20}: Electronic States of Small Endohedral Fullerene

4.1 Background and motivation

When one or several atoms are encapsulated inside one fullerene, this kind of system is referred to as an endohedral fullerene and the atoms are called guest atoms. After decades of research, many unique properties of this fullerene derivatives have been revealed, triggering extensive investigations on both the theoretical [135-137] and experimental sides [23, 138-140]. The Buckminsterfullerene C_{60}, as the most well-known fullerene, plays an important role in the large endohedral fullerene family, i.e., X@C_{60} [104, 141-145]. One of the members of this family, Li@C_{60}, has attracted particular attention. Its applications play unique roles in different fields, such as electron acceptor [146], superconductive agent [147], reductant [148], and electron buffer [149].

Some endohedral fullerenes can form a system with a fullerene anion and guest atom cation, namely with a charge separated (CS) character [148, 150], which leads to their intriguing properties. In Li@C_{60}, C_{60} is an electron acceptor [150], “stealing” a valence electron from the lithium atom, the electron donor. One can easily find that a considerable amount of this “stolen” electron charge is distributed on the C_{60} cage boundary. Hence one can approximately treat this state as a combination of a C_{60}^{-} fullerene anion and a Li^{+} cation. However, there are still non-charge-separated states, and we will have a closer look on non-charge-separated bound states of large endohedral fullerenes of Li in chapter 5.

As the only fullerene exclusively formed by pentagons (the smallest building block of fullerenes),

C_{20} has attracted much attention [119, 124, 151-153]. Its considerable electron binding energy (EBE), is comparable to C_{60} (2.25 eV for C_{20} [119] and 2.69 eV for C_{60} [154]). As discussed in chapter 3, C_{20}^{-} can form several bound *valence* and *superatomic* (SA) states, which is similar to the case of C_{60}^{-} [112-115]. Our computations [155], based on the EA-EOM-CCSD method [43], established four valence states and one SA state as bound states of C_{20}^{-}. Similar to the parent fullerenes, valence and SA states are two important types of endohedral fullerenes states. Thus, it is worthwhile to have a closer look at the valence and SA states of $Li^{+}@C_{20}^{-}$, since one can expect that $Li^{+}@C_{20}^{-}$ has promising applications. As mentioned in chapter 3, SA and Rydberg states have difference nature. While considerable electron density of the former distributed inside the cage, the extra electron of the latter is essentially delocalized outside the cage [156].

As mentioned in the first chapter, the difference in electron distribution of valence and SA states reflects their different nature. In the case of fullerenes, the long-range effect of image charges and image potentials gives rise lead to the forming of SA states [20-22]. In the case of endohedral fullerenes, the guest atom/ion also contributes to the formation of the SA states by providing real charges and real potentials, which associate with adding to the fullerene image charges and potentials from fullerene. There has been a study of one noble gas guest atom inserted into a C_{60} cage [118]. The results of this study show that the noble gas guest atom strongly influences the SA states, while the binding energies of the valence states change only little, as do their excess electron distributions. As the previous study has shown, noble gas guest atoms have a perturbative effect on the SA states of endohedral fullerenes, e.g., $He@C_{60}^{-}$ and $Ar@C_{60}^{-}$ [118]. As Li^{+} is isoelectronic to He, one can expect that Li^{+} may have a similar perturbative effect in $Li^{+}@C_{20}^{-}$. Of course, there is an additional Coulomb effect due to positive charge, which makes the Li^{+} guest cation a particularly interesting case.

In the following, we will study the complex effect of the Li^{+} guest cation in the smallest fullerene, C_{20}. Although there are several previous reports on the $Li^{+}@C_{20}^{-}$ system [157,158], to the best of our knowledge, these were confined to the level of density functional theory (DFT) level. As shown in a previous study [113], one needs a more accurate method, such as EA-EOM-CCSD, to properly describe the long-range effect on the fullerene bound states. As here the CS states are neutral states, we prefer to call the relative excitation energies electron-binding energies (EBEs) rather than electron affinities. We also introduce the concept of excess electron density, meaning the electron density difference of the latter two states.

The chapter is organized as follows. In section 4.2, we discuss the computational details of our EA-EOM-CCSD calculations. In section 4.3, we give a short discussion of the ground state structure of $Li^+@C_{20}^-$. In section 4.4, the binding energies of the CS bound states, both valence and SA states, are presented. In section 4.5, based on the EA-EOM-CCSD results of section 4.3, we discuss the singly occupied natural orbitals of valence and SA states. In section 4.6, a radial distribution analysis is presented for both valence and SA states. In the final section 4.7, we present conclusions based on the findings in the previous sections.

4.2 Computational details

As a closed-shell system, the ground state of $Li^+@C_{20}$ cation is suitable as a reference state for the calculation. Our EA-EOM-CCSD computations for neutral $Li@C_{20}$ were obtained employing the ground state of $Li^+@C_{20}$ cation (at equilibrium geometry) as reference state. We carried out a full ground state geometry optimization of $Li^+@C_{20}$ to find the thermodynamically most favorable configuration, employing both MP2 [126] and DFT/WB97XD [159] computations with Dunning's double-ζ basis set (cc-pVDZ) [125]. In the geometry optimization, no symmetry restrictions were applied. The Gaussian 09 program package was used in the geometry optimizations [160]. Additionally, we also performed CCSD [57] computations, using Dunning's double-ζ basis set and Dunning's triple-ζ basis set without f functions, for a full ground state geometry optimization of $Li^+@C_{20}$ (with D_{3d}, D_{2h}, D_{5d}, and C_{2h} configuration). Here the Molpro [129] and CFOUR [131] program packages were used. To save computational cost, the 20 carbon core orbitals were kept frozen. The analysis of Li@C20 bound states was based on the CCSD optimized geometry.

All the states of neutral Li@C_{20} were calculated as an electron attachment to the Li^+@C_{20} cation, using the EA-EOM-CCSD method. Unlike in the calculations presented in chapter 3, where several basis sets were employed, here, only two basis sets were employed. The first one is a double-ζ basis set, which was constructed starting from Dunning's standard cc-pVDZ basis set. We further augmented that basis for carbon with one diffuse s-function from the aug-cc-pVDZ basis set. For lithium, the basis set was augmented with two diffuse s-, three diffuse p-, and four diffuse d-type functions, which is consistent with the basis sets used in the previous work on C_{60} [115]. The exponents of the augmented diffuse functions were generated starting from the last exponents of the aug-cc-pVDZ basis, applying an even-tempered series $a_{n+1} = a_n/3.5$. In the following, this basis is referred to as DZ+. Similarly, we constructed a triple-ζ quality basis set starting from the cc-pVTZ set without the f-functions. Also the lithium cc-pVTZ(-f) basis set was augmented with two diffuse s-, three diffuse p-, and four diffuse d-type functions, using a similar even-tempered series for the exponents. This basis is referred to as TZ+ in the following sections. The DZ+ and TZ+ basis sets give rises to 354 and 543 molecular orbitals (MOs), respectively. The carbon and lithium 1s core orbitals were not frozen for technical reasons related to the computation of electron densities as well as single occupied molecular natural orbitals. All the coupled cluster calculations were carried out with the CFOUR package.

We also employed the so-called Δρ analysis, as presented in chapter 3. The only difference is replacing the density of the C_{20}^- anion with that of neutral Li@C_{20} and the density of neutral C_{20} with that of cationic Li^+@C_{20}:

$$\Delta\rho(r) = \rho_N(r) - \rho_C(r)$$

To better understand the nature of the Li@C_{20} bound states, we introduce the integrated excess electron density I(R),

$$I(R) = \int_0^R \Delta\rho(r)\, dr$$

which accounts for the charge inside a sphere of radius R.

4.3 Ground state structure of the $Li^+@C_{20}$ cation

There was a series of previous theoretical studies on $X@C_{20}$ endohedral ground state structures [135, 161–163]. All these studies concluded that the guest atoms are residing at the cage center. By contrast, experimental [103] and theoretical investigations [164] suggested that in larger endohedral fullerenes like $Li@C_{60}$ the guest atom resides off-center. We found that the center position of Li in large endohedral $Li@C_n$ fullerenes is energetically favored in some cases, as will be discussed in chapter 5. We have verified, based on DFT/cc-pVDZ geometry optimization that the minimum of $Li^+@C_{20}$ could only be found if Li^+ is positioned at the center. According to this result, we assume that in $Li^+@C_{20}$ the Li^+ guest cation is residing at the center.

Table 4.1 Relative energies for different symmetries of the $Li^+@C_{20}$ structure with different methods.

Symmetry	WB97XD/cc-pVDZ	Relative Energy(kcal/mol)	Type
C_i	-768.479928	0.00	Minimum
D_{2h}	-768.479395	0.33	Saddle
D_{3d}	-768.479864	0.04	Minimum
C_{2h}	-768.479831	0.06	Minimum
Symmetry	MP2/cc-pVDZ	Relative Energy(kcal/mol)	Type
C_i	-766.534855	0.00	Minimum
D_{2h}	-766.533784	0.67	Saddle
D_{3d}	-766.534855	0.00	Minimum
C_{2h}	-766.534855	0.00	Minimum

In this chapter, we only consider the lithium residing at the center of a C_{20} fullerene cage. As discussed in chapter 3, the I_h conformation of neutral C_{20} is Jahn-Teller unstable. Due to Jahn-Teller distortion the geometry would possibly turn into D_{5d}, D_{3d}, or D_{2h} form [155]. As shown in Table 4.1 and 4.2, we optimized geometries of $Li^+@C_{20}$ starting from different initial structures to find the true ground state. The MP2/DFT results show that, similar to the C_{20} cage, D_{3d} structure is energetically favored. The later calculation also proves that D_{3d} geometry is energetically more favorable than D_{2h}, with a relatively small energy gap at CCSD/cc-pVDZ level. In Fig. 4.1, we present the D_{3d} equilibrium geometries of C_{20} and $Li^+@C_{20}$ at CCSD/cc-pVDZ level, along with structural parameters.

Table 4.2 Relative energies for different symmetries and different basis of the $Li^+@C_{20}$ structure at the CCSD level with frozen 1s orbitals of carbon.

CFOUR	CCSD/cc-pVDZ (a.u.)	Relative energy(kcal/mol)
D3d (20-13-16-12)*	-766.417095	0.00
D2h	-766.416206	0.56
D3d (20-12-17-12)	-766.402098	9.41
C2h (20-13-16-12)	-766.416653	0.28
D5d (20-12-17-12)	-766.395850	13.33
Molpro	CCSD/cc-pVDZ (a.u.)	Relative energy(kcal/mol)
D3d (20-13-16-12)	-766.416031	0.00
D2h	-766.415135	0.56
CFOUR	CCSD/cc-pVTZ-f(4s3p2d) (a.u.)	Relative energy(kcal/mol)
D3d (20-13-16-12)	-766.783470	0.00
D2h	-766.782634	0.52

* The occupation numbers of every irreducible representation are shown in bracket.

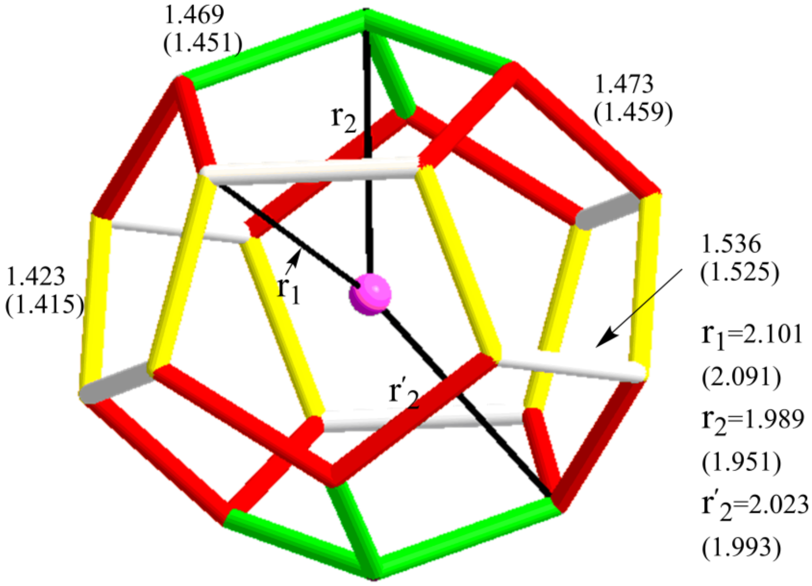

Figure 4.1. Ground state D_{3d} structure of $Li^+@C_{20}$ and C_{20} (in brackets) obtained from CCSD/cc-pVDZ geometry optimization. The four nonequivalent C-C bond lengths are indicated by colors. r_1, r_2, and r_2' denote the three characteristic radii from the center. All the units are in Å.

Obviously the parameters of $Li^+@C_{20}$ are increased as compared to the parent C_{20} fullerene because of the perturbative effect of the Li^+ guest cation. Due to the non-spherical shape, the changes depend on the directions: r_2 and r_2' (around 0.03 Å) increase more than r_1 (only 0.01 Å). Thus, the radius of the cage expands more in the direction of the C_3 axis. Based on this optimized $Li^+@C_{20}$ geometry, we performed calculations of the neutral $Li@C_{20}$ states employing the EA-EOM-CCSD method. The possibility of using an Abelian subgroup (in this case C_{2h}), benefits the EA-EOM-CCSD calculations as this reduces significantly the computational cost, which otherwise would have been prohibitive.

4.4 Charge separate states of $Li@C_{20}$

According to the EA-EOM-CCSD/TZ+ results, there are as many as 36 bound states and all of them are CS states. For simplicity, only valence and superatomic CS states with EBEs higher than 1.0 eV are presented in Fig 4.2.

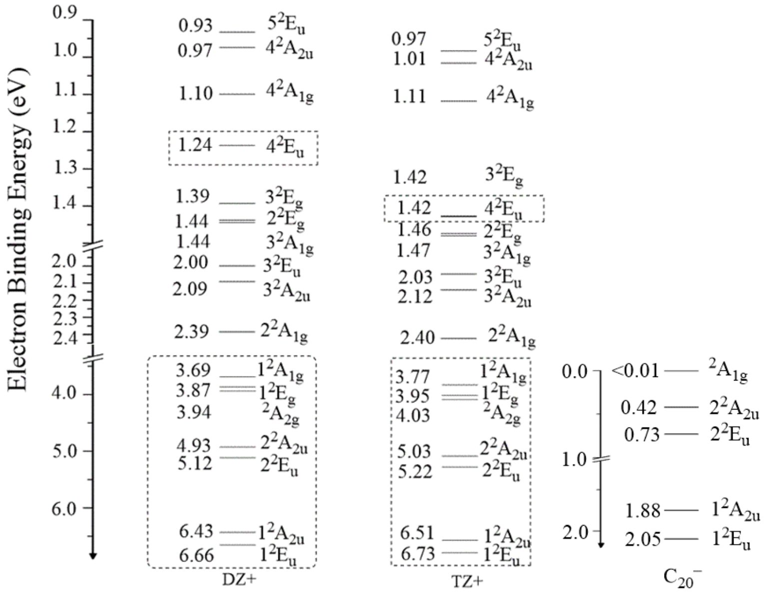

Figure 4.2 Term scheme of electron binding energies for the charge separated bound states of $Li^+@C_{20}^-$ at the EA-EOM-CCSD/DZ+ and TZ+ level. Bound states of C_{20}^- at the EA-EOM-CCSD/RoosTZ(-1d1f) level [155] are listed in the third column. The states can be categorized into two types: valence and SA states. States in dashed rectangles are valence states. The energies of 3^2A_{1g} and 2^2E_g of $Li^+@C_{20}^-$ at the DZ+ level and 3^2E_g and 4^2E_u at the TZ+ level are similar and differ at the third digit. Note that all computed states of $Li@C_{20}$ are the charge separated states characterized as $Li^+@C_{20}^-$.

As shown in Fig 4.2, one can easily distinguish valence and superatomic CS states, based on their different nature. The increase of basis functions from DZ+ to TZ+ leads to a moderate increase of the EBEs for all CS states, by ~0.1 eV. It seems that the DZ+ basis is sufficient to describe both the valence and superatomic CS states well, and the extra p and d functions in the TZ+ basis are not significant for a better description of these states.

4.4.1 Valence charge separated states of Li@C_{20}

As shown in Fig. 4.2, there are 8 valence states, enclosed in dashed rectangles. They can be classified in two sets: (i) two $^2E_u/^2A_{2u}$ pairs, whose counterparts are bound in C_{20}^- as discussed in chapter 3, and (ii) $^2A_{2g}$, 1^2E_g , 1^2A_{1g} , and 4^2E_u without bound counterparts in C_{20}^-.

Comparing to their counterparts in C_{20}^-, the EBEs of the valence states in group (i) have considerably increased. Similar to the states in C_{20}^-, the two $^2E_u/^2A_{2u}$ pairs are separated by an energy gap (>1eV), while the ^2E_u and $^2A_{2u}$ states of the same pair are close in energy. For example, at the TZ+ level, the EBEs of the first pair of states are 6.73 eV and 6.51 eV, respectively, to be compared to their counterparts in C_{20}^- , 2.05 and 1.88 eV. The EBEs of the second pair in $Li^+@C_{20}^-$ are 5.22 and 5.03 eV, compared to their counterparts in C_{20}^-, 0.73 and 0.42 eV. Thus, the presence of the Li^+ cation causes an EBE increase of around 4.5 eV.

As a consequence of the Coulomb effect of the Li^+ guest cation, there are more bound valence states in $Li^+@C_{20}^-$ than in the parent fullerene. The EBEs of $^2A_{2g}$, 1^2E_g , and 1^2A_{1g} are between 4.03 eV and 3.77 eV. The 4^2E_u state is well separated from the other states of both group (i) and (ii), having a relatively small EBE (1.42 eV). These results underline the importance of relying on an accurate method, such as the EA-EOM-CCSD method, well equipped to capture the physical effects beyond the HF description.

4.4.2 Superatomic charge separated states of Li@C_{20}

While in C_{20}^{-} the SA states are the sole result of the image charge [18, 21], the SA states in Li^{+}@C_{20}^{-} are due to the combined effect of image charge and the real charge by the Li^{+} cation. As a result of the Coulomb attraction of the Li^{+} cation, there are more superatomic CS states in Li^{+}@C_{20}^{-}. As in the valence states, we focus on the relatively strongly bound SA states with EBEs >1.0 eV. Noteworthy, one can find a gap (1.3–1.4 eV) between the first superatomic state and the valence states next to it. One can conclude that the Li^{+} cation has a stronger stabilizing effect on the valence states than the SA states, as in the valence states the extra electron charge is distributed closer to the center. Compared to the 4.5 eV increase of the valence state EBEs due to the Li^{+} guest cation, the EBE of the lowest SA state, $^{2}A_{1g}$, only increases by 2.4 eV. Thus, it is interesting to compare the EOM energies with HF orbital energies of the cation (Koopmans' theorem). We present the HF energies of all SA states in Table 4.3, at Koopmans' theorem level. The energetic difference between these two methods range from about 0.5 eV ($2^{2}A_{1g}$, strongest bound SA state) to 0.1 eV ($5^{2}E_{u}$, weakest bound SA state). This essentially reflects the diminishing strength of the polarization effect with decreasing binding energy.

Table 4.3 Binding energies at HF level (Koopmans' theorem) of all superatomic states shown in Fig. 4.2.

States	binding energy at HF level(eV)	type of superatomic state
$2^{2}A_{1g}$	1.92	s-type
$3^{2}A_{2u}$	1.70	p-type
$3^{2}E_{u}$	1.62	p-type
$3^{2}A_{1g}$	1.24	d-type
$2^{2}E_{g}$	1.23	d-type
$3^{2}E_{g}$	1.20	d-type
$4^{2}A_{1g}$	0.99	s-type
$4^{2}A_{2u}$	0.86	p-type
$5^{2}E_{u}$	0.84	p-type

Towards lower EBEs, the SA states of Li@C_{20} form a Rydberg series converging to the zero EBE threshold. Within the limitations of the given basis set, the lowest members of this series can be reasonably well described by the virtual HF orbitals and energies of the Li^{+}@C_{20} ground state.

4.5 Singly occupied molecular natural orbitals for $Li^+@C_{20}^-$

The valence and superatomic CS states are of different nature, and by visualizing the SONOs shown in Fig. 4.3 and 4.4, one can easily see these differences.

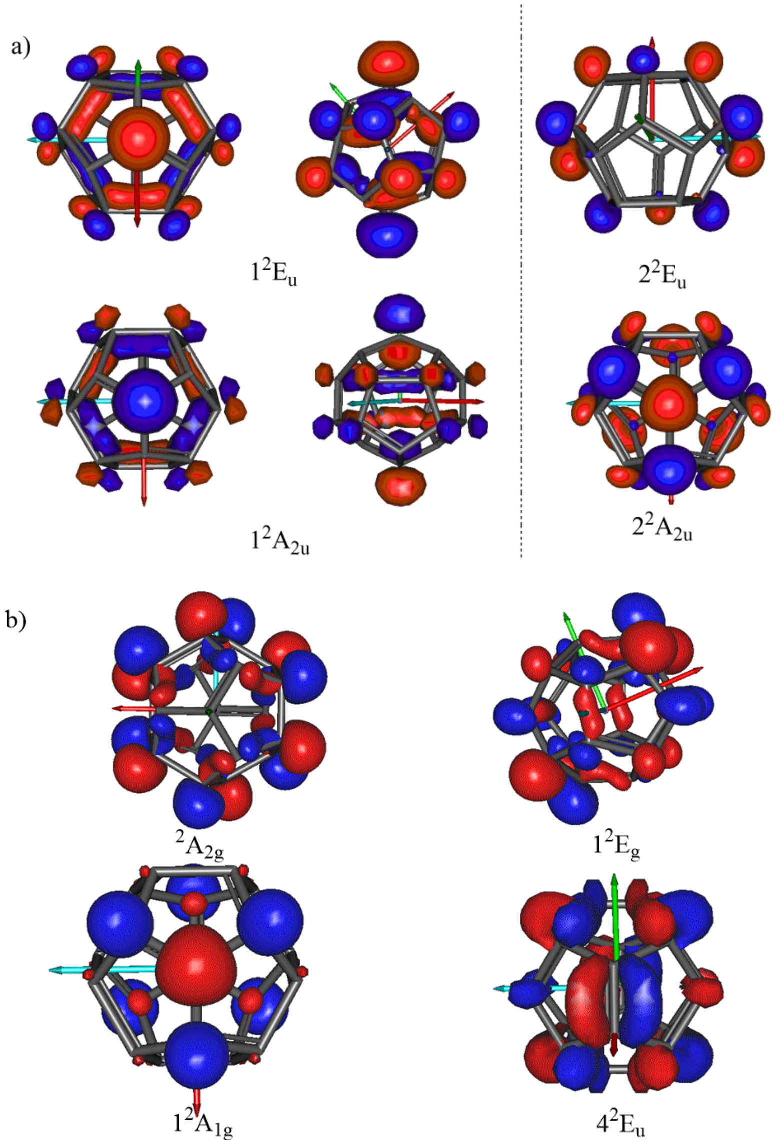

Figure 4.3. Singly occupied molecular natural orbitals of the valence charge separated states of $Li^+@C_{20}^-$. (a) Valence states in group (i) and (b) valence states in group (ii). For the ^2E_u states, the singly occupied molecular natural orbitals of only one component are shown. For the 1^2A_{2u} and 1^2E_u states, two different orientations of singly occupied molecular natural orbitals are shown. The surface encloses 50% of the orbital density. The red, cyan, and green arrows depict the X, Y, and Z axes, respectively

Similar to the valence states in C_{20}^-, the SONOs of valence states essentially distribute the extra electron charge around the edge of the carbon cage, such as in the $^2E_u/^2A_{2u}$ pairs shown in Fig. 4.3(a). As seen in Fig. 4.3, the SONOs of the first $^2E_u/^2A_{2u}$ pair, a_{2g} , $1e_g$, and $1a_{1g}$ exhibit clear p(π) character. However, the orbitals of the second $^2E_u/^2A_{2u}$ pair are sp-hybridized, distributing much of the p-cloud outside the cage, as shown in Fig. 4.3(b). The 4^2E_u valence state shares similar features.

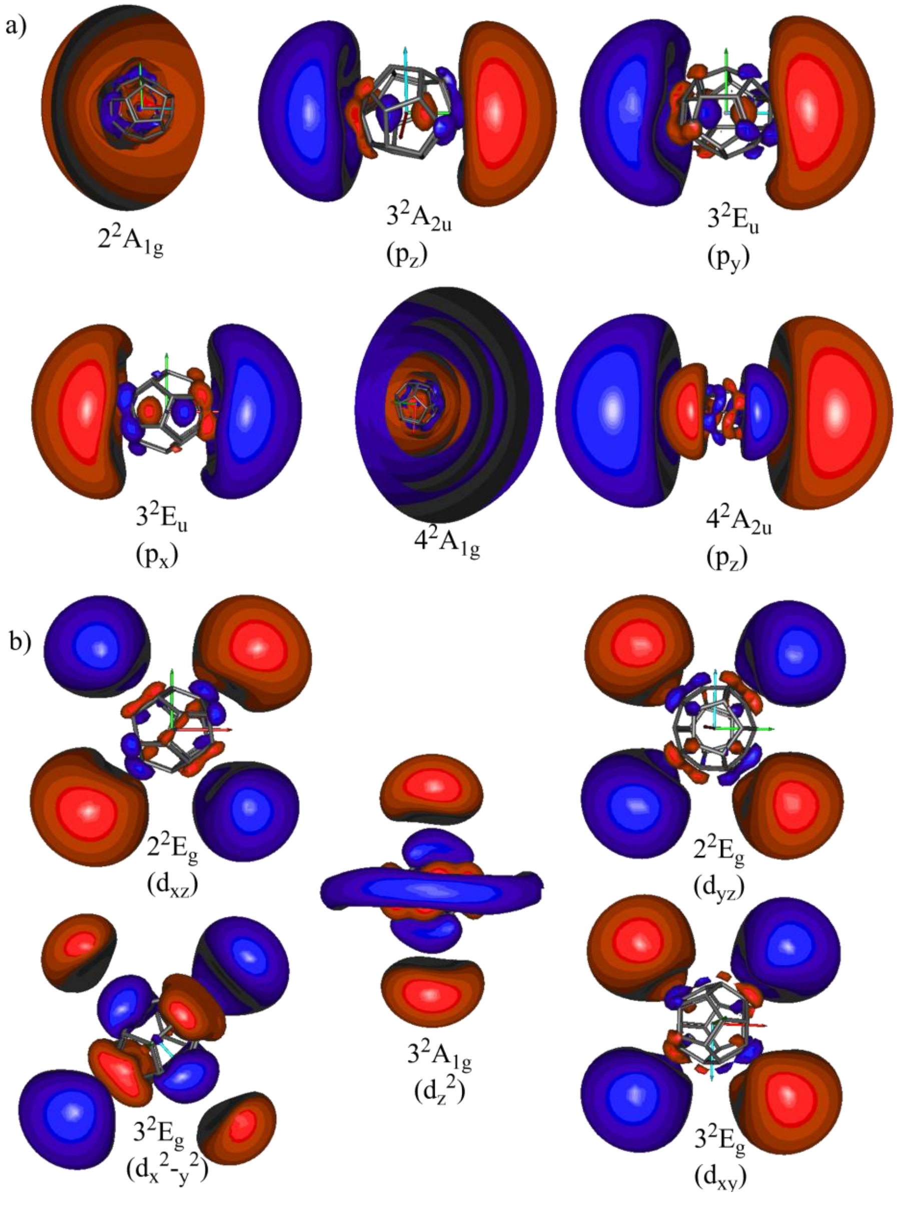

Figure 4.4. Singly occupied molecular natural orbitals of the superatomic charge separated states of $Li^+@C_{20}^-$, (a) s- and p-type superatomic charge separated states and (b) d-type superatomic charge separated states. For example, p_z and d_{xy} stand for p- or d-type singly occupied molecular natural orbitals of degenerate states of E_u and E_g symmetry, respectively. The surface encloses 50% of the orbital density. The red, cyan and green arrows depict the X, Y and Z axes, respectively.

In the superatomic SONOs depicted in Fig. 4.4, one can distinguish atomic s-, p-, and d-type character. The $2a_{1g}$ orbital associated with the 2^2A_{1g} SA state is an s-type atomic orbital. The $2a_{1g}$ orbital is similar to the corresponding SAMOs in C_{20}^- and C_{60}^-. The following three states, comprising the doubly degenerate 3^2E_u and the non-degenerate 3^2A_{2u} states, form another cluster of states, associated with p_x, p_y and p_z type SONOs, where the z axis is the C_3 axis of the C_{20} cage. The slightly higher EBE of the 3^2A_{2u} state indicates a somewhat stronger effect of the Li^+ cation along the z-direction.

The 4^2A_{1g} state, following the first s- and p-type superatomic CS states, corresponds to the next s-type SONO. Its special feature is a node in the radial function of the s orbital, which we will discuss in the section 4.6. Similarly, the energetically close 4^2A_{2u} and 5^2E_u states can be regarded as the three components of an excited p-type orbital. In Fig. 4.4(a) only the 4^2A_{2u} SONO is shown: the EBE of the doubly degenerate 5^2E_u state is already below 1 eV, that is, out of the energy range considered here.

A cluster of 5 SA states is presented in Fig. 4.4(b), including the non-degenerate 3^2A_{1g} and the doubly degenerate 2^2E_u and 3^2E_u states. The corresponding SONOs nicely show the characteristics of the 5 components of a d-function set, namely, d_{xz}, d_{yz}, d_{xy}, d_{z^2} , and $d_{x^2-y^2}$.

4.6 Radial distribution of the excess electron of $Li^+@C_{20}^-$

The radial density-difference distributions $\Delta\rho(r)$ of the $Li^+@C_{20}^-$ states are shown in Fig. 4.5(a) (valence states) and Fig. 4.5(b) and (c) (superatomic states). Also, we present the excess charge I(R) in Figures 6(a) and 6(b). Similar to the Fig. 3.5 in chapter 3, we list three different radii in Fig. 4.5, as the C_{20} cage is “non spherical”.

4.6.1 Radial distributions of valence charge separated states

As shown in Fig 4.5(a) and 4.6(a), all states are CS states with low density near the center, feature a broad peak around 5 Bohr, and fall off to zero before 10 Bohr. Correspondingly, the integral excess charge I(R) converges to 1 before 10 Bohr, as shown in Fig. 4.6(a).

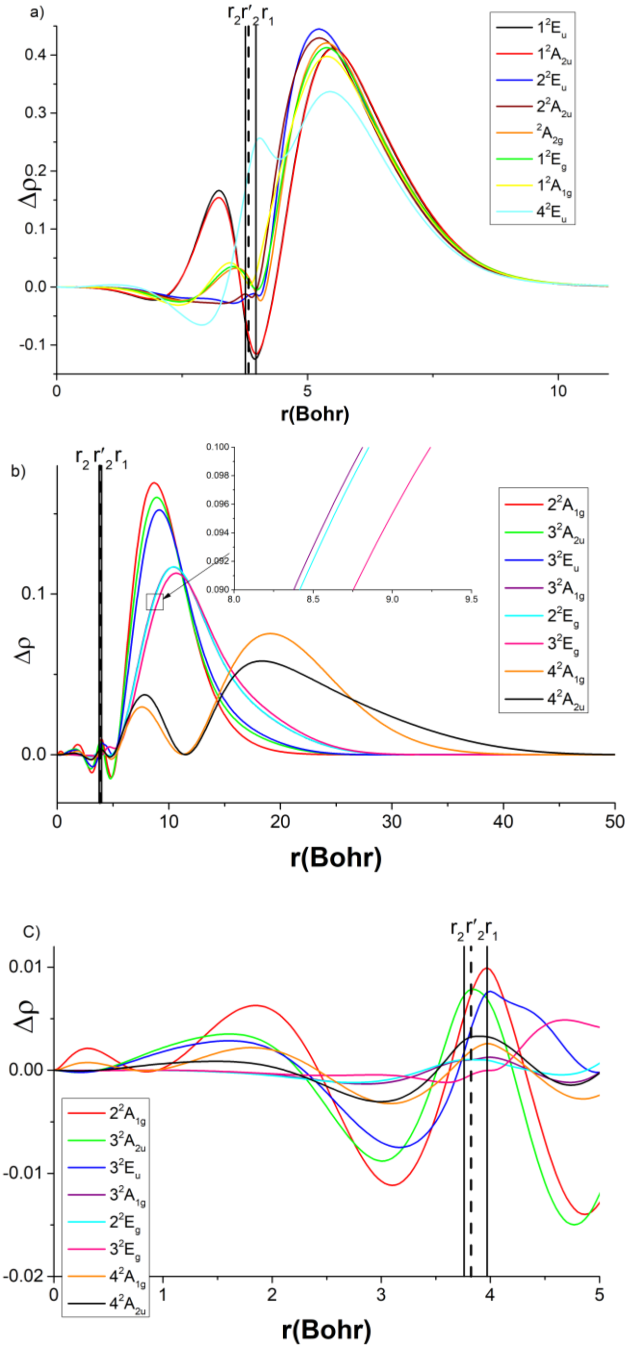

Figure 4.5. Radial distributions of the excess electron density of charge separated states in $Li^+@C_{20}^-$ with electron binding energy higher than 1.0 eV. The excess electron is defined with respect to $Li^+@C_{20}$ (see text). (a) Valence states, (b) superatomic states, and (c) inner part of (b). r_1, r_2, and r_2' are the three characteristic radii from the center of the cage.

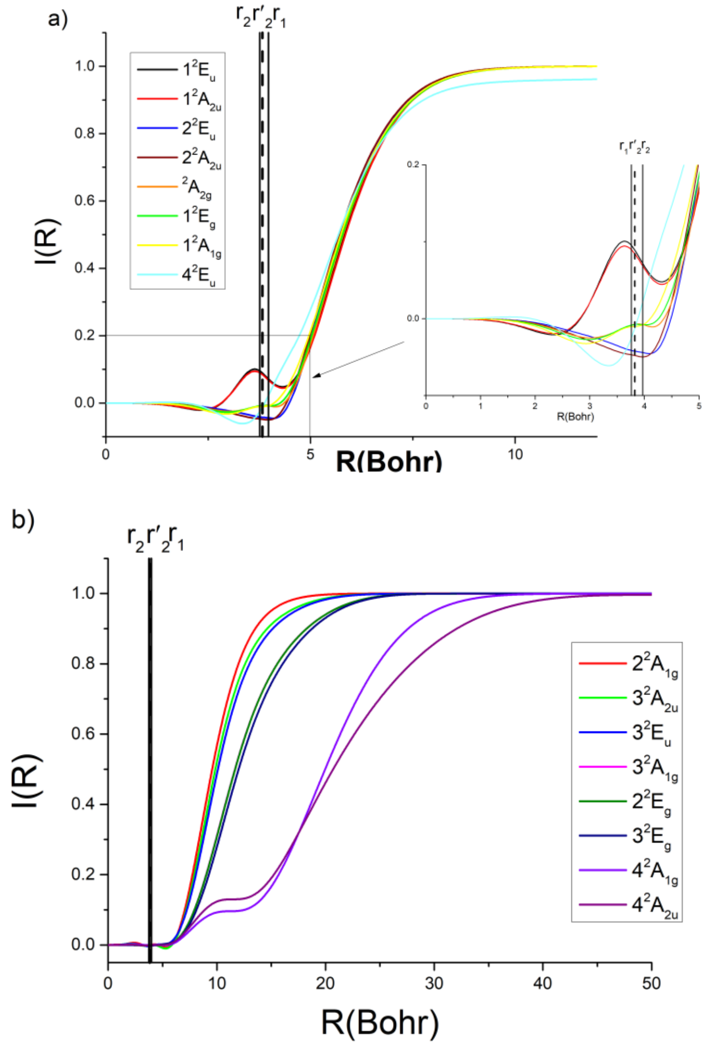

Figure 4.6. Integrated excess electron density for (a) valence charge separated states of $Li^+@C_{20}^-$ and (b) superatomic charge separated states of $Li^+@C_{20}^-$. r_1, r_2, and r_2' are the three characteristic radii from the center of the C_{20} cage.

The two $^2E_u/^2A_{2u}$ pairs, having counterparts in C_{20}^-, form the valence state group (i). The curves of the first pair exhibit a distinct maximum, similar to the parent fullerene. The maximum is at nearly the same distance in $Li^+@C_{20}^-$ (5.6 and 5.2 Bohr) as in the parent fullerene (5.7 and 5.4 Bohr). Moreover, the two pairs exhibit different behavior also in C_{20}^-. The density of the first $^2E_u/^2A_{2u}$ pair has both positive and negative density value inside the cage, while the densities of the second $^2E_u/^2A_{2u}$ pair change only little inside the cage, being slightly negative there. This difference indicates p-type and sp-type character for the first and second pair, respectively.

As shown in Fig. 4.5(a), most valence states of group (ii) have a peak of positive density contributions inside the cage, similar to the first $^2E_u/^2A_{2u}$ pair. The behavior of the I(R) curves helps us to better understand the character of the valence states in group (ii). One can see from Fig. 4.6(a) that the I(R) curves are consistent with the radial density curves of the valence states in group (ii), resulting in negative I(R) contribution inside the cage. Additionally, the valence states in group (ii) only exhibit maxima in the density distribution of the extra electron away from center. It indicates that the valence states of group (ii) are of sp-type inside the cage.

The weakest bound CS state, 4^2E_u, in Fig. 4.2 is of particular interest, as its RD distribution exhibits two peaks outside the cage, the first peak (at the radius $r = r_1$) and the second peak (~5.5 Bohr). One may wonder which one contributes more to the electron density? Based on the integrated density curve in Fig. 6(a), most of the excess electron is distributed outside the cage, while the total contribution inside the cage is negative.

4.6.2 Radial distributions of superatomic separated states

Compared to the parent fullerene, the excess electron density of the SA states of $Li^+@C_{20}^-$ is much closer to the center, as shown in Fig. 4.5(b). The $\Delta\rho(r)$ curves are more compact as compared to the broad distribution of the SA state in the parent fullerene. One may distinguish three different groups of SA states: (1) 2^2A_{1g}, 3^2A_{2u}, and 3^2E_u states, being s- and p-type SA states, (2) 3^2A_{1g}, 2^2E_g, and 3^2E_g, namely the d-type SA states, and (3) 4^2A_{1g} and 4^2A_{2u}, being second s- and p-type SA states. The SA states in the different groups have different slopes in the integrated electron density, as shown in Fig. 4.6(b).

As one can see from Fig. 4.5(b), the SA states of the different groups have maxima at different r values (~8.7 Bohr for group (1) and ~10.5 Bohr for group (2), respectively). Towards larger r the curves of group (1) and (2) decrease rapidly to zero between ~25 and ~30 Bohr, respectively. The RDs exhibit several minor density fluctuations inside the cage. However, the excess electrons density distributed inside the cage of the group (1) and group (2) SA states is negligible (smaller than 0.01), as shown in Fig. 4.6(a).

The SA states of group (3) possess excess electron density largely outside the cage. The $\Delta\rho(r)$ curves exhibit two maxima at ~7.6 Bohr and ~19.0 Bohr, respectively, separated by a node at ~11.3 Bohr. The nodes are reflected by short plateaus in the integrated density curves of Fig. 4.6(b). Moreover, the diffuse character of the SA states in group (3) is also seen in the smaller slopes compared to those of group (1) and (2).

4.7 Conclusions

In this chapter, we have performed a highly accurate investigation of $Li@C_{20}$ bound states, utilizing the state-of-the-art EA-EOM-CCSD method. Our results show that all obtained states are of $Li^+@C_{20}^-$ type. Due to the presence of the Li^+ guest cation, $Li^+@C_{20}^-$ possess more bound valence and superatomic states than C_{20}^- at the D_{3d} ground state equilibrium conformation. Among them, 8 charge separated valence states possess EBEs higher than 1.0 eV. Electron binding energies of the valence states of group (i) are higher than their counterparts in C_{20}^- (6.73 eV–5.03 eV vs. 2.05 eV–0.42 eV). Valence states of group (ii) have considerable binding energies and show p-character hybridization. Additionally, it can be inferred from the density distribution analysis of valence charge separated states, that, while the guest atom/cation has a larger influence on the EBEs than the SA states, there is little effect on the electron distributions.

By contrast, the Coulomb attraction of the Li^+ cation plays a more important role in the superatomic states. $Li^+@C_{20}^-$ possesses 8 superatomic states with EBEs >1.0 eV, which can be classified into three groups. Superatomic CS states of group (3) have nodes and are of a more diffuse nature than the other two groups. Compared to the only SA state in C_{20}^- with an EBE of ~ 0.3 meV, the corresponding SA state in $Li^+@C_{20}^-$ is stabilized by about 2.4 eV. Due to the diffuse feature, the EBEs of the superatomic states increase less than those of the valence states, which leads to a gap of 1.3-1.4 eV between the valence states and the onset of the SA states.

Chapter 5

Caged-electron States of Li@C_n: a Novel State of Large Endohedral Fullerene

5.1 Background and motivation

The first fullerene C_{60} was discovered in 1985 [1]. Since then, researchers have paid great attention to fullerenes, motivated by their impressive structures and unique electronic properties [91-93]. In the literature, there are numerous experimental and theoretical reports of both neutral [17, 165, 166] as well as ionic [112, 113, 114, 115, 167, 168] fullerenes. Endohedral fullerenes have been applied to a wide range of fields, according to the growing number of reports [135, 138, 139, 158]. Due to their electronic structures, they can exhibit properties, which their parent fullerenes cannot have, e.g., undergo an interatomic Coulombic decay [169]. Specially, one can easily find that the applications of fullerenes and their derivatives in the fields of organic solar cells [170-173], supercapacitors [174-176], catalyzers [177-179], and superconductive agents [180-182].

In this chapter, we concentrate on Li endohedral large fullerenes (much larger than Li@C_{20} studied in chapter 4), which can form interesting electronic states [135, 183, 184]. For example, Li@C_{60}, which was discovered in 1996 [185], has been seen as a compound with promising applications in solar cells [186]. Its electron transfer rate constant is considerably higher than in the parent fullerene C_{60} [187]. Moreover, it can play a role as an electron transfer controller [188] or a remarkable multistate molecular switch [189], due to its electronic properties.

Previously, the TC group at Heidelberg has studied endohedral fullerenes encapsulating noble gas guest atoms. As this study showed, these guest atoms have little effect on the valence states [118]. Unlike noble gas atoms, alkali guest atoms, like Li [190-192], act as an electron donor which donates the electron to the fullerene cage. Thus, the guest atom and the cage form CS states like in a neutral donor–acceptor system. The Li valence electron is transferred to the fullerene cage, and the system becomes a negatively charged fullerene cage encapsulating a positive charged cation. In previous studies, only such CS bound states of Li endohedral fullerenes were found, as mentioned in chapter 4.

In this chapter, the main goal is to report on hitherto unknown low-lying non-charge-separated states of large endohedral fullerene Li@C_n. One of the systems, i.e., Li@C_{60}, has been synthesized and studied in experiments [193, 194]. The accurate calculation of the states of Li@C_{60} requires an enormous effort. By employing accurate computational methods, we found an interesting non-charge-separated state, which may have promising applications. After analyzing the nature of the new state, which we named “caged-electron” state, we have an outlook on its applications in larger endohedral fullerenes where such a state can be the ground state.

This chapter is organized as follows. In section 5.2, we introduce the computational methods used. In section 5.3, we discuss the equilibrium geometry of the caged-electron states of Li@C_{60} and show that in the caged-electron states the Li atom is residing at the center. In section 5.4, we present EA-EOM-CCSD [43] results for the binding energies of several bound states of Li@C_{60}. In section 5.5, we compare the caged-electron states with other bound states of Li@C_{60} by analyzing the radial distributions. In section 5.6, a short outlook is given of the caged-electron state in Li@C_{180} and its possible applications. Finally, in section 5.7 a short conclusion is presented.

5.2 Computational details

We calculated the caged-electron state in Li@C_{60} both in I_h and C_{3v} conformation, by employing DFT/WB97XD [159] and HF methods, with cc-pVDZ [125] basis sets, utilizing the Gaussian program package [160]. To optimize the equilibrium geometry of the Li@C_{60} caged-electron states, the ΔSCF/DFT procedure is employed. In this procedure, one can use the “rotate” card of the Molpro program [129] to exchange the virtual orbital of the target excited state, with the highest occupied molecular orbital of the same irreducible representation, while keeping the occupation numbers frozen. For the ΔSCF/DFT calculations, we chose the M06-2X functional [195], which is suitable for non-covalent interactions, with density fitting approximations to speed up the calculations [196]. Importantly, in the equilibrium conformation of the caged-electron state, Li is essentially in the center of the cage (see below).

Upon geometry optimization, we performed state-of-the-art EA-EOM-CCSD computations for the bound states of $Li^+@C_{60}$ utilizing the CFOUR code [131]. We chose the $Li^+@C_{60}$ cation as the reference state, since it is a closed-shell system suitable for calculations. We used the same basis set as in chapter 4, referred to as DZ+. The EA-EOM-CCSD computations were based on the I_h symmetry conformation with an at the center of Li in the C_{60} cage (the structural parameters of the neutral C_{60} molecule were taken from an electron diffraction measurement [197]). Based on the EA-EOM-CCSD results, we also analyzed the radial density difference distributions of bound states of $Li@C_{60}$, using the method described in chapter 4.

We also discuss the caged-electron states in other large fullerenes, such as $Li@C_{180}$. We calculated the bound states at both the DFT/cc-pVDZ and HF/cc-pVDZ level, employing Koopmans' theorem. All calculations for $Li@C_{180}$ were done with the Gaussian program package.

5.3 Equilibrium geometry of the caged-electron state

5.3.1 Existence of the caged-electron state in $Li@C_{60}$

As shown in Fig. 5.1(a), there is a non-charge-separated state (referred to as the caged-electron state) of Li at center conformation, where the extra electron resides around the center. This state was bound at the HF/DFT level. We will further discuss this state in section 5.4 and 5.5.

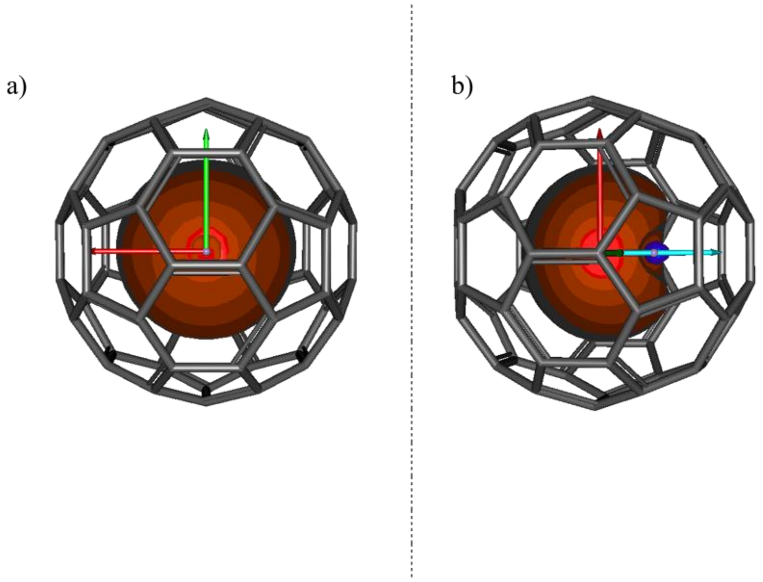

Figure 5.1. Images of the caged-electron state of Li@C_{60}. (a) Singly occupied natural orbital of neutral Li@C_{60} in I_h symmetry with lithium sitting at the center of the carbon cage computed with EA-EOM-CCSD. (b) Virtual HF orbital of the Li^+@C_{60} cation at its equilibrium geometry, i.e., in C_{3v} symmetry with lithium off-center computed at the HF level. The surfaces shown enclose 80% of the orbital density. The red, cyan, and green arrows assign the X, Y, and Z axes, respectively

The structure with Li at the center is not the equilibrium geometry of the Li^+@C_{60} ground state. According to the literature, in the Li^+@C_{60} ground state the Li^+ cation is off-center in a C_{3v} equilibrium conformation [103]. The interaction between Li^+ and the cage stabilizes the off-center position of Li^+, and the stabilization effect increases when there is an extra charge at the cage as in CS states. It is interesting to analyze whether there is a caged-electron state in an off-center endohedral fullerene Li@C_{60}. Due to the low symmetry, EA-EOM-CCSD computations were not viable for the off-center configuration. Instead, we employed HF and DFT with long-range corrected WB97XD function, using the Gaussian 09 program package. The caged-electron state is still strongly bound with a considerable EBE (2.27 eV in HF, 3.24 eV in DFT), at the equilibrium geometry of the Li^+@C_{60} cation ground state, applying Koopmans' theorem. The corresponding virtual orbital is depicted in Fig. 5.1(b). Although Li is off-center, it is interesting to note that the density of the excess electron resides at the center rather than surrounding the Li atom, resulting in a heart-like shape.

5.3.2 Geometry optimization of the caged-electron state of Li@C_{60}

While the caged-electron states are bound in both in the center and off-center conformations, one may wonder which structure would be energetically more favored for caged-electron state. Due to the fact that the extra electron charge stays at the center, the stabilization effect between Li^+ and thee cage is weaker than in the Li^+@C_{60} cation, and the at the center of structure may be favored. We employed the ΔSCF/DFT procedure, to optimize the geometry of the excited 1^2A_g state (the caged-electron state). As mentioned above, the ground state of Li^+@C_{60} is of C_{3v} symmetry with Li at a distance of 1.34 Å off the center. To compare, we also optimized the ground state conformation of Li^+@C_{60} and neutral Li@C_{60} at the DFT/cc-pVDZ level. The results of the geometry optimizations are shown in Table 5.1.

Table 5.1. Total (E_{tot}, a.u.) and relative (E_{rel}, eV) energies of the ground state (GS) and caged-electron state (CES) of neutral Li@C_{60} as well as the ground state of the Li^+@C_{60} cation (GS) at their corresponding optimized (equilibrium) configurations that differ by the position of Li, which is either "in the center" or "off-center" of the C_{60} cage. All the calculations are employing M06-2X functional and cc-pVDZ basis set. The distance of Li from the C_{60} center (R, Å) are listed in the third column.*

Initial structure	E_{tot}	E_{rel}	R
CES Li@C_{60} at center (I_h)	-2293.258776	0.006	0.00
CES Li@C_{60} off center (C_{2v})	-2293.258776	0.006	0.00
CES Li@C_{60} off center (C_{3v})	-2293.258982	0.000	0.10
GS Neutral Li@C_{60} (C_{3v})	-2293.278853		1.49
GS Li^+@C_{60} cation (C_{3v})	-2293.067496		1.47

* analytical gradient threshold for geometry optimization is $3.0*10^{-4}$ Hartree/Å.

As one can see in Table 5.1, the M06-2X functional is suitable for the system as its geometry optimization result of the Li^+@C_{60} ground state is consistent with experiment. For the caged-electron state of Li@C_{60}, the location of Li is very close (0.1 Å) to the center. The distance was much smaller than in the neutral ground state (1.49 Å), and cationic the ground state (1.47Å).

As the treatment of Li@C_{60} at the EA-EOM-CCSD level is not feasible without employing high symmetry, and Li is not far from the center in the equilibrium conformation, we assume I_h symmetry in the EA-EOM-CCSD calculations for the Li@C_{60} states.

5.4 Bound states of Li@C_{60} (I_h)

In Fig. 5.2, we show the binding energies of the electronic ground state and 7 low-lying excited states of neutral Li@C_{60} in the I_h symmetry conformation. As in chapter 4, the binding energies of the neutral Li@C_{60} states refer to the Li^+@C_{60} cation. The Li^+@C_{60} cation ground state is the reference state employed in the EA-EOM-CCSD computations. All states with an EBE larger than 1.0 eV are shown in Fig. 5.2.

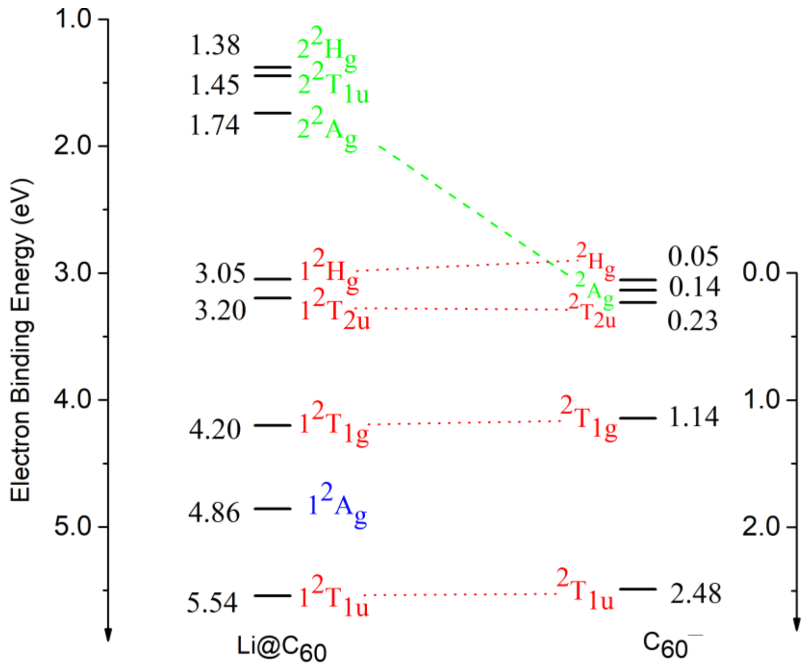

Figure 5.2. Electron binding energies of low-lying states of Li@C_{60} (in I_h symmetry) compared to all the bound states of the C_{60}^- anion computed at the EA-EOM-CCSD level of theory. The values for the C_{60}^- anion are taken from the literature (see refs [114] and [115]). All the bound states of Li@C_{60}, except of the 1^2A_g state, are charge separated states. The charge separated Li^+@C_{60}^- states as well as the bound states of the C_{60}^- anion can be divided into valence (shown in red) and superatomic (shown in green) states. The caged-electron state is the first excited state and is shown in blue.

Chapter 5

As discussed in chapter 4, all bound states of Li@C_{20} are of the charge separated Li^+@C_{20}^- form. There are two types of CS states, namely valence states in which the excess electron resides essentially on the carbon cage and superatomic states in which the excess electron charge is distributed well outside of the cage [19, 192, 198]. As shown in Fig. 5.2, Li@C_{60} possesses four low-lying valence CS states, and three superatomic CS states. Additionally, there is a new state which is neither of valence nor superatomic CS type. As C_{20} and C_{60} also have bound valence and superatomic states [115, 155], a comparison of Li@C_{60} CS states with those of C_{60}^- anion ,as done in Fig. 5.2, is of interest.

As shown in Fig. 5.2, all bound states of the C_{60}^- anion can be related to the corresponding states in Li@C_{60}, as indicated by dotted (for valence) and dashed (for superatomic) lines. While the Li^+ guest cation enhances the EBE of the states, it does not change the character or the order of the anionic states. As expected, the presence of the Li^+ cation stabilizes the bound states leading to higher binding energies. Compared to the valence states of C_{60}^-, the EBEs of the Li^+@C_{60}^- valence CS states are larger by about 3 eV. This can be crudely explained by estimating the electrostatic attraction between the Li^+ cation at the center and the negatively charged C_{60}^- cage (around 4 eV). With respect to the only bound superatomic state in C_{60}^-, the corresponding CS state of Li@C_{60}, 2^2Ag, is stabilized by 1.6 eV, being the most stable superatomic CS state of Li@C_{60}. This leads to an energy gap of around 1.3 eV between the highest valence and lowest superatomic CS states of Li@C_{60}. As discussed in chapter 4, the more compact valence states are more strongly influenced by the Li^+ cation than the diffuse superatomic states. Moreover, due to the presence of Li^+, there are further bound superatomic states. The valence and superatomic states different hybridizing orbitals patterns. The valence and superatomic states hybridize from the 2s and 2p orbitals of the fullerene carbon atoms, and 3s and higher unoccupied orbitals, respectively [199]. The superatomic orbitals distribute considerable electron density inside the cage, which is different from Rydberg states. The unique nature of superatomic orbitals is due to the hybridize of orbitals of fullerenes [200].

The spectrum of Li@C_{60}, shown in Fig. 5.2, exhibits a new state which is different from the valence and superatomic CS states. It is the first excited state of Li@C_{60}, 1^2Ag, possessing a considerably large EBE (4.86 eV). The singly occupied natural orbital associated with the new state based on the result of EA-EOM-CCSD calculations is shown in Fig. 5.3 (a). It is similar to the one shown in Fig. 5.1 (a). Clearly, the singly occupied natural orbital of the new state sits at the center of the cage and describes a caged excess electron. It should be noted that, to the best of our knowledge, this kind of state has not previously been reported for alkali endohedral fullerenes.

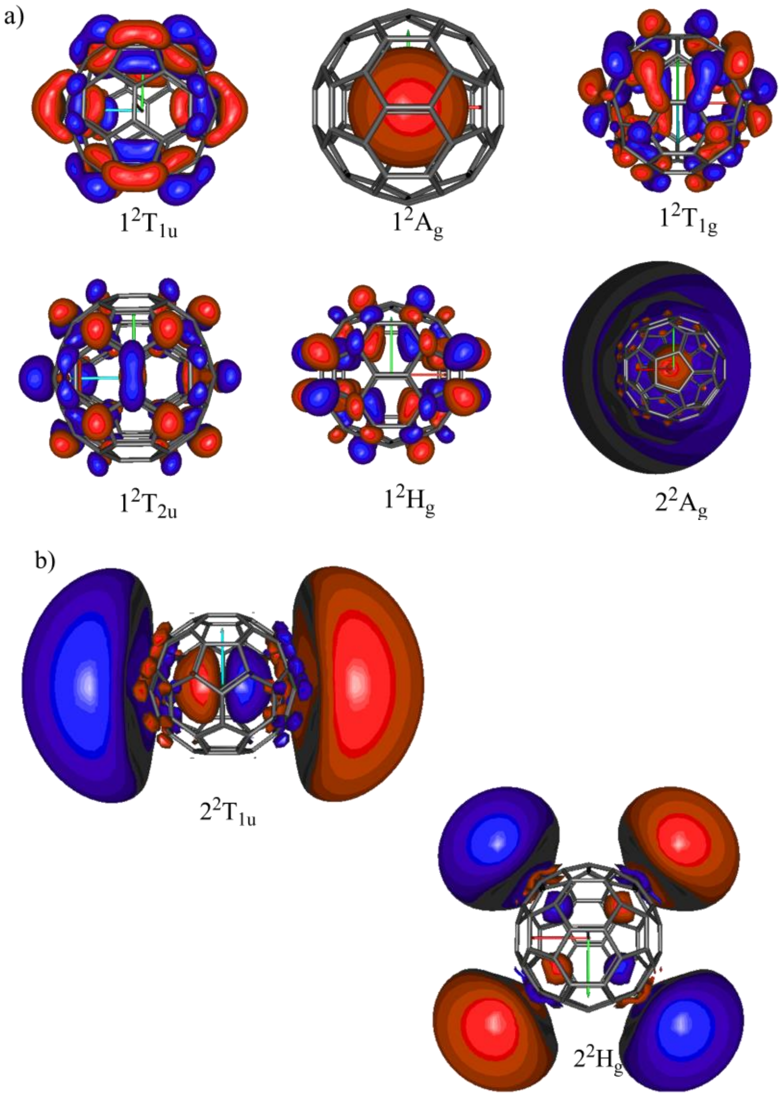

Figure 5.3. Singly-occupied natural orbitals of the Li@C_{60} states shown Figure 5.2 as obtained at the EA-EOM-CCSD level. a) Four valence charge separated states, one caged-electron state and an s-type superatomic charge separated state. b) The degenerate p- and d-type superatomic charge separated states. Of the degenerate states one component is shown. The surface encloses 50% of the orbital density. The red, cyan and green arrows depict X, Y and Z axes, respectively.

In Figure 5.3, we visualize the singly occupied natural orbitals of the 8 states. One can easily see that 1^2T_{1u}, 1^2T_{1g}, 1^2T_{2u} and 1^2H_g are valence charge separated (CS) states, with the electron density of their SONOs residing on the cage. Also we can easily distinguish the superatomic CS states, 2^2A_g, 2^2T_{1u} and 2^2H_g, featuring their characteristic diffuse charge distribution.

5.5 Radial distributions of Li@C$_{60}$ (I_h) bound states

To further analyze the states of Li@C$_{60}$, based on EA-EOM-CCSD results, we consider and characterize the excess electron density distribution of all the bound states in Fig. 5.2 by employing the "Δρ analysis" introduced in chapter 4. Positive and negative values of Δρ analysis indicate increase ("attached") and decrease, respectively, of the electron density comparing to the initial cation state. The radial distributions are presented in Fig. 5.4.

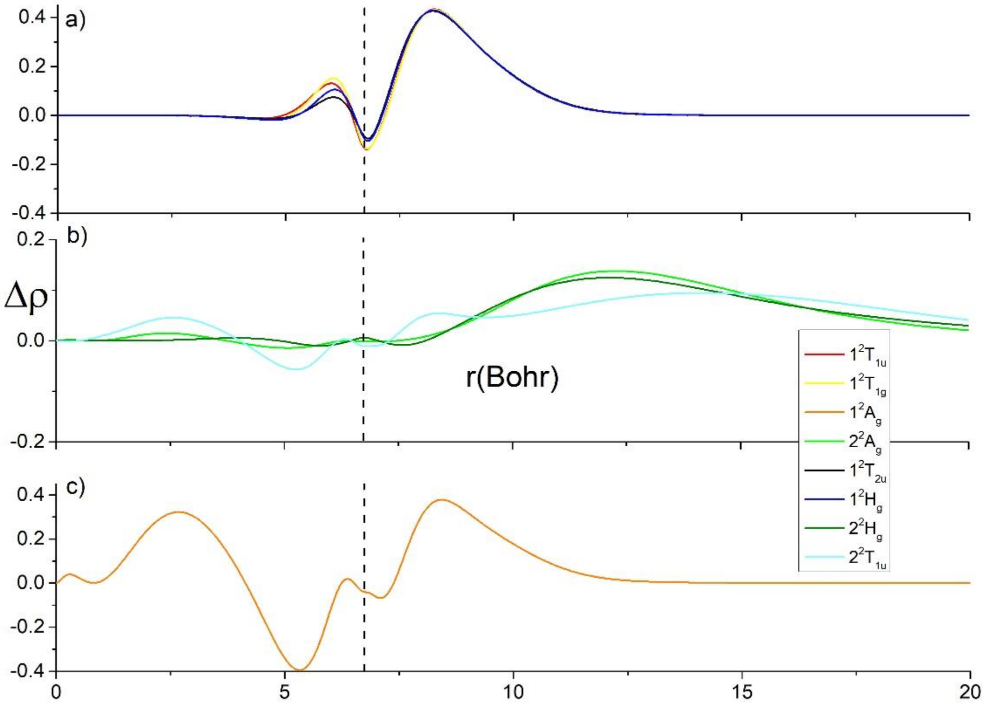

Figure 5.4. Radial distributions of the excess electron density for all states of Li@C$_{60}$ shown in Figure 5.2. The excess electron is defined with respect to Li$^+$@C$_{60}$ (see text). (a) Valence CS states. (b) Superatomic CS states. (c) Caged-electron state. The vertical dashed line indicates the radius of the carbon cage.

The upper panel of Figure 5.4, displays the Δρ curves of the valence CS states, which exhibit a similar behavior. One can expect that the excess electron density of valence states is distributed essentially around the cage, as valence states can be seen as hybrids formed from the 2s and 2p atomic and molecular orbitals of the fullerene carbon atoms [199]. As shown in Fig. 5.4 (a), the excess electron density is distributed partly outside the cage at around 8 Bohr and to a lesser extent inside the cage (around 6 Bohr). In the middle panel of Fig. 5.4, the low-lying superatomic CS states are addressed, which exhibit a distinctly different trend, comparing to the valence CS states. Only little excess electron density of superatomic CS states is distributed inside the cage, featuring a weak oscillatory behavior, whereas most of the density is diffusely distributed outside the cage over a range of up to 25 Bohr and more.

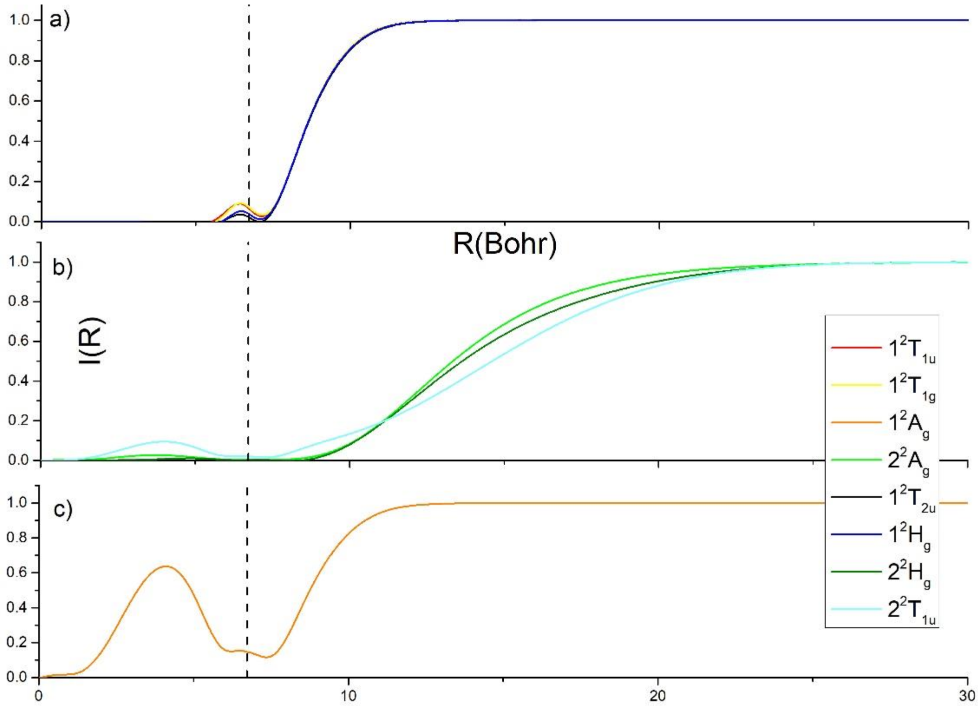

Figure 5.5. Integrated excess electron density for all states of Li@C$_{60}$ shown in Figure 5.2. The excess electron is defined with respect to Li$^+$@C$_{60}$ (see text). (a) Valence CS states. (b) Superatomic CS states. (c) Caged-electron state. The vertical dashed line indicates the radius of the carbon cage.

In the lower panel of Fig. 5.4, the radial excess electron distribution of the caged-electron state is shown. In contrast to the CS states, there is a considerable density variation on both sides of the cage. The most remarkable feature is the broad peak centered at around 2.5 Bohr, with a height of

0.3. The integrated difference density of peak amounts to almost 0.6 at about 4 Bohr, as shown in Fig. 5.5(c), indicating that, as in the Li ground state, the extra electron occupies an essentially spherical s-type orbital of the Li^+ cation.

At about 4 Bohr, the difference density becomes negative forming a wide valley centered at 5.3 Bohr, and thereafter rises apart from a minor wiggle, steadily to another maximum at 8.7 Bohr outside the cage. The integrated density difference decreases to 0.2 at the edge of the cage, then rises again, and finally converges to 1 at around 15 Bohr.

It is particularly interesting to compare the distribution of the excess electron in Fig. 5.4(c) and the SONO of the caged-electron state of $Li@C_{60}$ in Fig. 5.1(a). The SONO features the spherical density distribution around the Li^+ cation in the panel corresponding to the first peak in the difference density curve. However, there is no signature of the reorganization of the $Li^+@C_{60}$ density distribution in Fig. 5.1(a), due to the screening of the Li^+ cation, as such a response effect cannot be described within the SONO picture.

The minimum-maximum double feature in the caged-electron state radial density can be rationalized as the response of the charge distribution in the $Li^+@C_{60}$ cation to the screening of the Li^+ cation in the caged-electron state: Here, the attraction potential of the positive charge in the center of the cage is no longer present, and, as a result, there is a transfer of charge from the inside part near the cage towards the outside. This reorganization of the $Li^+@C_{60}$ charge distribution is clearly displayed in the density difference curve of the 1^2A_g state. In the CS states, by contrast, the extra electron does not change the original density distribution of the $Li^+@C_{60}$ cation in a major way.

To better understand the nature of the caged-electron state, we also investigated the radial distributions of the SONOs, as shown in Fig. 5.6. The SONOs of valence CS states, displayed in the upper panel of Fig. 5.6, exhibit a similar behavior, the electron density residing essentially around the cage. The SONOs of the superatomic CS state, as shown in the middle panel of Fig. 5.6, feature the typical broad density distributions with maxima for outside the cage. The SONO density distributions of both the valence and superatomic CS states closely resemble the respective Δρ curves of Fig. 5.4. This confirms the finding that in the CS states the extra electron does not cause a noticeable change of the $Li^+@C_{60}$ charge distribution.

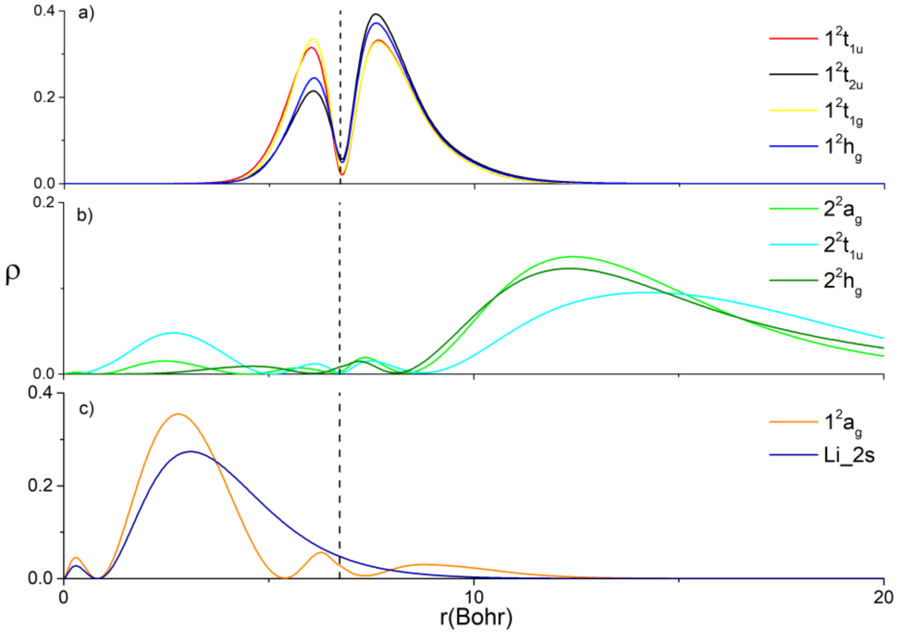

Figure 5.6. Radial density distributions of the singly-occupied natural orbital of various $Li@C_{60}$ states. (a) Valence CS states. (b) Superatomic CS states. (c) Caged-electron state 1^2A_g shown together with that of the 2s orbital of a free lithium atom. The vertical dashed line indicates the radius of the carbon cage.

By contrast, the radial distribution of the SONO associated with the 1^2A_g caged-electron state, shown in the lower panel of Fig. 5.6, differs markedly from the corresponding Δρ curve. While the spherical charge distribution surrounding the Li^+ cation at the center is seen within both the SONO and the Δρ curve, the SONO curve does not show the pronounced minimum-maximum feature in the Δρ curve, associated with the charge reorganization in the caged-electron state. As already mentioned, the charge reorganization effect cannot be captured at the one-particle level. The radial density distribution of the caged-electron state SONO is rather similar to that of the Li 2s orbital, as shown in lower panel of Fig. 5.6.

5.6 Caged-electron state in Li@C_{180}(I_h)

The 1^2A_g caged-electron state of Li@C_{60} corresponds to an arrangement in which a neutral Li atom (in its ground state) resides at the center of the C_{60} cage. One may ask why such a state is not the ground state but rather the first excited state, positioned 0.7 eV above the Li@C_{60} ground state, and, by extension, why in Li@C_{20} such a state does not exist at all.

The energy of the first excited state of the Li atom is 5.4 eV [201]. That is, it takes at least 5.4 eV to remove the 2s electron from the Li^+ core and promote it to an outer orbital, forming a CS state. Within a small fullerene cage, of course, such an “inner-excitement” is highly rewarded: the positive Li^+ at the center polarizes the fullerene electron cloud, which results in a substantial energy gain, compensating or even over-compensating the Li 2s excitation energy.

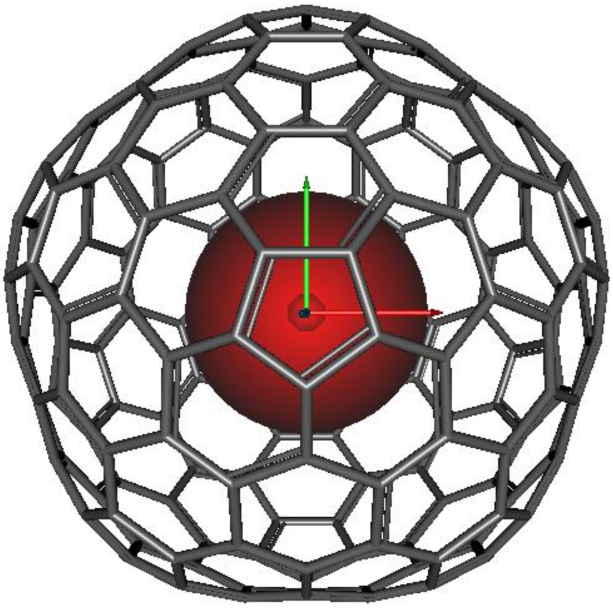

Figure 5.7. Image of the ground state of Li@C_{180}. Shown is the singly occupied natural orbital of neutral Li@C_{180} at its equilibrium geometry computed at the HF level. Clearly, the ground state is a caged-electron state. Notice that DFT calculations give the same result (see text). The surface shown encloses 80% of the orbital density. The red, cyan, and green arrows assign the X, Y, and Z axes, respectively.

Obviously, the polarization energy depends on the radius of the fullerene cage. In the limit of an infinity cage radius, the polarization energy would drop to zero, and the "neutral Li" (caged-electron) state would definitely be the ground state.

This suggests to inspect endohedral Li in still larger fullerenes and to see if in fact the neutral Li state becomes the ground state of the system. A suitable subject for such a study is Li@C_{180}, a highly symmetric (I_h) fullerene [202, 203], which will be discussed in the following. We have optimized the I_h equilibrium geometry of Li@C_{180} at both HF and WB97XD level and computed the vibrational frequencies. All frequencies obtained are positive, indicating the stability of the high symmetry conformation of Li@C_{180}.

Based on the HF and DFT calculations, one finds that the ground state of Li@C_{180} is indeed a caged-electron state, possessing large corresponding EBE (5.50 eV in HF and 5.31 eV in DFT, applying Koopmans' theorem). The large radius of the C_{180} cage (11.84 Bohr in HF, 11.89 Bohr in DFT), stabilizes the caged-electron state. It reduces the electrostatic attraction between a hypothetical Li^+ and a negatively charged cage to nearly a half of the value in Li@C_{60}, disfavoring a CS state. In Fig. 5.7, we present the HF SONO of Li@C_{180} ground state. Clearly, there is a striking similarity between the SONOS of the ground state of Li@C_{180} and the caged-electron state in Li@C_{60}.

5.7 Conclusions

In this chapter, we have analyzed the low-lying states of neutral Li@C_{60} (I_h) based on the results of EA-EOM-CCSD computations. The first excited state is a non-charge-separated state, being the first reported for endohedral alkali fullerenes. The other low-lying states feature the usual charge separated characteristics. As our analysis has shown, the caged-electron state is formed by adding an electron essentially to the Li 2s orbital of Li^+@C_{60}. The extra electron in the caged-electron state leads to a substantial rearrangement of the electron density distribution in the parent cation, which is in striking contrast to the charge separated states. According to our geometry optimization, the Li atom sits in the center of the cage at the equilibrium geometry of the caged-electron state, in contrast to the off-center charge separated states.

Our HF and DFT calculation of Li@C_{180} have confirmed that a caged-electron state can be the ground state of the larger highly symmetrical endohedral fullerene. Finally, we would like to have a short discussion of the applications of the caged-electron state. In the fields, such as artificial photosynthesis and solar cells, one is interested in charge separated states (see refs [193] and [204] and refs [205] and [206] and references therein). For example light-induced electron transfer has been applied to transfer an electron from anionic phthalocyanines to Li^+@C_{60} forming a long-lived charge separated neutral Li@C_{60} [206]. In such a context, the possibility of having a caged-electron state as the ground state, e.g., caged-electron state in Li@C_{180}, has promising applications. As an obvious option, one could use laser excitation to trigger and control the generation of desired charge separated states, customized for promising applications.

Chapter 5

Chapter 6

Bound states and symmetry breaking of the ring C_{20}^{-} anion: isomer of smallest fullerene

6.1 Background and motivation

Carbon rings C_m are important isomers of fullerenes and are abundant (m>10) in ion chromatography experiments [207]. Carbon rings have attracted much attention in the literature, due to their connection to the formation process of fullerenes and nanotubes [208-212]. One of the interesting properties of carbon rings is their different structures. In the literature [213, 214], there are four different types of structures of C_m rings (m is even number), i.e., (i) rings with equal bond lengths and bond angles (D_{mh} symmetry), (ii) rings with alternating bond angles and equal bond lengths ($D_{m/2h}$ symmetry), (iii) rings with alternating bond lengths and equal bond angles ($D_{m/2h}$ symmetry), and (iv) rings with alternating bond angles and bond lengths ($C_{m/2h}$ symmetry). Due to the difficulty to synthesize carbon rings and to determine their structures experimentally, the theoretical approach plays an important role in determining structures of carbon rings.

Nowadays, determining the energetically favorable structure of carbon rings is still an ongoing challenge for the application of density function theory (DFT). Most DFT calculations [39, 214, 215] wrongly predict the cumulenic form (with only equal double bonds) as the most stable structure for carbon rings. This prediction is not supported by experimental results, and the polyynic form (with alternating single and triple bonds) is more stable than the cumulenic form [38]. Clearly, DFT is not a reliable tool for determining the structures of carbon rings.

Unlike DFT, post-HF methods, such as CCSD [57], can provide the correct prediction: the polyynic form [213]. As an example, there is a lively discussion of the geometric and electronic structures of neutral C_{20} ring, employing DFT [37, 216-221]. Some previous theoretical studies predict that symmetry breaking occurs in the potential energy surface of neutral C_{20} carbon ring, due to the Jahn-Teller effect [37, 216, 217]. Bartlett and his co-workers reported the polyynic form in D_{10h} symmetry to be the energetical favorable geometry of the C_{20} carbon ring, based on their coupled cluster calculation results [124]. It indicates that there is no symmetry breaking of the neutral C_{20} carbon ring. Clearly, it is necessary to employ proper post-HF methods, e.g., the coupled cluster method, to study carbon rings.

Now we turn to the C_{20}^- ring anion, which is an isomer of the smallest fullerene anion C_{20}^-. As the C_{20}^- fullerene isomer possesses a considerable electron binding energy (EBE), naturally, researchers wonder whether the C_{20}^- carbon ring also possesses a large EBE. That this is indeed the case, has been proven by a photoelectron experiment on the C_{20}^- ring anion [119]. However, the geometrical structure and electronic bound states of the C_{20}^- ring anion are still unknown. Apart from a few DFT studies [121, 218, 219, 221], to the best of our knowledge, there is no theoretical study of C_{20}^- ring anion, employing proper post-HF methods. This motivates us to study the geometrical structure and all the electronic bound states of the C_{20}^- ring anion, utilizing state-of-the-art methods.

Studying all the electronic bound states of the C_{20}^- ring anion is interesting by itself. Unlike other anions with similar electron affinities, pure carbon clusters, like fullerene anions, have abundant excited bound states [112-115, 155]. This phenomenon raises the question whether the C_{20}^- ring anion can also exhibit a manifold of excited bound states. Additionally, studying excited states of prominent electron acceptors has great potential in application, as these states can facilitate electron transfer [114].

As the C_{20}^- ring is an open-shell anion, another question arises, namely, whether symmetry breaking occurs, due to the half-filled highest occupied molecular orbital. It is well known that the low-lying bound states play an important role in the mechanisms of symmetry breaking, i.e., vibronic coupling [49, 222, 223]. There are strong nonadiabatic interactions in particular between bound states with a small energy separation (~0.2 eV). In such cases the Born-Oppenheimer approximation may fail.

Thus, studying the bound states of the C_{20}^{-} ring is necessary. Moreover, as mentioned above, one needs proper methods, such as coupled cluster theory, to study the symmetry breaking problem of the C_{20}^{-} ring. To the best of our knowledge, our work is the first theoretical report applying accurate the EA-EOM-CCSD method [43] on the C_{20}^{-} ring to study its electronic bound states and symmetry breaking.

The chapter is organized as follows. In section 6.2, we briefly discuss the computational details of our calculations. In section 6.3, we present the ground state structure of the neutral C_{20} and anionic C_{20}^{-} ring. In section 6.4, we discuss the bound states of the C_{20}^{-} ring anion. In section 6.5, we analysis the possible mechanisms of symmetry breaking of the C_{20}^{-} ring. At last, in section 6.6, we summarize the results and conclude.

6.2 Computational details

We have carried out geometry optimizations for the neutral C_{20} ring in its ground state in D_{10h} symmetry. We performed the calculations with full Dunning triple-ζ basis sets (cc-pVTZ) [125], combing with CCSD theory employing CFOUR program package [131]. For the C_{20}^{-} anion, we employed EA-EOM-CCSD theory combined with cc-pVTZ basis sets, in D_{10h} as well as in C_{10h} symmetry. To demonstrate that the structures obtained are stable entities, we also calculated the vibrational frequencies of the C_{20} and C_{20}^{-} rings at CCSD/cc-pVTZ level and EA-EOM-CCSD/cc-pVTZ level of theory, respectively. Their frequencies are also of interest by themselves. Moreover, we also present several potential energy surface scans corresponding to different vibrational modes near the different equilibrium geometries of C_{20} and C_{20}^{-}, as discussed in section 6.5.

Based on the geometry of neutral C_{20} obtained by CCSD, we search for bound states of C_{20}^{-} employing the EA-EOM-CCSD method, with basis sets of different quality, in particular, the full dunning triple-ζ basis sets and TZ(-1d-1f)+10spd, which was utilized in chapter 3. TZ(-1d-1f) was constructed from triple-ζ Roos basis sets reducing d and f function. To find if there are any bound superatomic states, we further augmented TZ(-1d-1f) with 10 s-, 10 p-, and 10 d-type diffuse functions (denoted as 10spd) placed in the center of the C_{20} ring, which were generated using an even-tempered series $a_{n+1} = a_n/3.5$, starting with $a_0 = 1.0$.

6.3 Ground state geometry of C_{20} and C_{20}^-

Planar carbon rings C_m with an even number m, can be classified as m=4n+2 and m=4n families, where n is a natural number. The former family is predicted to possess aromaticity, as rings in this form satisfy Hückel's rule, a matter which attracted great attention. The latter family lacks aromaticity. Thus the geometry of the C_{20}, as a member of the latter family, should be polyynic rather than cumulenic. This guess is consistent with the coupled cluster results of the Bartlett group [124] and also with our present calculations.

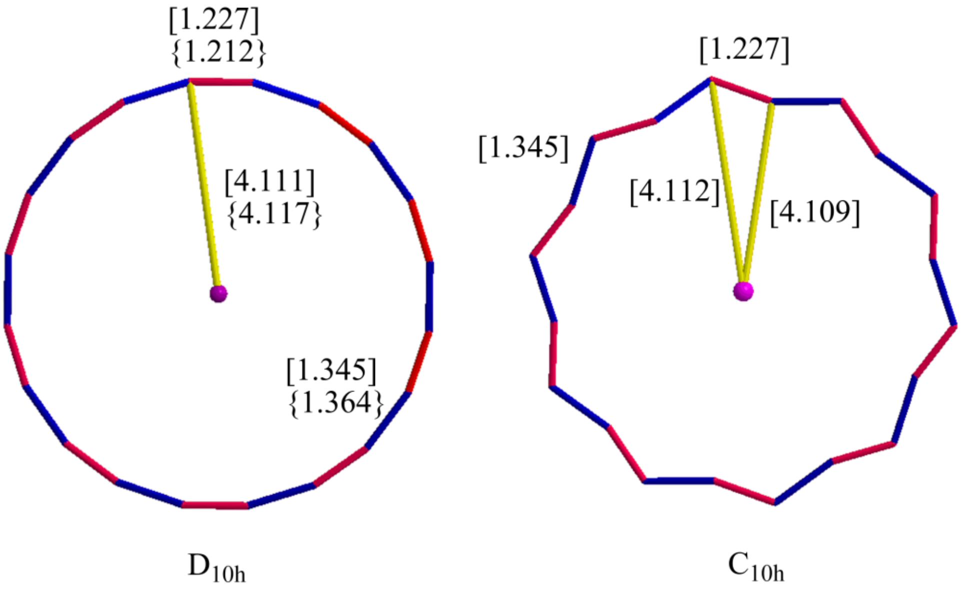

Figure 6.1. The equilibrium geometry of the ground state of neutral C_{20} (D_{10h}), which is obtained at CCSD/cc-pVTZ level (shown in curly brackets), and the equilibrium geometry of anionic C_{20}^- (D_{10h} and C_{10h}) obtained at EA-EOM-CCSD/cc-pVTZ level (in brackets). The equivalent bonds are indicated by the same color. All units are in Å.

In Fig. 6.1, we present the geometry of the ground state of the neutral and anionic C_{20} rings. In the literature, to the best of our knowledge, there is no theoretical study on the ground state geometry of C_{20}^- anion, employing accurate post-HF methods. Although we see that m=4n ring is polyynic, we still have to figure out whether the ground state is of type (iii) or type (iv). In Fig. 6.1, we present the radii of the ring rather than the bond angles, and show that the structure is of type (iv). Moreover, we want to know whether these anions of type (iii) and type (iv) are stable entities. To answer this question, we also calculated the vibrational frequencies and present the results in Table 6.1.

Table 6.1. Vibrational frequencies of the C_{20} (D_{10h}) and C_{20}^- (D_{10h} and C_{10h}) rings. The frequencies are obtained at CCSD/cc-pVTZ level and EA-EOM-CCSD/cc-pVTZ level respectively. All units are in cm^{-1}.

C_{20} (D_{10h})		C_{20}^- (D_{10h})		C_{20}^- (C_{10h})	
E_{2g}	51.76	A_{2g}	209.08i	E_{2g}	53.02
E_{2g}	51.76	E_{2g}	52.92	E_{2g}	53.02
E_{2u}	64.13	E_{2g}	52.92	E_{2u}	66.49
E_{2u}	64.13	E_{2u}	66.41	E_{2u}	66.49
E_{3u}	139.74	E_{2u}	66.41	E_{3u}	142.82
E_{3u}	139.74	E_{3u}	139.20	E_{3u}	142.82
E_{3g}	152.31	E_{3u}	139.20	E_{3g}	156.78
E_{3g}	152.31	E_{3g}	156.74	E_{3g}	156.78
E_{4g}	243.54	E_{3g}	156.74	E_{4g}	247.32
E_{4g}	243.54	E_{4g}	245.32	E_{4g}	247.32
E_{4u}	262.68	E_{4g}	245.32	E_{4u}	266.42
E_{4u}	262.68	E_{4u}	266.33	E_{4u}	266.42
A_{2g}	314.13	E_{4u}	266.33	A_{g}	282.07
B_{2u}	348.94	B_{1u}	343.42	B_{u}	345.76
B_{1g}	368.36	B_{1g}	378.00	B_{g}	377.68
B_{1u}	373.34	B_{2g}	380.93	B_{g}	381.63
$A_{1g(1)}$	389.54	B_{2u}	384.58	B_{u}	386.56
B_{2g}	402.30	A_{1g}	396.84	A_{g}	396.96
E_{4g}	471.91	E_{4g}	478.98	E_{4g}	480.18
E_{4g}	471.91	E_{4g}	478.98	E_{4g}	480.18
E_{4u}	509.56	E_{4u}	487.18	E_{4u}	487.45
E_{4u}	509.56	E_{4u}	487.18	E_{4u}	487.45
E_{1u}	536.53	E_{1u}	497.50	E_{1u}	491.21
E_{1u}	536.53	E_{1u}	497.50	E_{1u}	491.21
E_{3u}	540.26	E_{3u}	547.35	E_{3u}	548.67
E_{3u}	540.26	E_{3u}	547.35	E_{3u}	548.67
E_{1u}	553.23	E_{1u}	549.51	E_{1u}	550.28
E_{1u}	553.23	E_{1u}	549.51	E_{1u}	550.28
E_{2g}	588.06	E_{2g}	578.56	E_{2g}	584.03

Table 6.1. (continued)

C_{20} (D_{10h})		C_{20}^{-} (D_{10h})		C_{20}^{-} (C_{10h})	
E_{2g}	588.06	E_{2g}	578.56	E_{2g}	584.03
E_{3g}	636.77	E_{3g}	600.22	E_{3g}	600.44
E_{3g}	636.77	E_{3g}	600.22	E_{3g}	600.44
E_{2u}	794.47	E_{2u}	748.47	E_{2u}	746.35
E_{2u}	794.47	E_{2u}	748.47	E_{2u}	746.35
E_{2g}	825.49	E_{2g}	843.41	E_{2g}	843.47
E_{2g}	825.49	E_{2g}	843.41	E_{2g}	843.47
E_{1g}	1012.71	E_{1g}	963.66	E_{1g}	952.10
E_{1g}	1012.71	E_{1g}	963.66	E_{1g}	952.10
E_{3u}	1112.72	A_{1u}	1106.95	A_{u}	1086.30
E_{3u}	1112.72	E_{3u}	1141.52	E_{3u}	1143.88
A_{1u}	1148.43	E_{3u}	1141.52	E_{3u}	1143.88
E_{4g}	1338.53	E_{4g}	1387.20	E_{4g}	1389.17
E_{4g}	1338.53	E_{4g}	1387.20	E_{4g}	1389.17
B_{2u}	1437.30	B_{1u}	1499.96	B_{u}	1502.69
B_{1u}	2143.84	E_{1u}	2024.85	E_{1u}	2024.66
E_{4g}	2205.10	E_{1u}	2024.85	E_{1u}	2024.66
E_{4g}	2205.10	B_{2u}	2060.89	B_{u}	2062.17
E_{3u}	2294.81	E_{4g}	2137.83	E_{4g}	2138.19
E_{3u}	2294.81	E_{4g}	2137.83	E_{4g}	2138.19
$A_{1g(2)}$	2315.45	A_{1g}	2219.11	A_{g}	2219.00
E_{1u}	2321.96	E_{3u}	2240.57	E_{3u}	2238.02
E_{1u}	2321.96	E_{3u}	2240.57	E_{3u}	2238.02
E_{2g}	2342.10	E_{2g}	2260.54	E_{2g}	2260.59
E_{2g}	2342.10	E_{2g}	2260.54	E_{2g}	2260.59

Based on our results of vibrational frequency calculations, one can easily find out that the neutral C_{20} (in D_{10h} symmetry) is a stable entity, which is consistent with the results of the Bartlett group [124]. Unlike the neutral C_{20}, the structure of C_{20}^{-} in D_{10h} symmetry is thermodynamically unstable, due to the existence of an imaginary vibrational frequency. The vibrational mode of the imaginary frequency of C_{20}^{-} (in D_{10h} symmetry) is A_{2g}, which leads to type (iv) geometry. In the equilibrium geometry of C_{20}^{-} (in C_{10h} symmetry), all vibrational frequencies are real, showing thermodynamic stability. Thus, a D_{10h} to C_{10h} symmetry breaking in C_{20}^{-} ring anion is indicated. We will discuss the underlying mechanism in section 6.5.

6.4 Bound states of C_{20}^{-} anion

We searched for the bound states of the C_{20}^{-} ring anion and concentrated thereby on the equilibrium geometry of the neutral C_{20} ring. We hereby employed the EA-EOM-CCSD method with different basis sets. To compare the results with those of the C_{20}^{-} fullerene anion, we employed the same basis TZ(-1d-1f)+10spd as was utilized in our previous paper [155]. All bound states of the C_{20}^{-} ring anion are presented in Fig. 6.2.

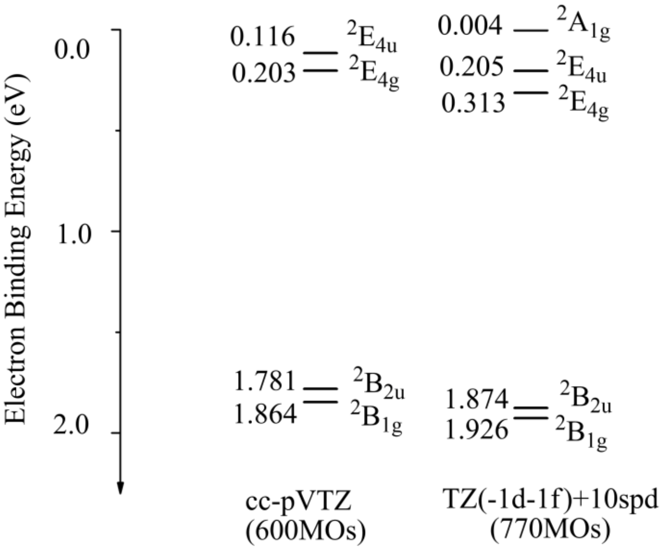

Figure 6.2. The binding energies (eV) of the bound states of the C_{20}^{-} ring anion calculated employing the EA-EOM-CCSD method and different basis sets. All states are valence bound states except the $^2A_{1g}$ state, which is a superatomic bound state.

As shown in Fig. 6.2, there are four bound valence states of the C_{20}^{-} ring anion at EA-EOM-CCSD/cc-pVTZ level, including two non-degenerate states, i.e., $^2B_{1g}$ and $^2B_{2u}$, and two degenerate states i.e., $^2E_{4u}$ and $^2E_{4g}$. Although the fullerene isomer also has two degenerate and two non-degenerate states, the spectrum of bound states of the C_{20}^{-} ring is different from its fullerene counterpart [155]. The bound states of C_{20}^{-} ring can be classified as two pairs: two low-lying non-degenerate states lower in energy and two degenerate states higher in energy. The non-degenerate states are close in energy with a small gap of less than 0.1 eV. Similarly, there is a ~0.1 eV gap between the degenerate states. Between the degenerate states and non-degenerate states there is a substantial gap of around 1.5 eV. It is noteworthy that the two low-lying non-degenerate bound states of the ring anion, are nearly degenerate in energy such that the photoelectron experiment failed and attributed them to one bound state [119].

As seen in Fig. 6.2, the use of the cc-pVTZ basis set is sufficient to describe the low-lying bound valence states of the C_{20}^{-}. Noteworthy, the larger basis (TZ(-1d-1f)+10spd) predicts the existence of an additional, very weakly bound $^2A_{1g}$ state. This state is a superatomic state showing that as found for the fullerene, the carbon ring can also form a superatomic state.

In the literature, the experimental electron binding energy of the C_{20}^{-} ring is higher than that of its fullerene isomer [119]. However the calculated EBE of the ground state of the anion (1.93 eV) is smaller than that of the ground state of its fullerene isomer (2.05 eV). This indicates that, to compare theoretical results with the experimental results more closely, one may need an even better method and/or basis set for this carbon ring.

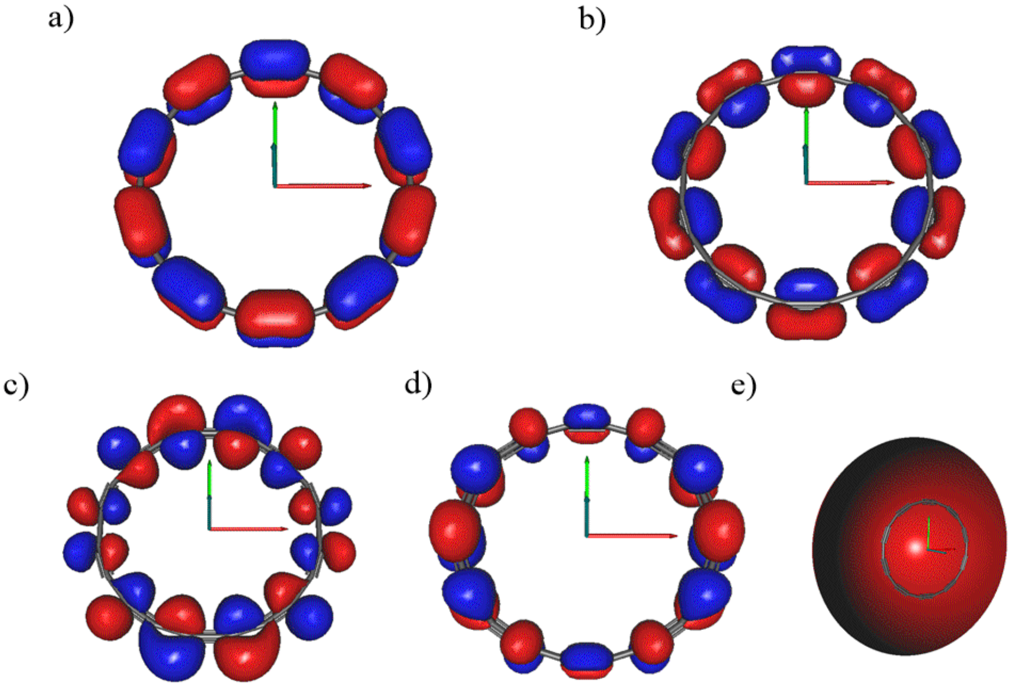

Figure 6.3. Singly occupied natural orbitals (SONOs) associated with (a)$^2B_{1g}$, (b) $^2B_{2u}$, (c) $^2E_{4g}$, (d) $^2E_{4u}$, and (e) $^2A_{1g}$ states. For the $^2E_{4g}$ and $^2E_{4u}$ states, the SONOs of only one component are shown. The red, cyan and green arrows are X, Y and Z axes, respectively. The surfaces enclose 80% of the orbital density.

The Singly occupied natural orbitals (SONOs) corresponding to all bound states of the C_{20}^{-} ring are shown in Fig 6.3. As one can see from the figure, the SONO of the non-degenerate valence state $^2B_{1g}$ is perpendicular to the plane, while the SONO of $^2B_{2u}$ is in plane. Since the ring is large and contains 20 carbon atoms, its curvature is small and the atomic p orbitals, contributing to the $^2B_{1g}$ and $^2B_{2u}$ states, do not have much overlap with other π orbitals. This is the reason why these two states are close in energy. As a result, these two states may play a role in a vibronic coupling scenario, which we will discuss in section 6.5. Similarly, the SONOs of the $^2E_{4g}$ and $^2E_{4u}$ states, shown in Fig. 6.3, are also perpendicular to each other. One can easily see that the extra electron in the low-lying states $^2B_{1g}$ and $^2B_{2u}$ are equally distributed at every atom. However, the extra electron distributions of higher excited states $^2E_{4g}$ and $^2E_{4u}$ are located on some particular atoms. The different nature of the distributions of the extra electron may be the reason for the large gap between the valence states.

As presented in Fig 6.3, the $^2A_{1g}$ state is an s-type superatomic bound state. Comparing to its counterpart in the C_{20}^{-} fullerene, it is slightly stronger in binding energy (4 meV comparing to 0.27 meV). The much larger radius of the ring (~4.1 Å) than that of the fullerene isomer (~2.0 Å), may be the reason for the stronger bound superatomic states. This is an example for the fact that forming superatomic bound state is a common property of carbon clusters with hollow space inside. We hope that this common property will motivate the search for superatomic states in carbon clusters, such as carbon rings.

6.5 Possible mechanism of symmetry breaking in C_{20}^{-} anion

In this section, we will have a discussion of possible mechanisms of symmetry breaking of the C_{20}^{-} anion, at the limitation of our method. As there is a ~1.5 eV gap between the non-degenerate and degenerate states, the low-lying states may play a more important role in the symmetry breaking mechanism. It is noteworthy that due to the small energy spilt between the two low-lying states, these two states are near a possible conical intersection. In this case, the adiabatic approximation, e.g., Born-Oppenheimer approximation, may fail and one may need the diabatic approximation to discuss the nuclear dynamics. We will concentrate on the low-lying states $^2B_{1g}$ and $^2B_{2u}$, and present a potential energy surface scan of these two states.

To determine the reason of symmetry breaking, we calculated the total energy of the ground and first excited states of the C_{20}^- anion at the EA-EOM-CCSD/cc-pVTZ level for different distorted geometries in the vicinity of the equilibrium geometry of neutral C_{20} and anionic C_{20}^- (in both D_{10h} and C_{10h} symmetries).

6.5.1 Determining dimensionless normal coordinates Q

The equilibrium geometry of C_{20}^- anion can be described as the equilibrium geometry of neutral C_{20} distorted by different symmetry adapted normal coordinates **Q**. As usual [49, 224, 225], the normal coordinates diagonalize the Hamiltonian describing the harmonic vibrations of an electronic state, here, the ground state of neutral C_{20}. Employing dimensionless normal coordinates **Q**, one has

$$\hat{H}(\boldsymbol{Q}) = V_0 + \frac{\hbar\omega_\alpha}{2}\left(\sum_{\boldsymbol{\alpha}} -\frac{\partial^2}{\partial \boldsymbol{Q}_{\boldsymbol{\alpha}}^2} + \boldsymbol{Q}_{\boldsymbol{\alpha}}^2\right) + \cdots,$$

where V_0 is the potential energy at the point $x=x_0$. ω_α is the frequency for vibrational mode α.

The transformation between Cartesian coordinates x and dimensionless normal coordinates is given by,

$$\boldsymbol{Q} = \widetilde{\boldsymbol{D}}(\boldsymbol{x} - \boldsymbol{x_0}) \quad ,$$

$$\boldsymbol{x} = \boldsymbol{x_0} + \widetilde{\boldsymbol{D}}'\boldsymbol{Q} \quad ,$$

where $\boldsymbol{x_0}$ stands for the minimum energy point of the potential energy surface. The transformation matrices, which are no longer orthonormal.

However, the program CFOUR, provides orthonormal vectors $\boldsymbol{D}$ and $\boldsymbol{D^T}$, which are not dimensionless. To determine dimensionless Q, one has convert the matrix $\boldsymbol{D}$ and $\boldsymbol{D^T}$ to $\widetilde{\boldsymbol{D}}$ and $\widetilde{\boldsymbol{D}}'$, respectively:

$$\widetilde{\boldsymbol{D}}_{\alpha i} = \boldsymbol{D}_{\alpha i}\sqrt{\frac{m_i \omega_\alpha}{\hbar}} \quad ,$$

$$\widetilde{\boldsymbol{D}}'_{i\alpha} = \boldsymbol{D}^{T}_{i\alpha}\sqrt{\frac{\hbar}{m_i \omega_\alpha}} \quad ,$$

where $\hbar$ is the reduced Planck constant and m_i is the corresponding reduced mass and the frequency ω_α corresponds to the equilibrium geometry of the ground state of the C_{20} ring.

6.5.2 Potential energy surface scans in Q space

We first discuss a cut through the potential energy surface of the anion along the A_{2g} vibrational mode starting at the equilibrium geometry of the neutral, i.e., in D_{10h} symmetry. The A_{2g} mode is the one with the imaginary frequency of the anion.

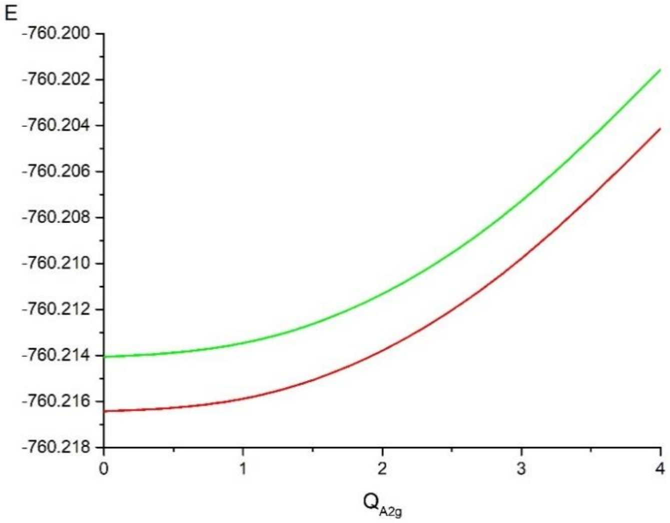

Figure 6.4. Cuts through the potential energy surfaces along the A_{2g} mode of the two lowest states of C_{20}^{-} ring anion. The red line is the ground state $^2B_{1g}$, and the green line is the first excited state $^2B_{2u}$. At $Q_{A_{2g}}$=0, the geometry is the equilibrium geometry of the neutral C_{20} ring (in D_{10h} symmetry) obtained at CCSD/cc-pVTZ level. Energies are in a.u.

As one can see from Fig. 6.4, there is no local minimum of this potential energy curve of the anion apart from the equilibrium geometry of the neutral C_{20} ring. Clearly, this finding cannot explain the existence of an imaginary frequency and hence the symmetry breaking corresponding to it. The vibrational calculations, shown in section 6.3, indicate that there should be at least one local minimum, corresponding to the C_{10h} symmetry. Consequently, this implies that it is not a single mode (A_{2g}) alone which is responsible for the symmetry breaking.

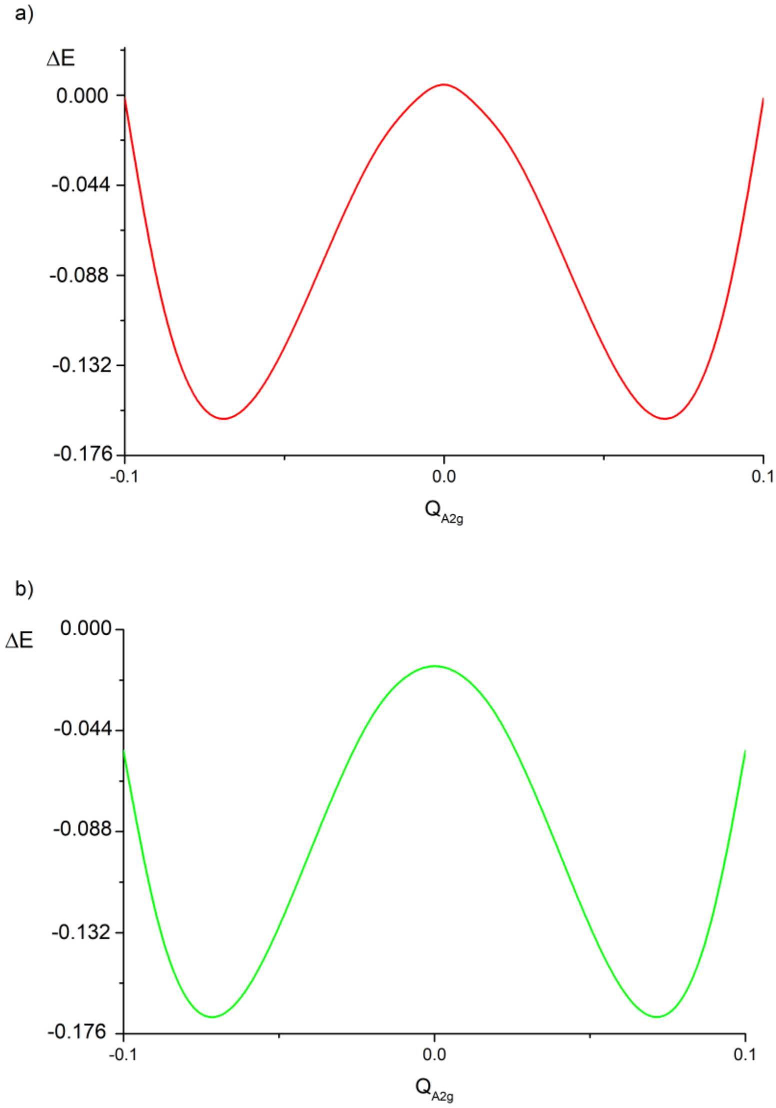

Figure 6.5. Cuts through potential energy surface along the A_{2g} mode for two states of the C_{20}^- ring anion, a) ground state $^2B_{1g}$, and b) first excited state $^2B_{2u}$. At $Q_{A_{2g}}$=0, the geometry is the equilibrium geometry of the C_{20}^- ring anion in D_{10h} symmetry, obtained at EA-EOM-CCSD/cc-pVTZ level. The plots show the presence of symmetry breaking. Energies (cm^{-1}) are relative to that at the D_{10h} minimum.

To better understand the potential energy surface, we calculated the values of the only two available totally symmetric vibrational modes $Q_{A_{1g(1)}}$ (frequency 389.54) and $Q_{A_{1g(2)}}$ (frequency 2315.45), corresponding to the transfer from C_{20} to C_{20}^{-} (both in D_{10h} symmetry). The results are $\boldsymbol{Q}_{A_{1g(1)}}$=0.546 and $\boldsymbol{Q}_{A_{1g(2)}}$=8.675. The value of the latter is rather unusually large. Based on this finding, we have computed another potential energy surface scan along $\boldsymbol{Q}_{A_{2g}}$, at the equilibrium geometry of C_{20}^{-} in D_{10h} symmetry. This cut is shown in Fig 6.5.

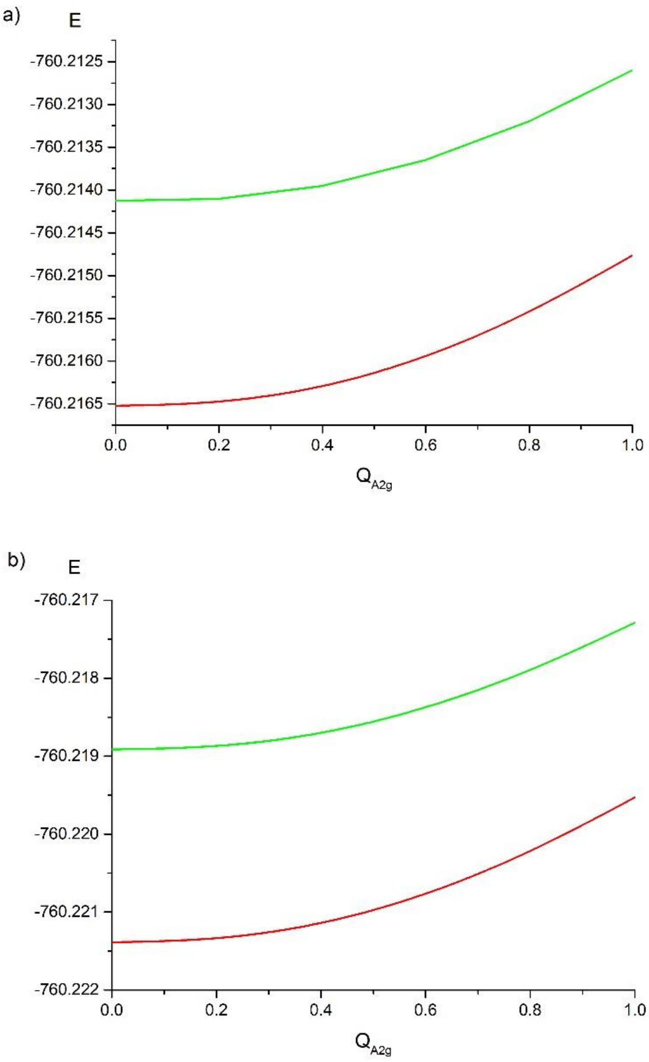

Figure 6.6. Cuts along A_{2g} of the potential energy surface of the two lowest lying states of the C_{20}^{-} ring anion. The red lines are the ground state $^{2}B_{1g}$, and the green lines are the first excited state $^{2}B_{2u}$. At $Q_{A_{2g}}$=0, the geometry is the equilibrium geometry of the neutral C_{20} ring in D_{10h} and obtained at CCSD/cc-pVTZ level with a distortion of only one totally symmetric mode: (a) $Q_{A_{1g(1)}}$=0.546, $Q_{A_{1g(2)}}$=0, and (b) $Q_{A_{1g(1)}}$=0, $Q_{A_{1g(2)}}$=8.675. Energies are in a.u.

The computed energy curves of the ground and first excited states near the equilibrium geometry of C_{20}^{-} in D_{10h} symmetry, show indeed that the inclusion of the vibrational modes $\boldsymbol{Q}_{A_{2g}}$ leads to a minimum in C_{10h} symmetry, i.e., to a symmetry breaking. This finding makes clear that care must be taken when discussing weak symmetry breaking where the energy is lowered only slightly, but the geometry (here the dimensionless $\mathbf{Q}$ for the totally symmetric modes) changes substantially. In such cases the interplay of the totally symmetric modes and the symmetry breaking mode (here A_{2g}) is relevant and must be taken into account.

We can now ask the question whether the interplay of A_{2g} with one of the two totally symmetric modes suffices to explain the symmetry breaking. The computational answer is depicted in Fig. 6.6. The curves shown are obtained by calculating the energy of the ground and first excited states of the C_{20}^{-} ring anion along A_{2g} taking into account the distortion of only one of the totally symmetric mode. As seen, the curves do not exhibit a local minimum and cannot explain symmetry breaking. Obviously, linear vibronic coupling is not the reason for the symmetry breaking.

In the case of C_{20}^{-} ring anion, there is no Jahn-Teller effect, to explain the symmetry breaking, because neither the involved states nor the coupling modes are degenerate. However, as the ground state $^2B_{1g}$ and the first excited state $^2B_{2u}$ are very close in energy (~0.08 eV), and vibronic coupling between them could be operative apart from the symmetry breaking distortion discussed above which is operative within the ground state itself. One may wonder whether vibronic coupling effects, do also play a role in the symmetry breaking of C_{20}^{-} ring anion?

Interestingly, due to the high symmetry of the system, there is no mode available which directly couples the ground and first excited states. i.e., a linear vibronic coupling model is not present. The lowest order vibronic coupling between these two states is a bilinear coupling [222]. Again, due to the high symmetry, there is only one pair of modes which can couple bilinearly the two states in question. These two possible modes of bilinear coupling are $\boldsymbol{Q}_{A_{2g}}$ and $\boldsymbol{Q}_{A_{1u}}$, since we have $\boldsymbol{A_{2g}} \otimes \boldsymbol{A_{1u}} = \boldsymbol{A_{2u}}$ and $\boldsymbol{B_{1g}} \otimes \boldsymbol{B_{2u}} = \boldsymbol{A_{2u}}$ in D_{10h} symmetry. We scanned the potential energy surface of the C_{20}^{-} ground state along the joint variation of $\boldsymbol{Q}_{A_{2g}}$ and $\boldsymbol{Q}_{A_{1u}}$, as shown in Fig. 6.7, where for simplicity, we set $\boldsymbol{Q}_{A_{2g}} = \boldsymbol{Q}_{A_{1u}} = \boldsymbol{Q}$ in the potential energy surface scan.

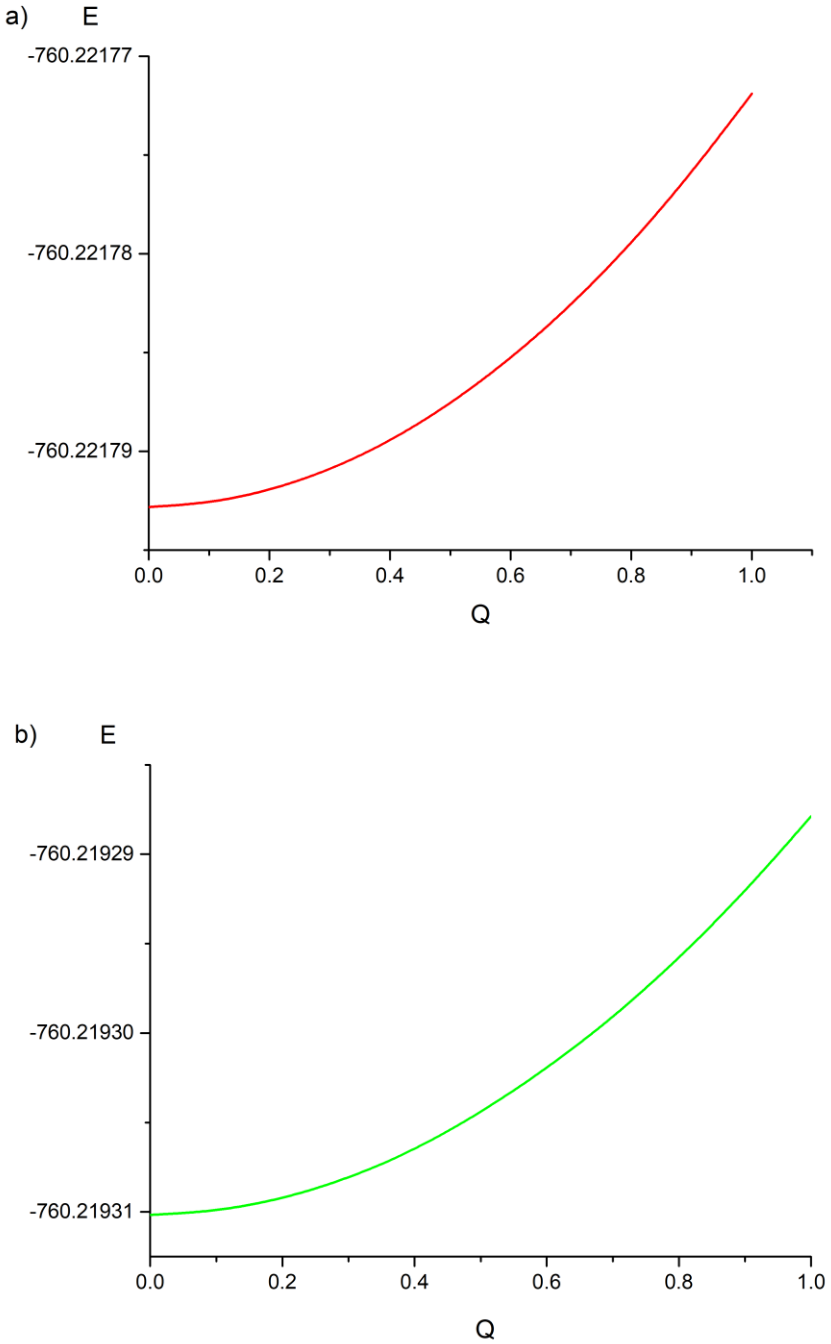

Figure 6.7. Test for bilinear coupling between the ground and first excited states of the anion. Shown is a cut through the potential energy surface of (a) the ground state of the C_{20}^{-} ring anion (b) the first excited state of this anion, along the bilinear distortion Q. Here, $\boldsymbol{Q_{A_{2g}} = Q_{A_{1u}} = Q}$ for simplicity. The point Q=0 is the equilibrium geometry of C_{20}^{-} ring anion in D_{10h} symmetry. Energies are in a.u.

As shown in Fig. 6.7, there is a non-vanishing bilinear coupling between the states along $\boldsymbol{Q_{A_{2g}}}$ and $\boldsymbol{Q_{A_{1u}}}$, but this coupling cannot lead to symmetry breaking. If there was a symmetry breaking via bilinear coupling, the planar symmetry of the ring would break too [224, 225], as A_{1u} is the out of plane mode. Thus, within the accuracy of the ab initio calculations, we can safely draw the conclusion that the symmetry breaking is not due to the bilinear vibronic coupling.

We conclude that to the symmetry breaking of the C_{20}^{-} ring from D_{10h} to C_{10h} is due to the interplay of the symmetry breaking mode A_{2g} and the totally symmetric modes. It is the result of geometry distortion of the ring upon electron attachment. The triple bond length increases by 0.015 Å while the length of single bond decreases by 0.019 Å. This is consistent with findings for small carbon systems [226]. Unlike the carbon ring, the total length of large linear carbon chains, e.g., C_{10}, increases, due to the attachment of an extra electron [227, 228]. The different trend of carbon rings and carbon chains upon an extra electron attachment results in a large ring strain. This leads to the following for the radii of the ring: 4.111 Å of the C_{20}^{-} ring in D_{10h} and 4.009/4.112 Å in C_{10h}, see Fig. 6.1. The smaller circumference of the ring in D_{10h} upon electron attachment leads to stronger ring strain between single and triple bonds, which the system partly reduces by symmetry breaking.

6.6 Conclusions

By employing the state-of-the-art EA-EOM-CCSD method and reliable basis sets, we have performed a thorough study of all the anionic bound states of the C_{20}^{-} ring. Similar to the fullerene isomer, we have found four valence and one superatomic bound states of the C_{20}^{-} ring anion, at the equilibrium geometry of the parent C_{20} neutral ground state. Among the bound states, the two of lowest energy $^2B_{1g}$ and $^2B_{2u}$, are non-degenerate states close by in energy and possess relatively high binding energies (1.93 eV and 1.87 eV, respectively). The other two are degenerate states $^2E_{4g}$ and $^2E_{4u}$, which are the weakly bound valence states (0.31 eV and 0.21 eV, respectively). Similar to the fullerene isomer, there is one superatomic state $^2A_{1g}$, with slightly stronger binding energy (4 meV) than its counterpart in the fullerene (0.27 meV). The stronger binding energy of the superatomic state of the ring, may owe its strength to the larger radius of the carbon ring than the radius of its fullerene isomer.

Moreover, based on the results of rather many scans of the potential energy surface and the computed vibrational frequencies, we notice a symmetry breaking in the C_{20}^{-} ring anion which does not exist in the neutral molecule. After analyzing the possible mechanisms of symmetry breaking, we conclude that the symmetry breaking is not due to vibronic coupling, but rather due to the interplay between the symmetry breaking mode and the totally symmetric ones. This interplay stems from the shrinking of the ring which of the ring upon electron attachment that produces ring stress which is reduced by asymmetric distortion.

Chapter 6

Chapter 7

Conclusions and Outlook

In this work we investigated electronic properties of typical carbon clusters, i.e., fullerenes, endohedral fullerenes, and carbon rings. We have employed state-of-the-art coupled cluster singles and doubles (CCSD) and equation of motion coupled cluster singles and doubles method for electron affinities (EA-EOM-CCSD) methods as well as proper basis sets to rather large molecular systems. The CCSD and EA-EOM-CCSD methods are accurate high level methods and the results obtained underline the necessary of applying such methods to carbon clusters studies.

We have analyzed the molecular structure and the electronic states of the smallest fullerene C_{20} and of its anion. Our geometry optimization shows that the energetically favored structures of C_{20} molecule and C_{20}^{-} anion are in D_{3d} and D_{2h} symmetry, respectively. Based on the geometry optimization results, we calculated the electronic affinity of the C_{20} fullerene, and the result is consistent with the experimental results (error within ~0.03 eV), which sheds light on the proper methods needed to study carbon clusters. We have also investigated the bound electronic ground and excited states of C_{20}^{-} anion. Our calculations reveal that the C_{20}^{-} anion possesses five bound states, including four valence states and one diffuse superatomic state. This finding indicates that the ability of forming superatom molecule orbitals can be found even in the smallest fullerene and thus is a common property of carbon clusters with hollow space inside. We hope that the finding of superatom molecule orbital in the smallest fullerene anion can inspire researchers to further identify and investigate superatomic states for carbon clusters.

We have then turned to fullerene derivatives, i.e., alkali endohedral fullerenes. Our EA-EOM-CCSD calculations on bound states of Li@C_{20} proves that all of the many low-lying electronic states of Li@C_{20} are charge separated states, resulting due to the high electron affinities of fullerenes and the low ionization potential of alkali atoms. As expected, owing to the presence of the guest atom, there are more valence and superatomic states in the endohedral fullerene Li@C_{20} than in the anion C_{20}^{-}. The comparison between charge separated valence states and their counterparts in the parent fullerene anion C_{20}^{-} is helpful. It reveals that the Coulomb effect of the Li^{+} cation only increases the binding energy of valence states without affecting the character of valence states. In the case of superatomic states, the Li^{+} cation compacts the diffuse superatom molecule orbitals, in sharp contrast to the weak perturbative effect of noble gas guest atoms. Our finding of the relation between the guest atom and valence/superatomic charge separated states can provide a new starting point for designing new endohedral fullerenes with special charge separated states. Moreover, it also provides another way to searching possible superatomic states of fullerene anions, by studying respective neutral endohedral fullerene derivatives.

It used to be a well-accepted idea that electronic bound states of alkali endohedral fullerenes are charge separated states. Our calculations on Li@C_{60} electronic states has proven that most of the states are charge separated states. The Li^{+} cation has a stabilizing effect on every bound valence state as in the smallest fullerene, resulting in an increase of electron binding energies. Moreover, similar to Li@C_{20}, the Li^{+} cation has a similar compact effect on the superatomic states. However, unlike Li@C_{20}, our EA-EOM-CCSD calculations on Li@C_{60} predict a hitherto unknown low-lying non-charge-separated state, which is referred to as caged-electron state. This intriguing electronic state freezing the electron at the center of the cage, independently from the position of the Li guest atom, is the result of decreasing the Coulomb effect inside the cage due to the increasing size of fullerenes. Thus this finding is a great example of the size effect of fullerenes. Moreover, our geometry optimization calculation suggests that at center structure is the equilibrium geometry of this caged-electron state. The geometry is different from that of the charge separated neutral Li@C_{60} or the cationic Li^{+}@C_{60} system. It indicates a possible way to change the position of guest atom of endohedral fullerenes. As the caged-electron state is a low-lying state, naturally one may wonder whether such a state can be the ground state. Our HF/DFT calculations on Li@C_{180} predict a caged-electron state to be its ground state. We argue that this example shows a promising application of caged-electron states. One can form the target charge separated states needed for charge transfer at the moment of interest by inducing a photo-excitation process from the ground caged-electron state of large endohedral fullerene, such as Li@C_{180}. Also, this caged-electron state itself may have potential in application, due to its low-lying nature. In our opinion, the intriguing caged-electron states provide promising electronic properties of endohedral fullerenes, and may constitute the starting point of interest in new materials.

To better understand the nature of carbon cluster symmetry breaking, we investigated C_{20}^{-} ring anion, as an example of C_{4n} ring. Unlike the neutral C_{20} ring in D_{10h} symmetry, the anion structure at D_{10h} symmetry shows a considerable imaginary frequency. It leads to a ring of lower symmetry (C_{10h}), which possesses different radii. To predict the geometry change, the usual vibronic coupling mode are insufficient as very large vibrational distortions of normal modes are found to arise. Interestingly, our calculation proves that this symmetry breaking is not a result of a linear or bilinear coupling, but follows a much simpler model. Due to the extra electron, the ring anion shrinks to a smaller radius, compared to parent neutral carbon ring. The repelling ring strain forces the ring via the bond-angle alternating mode to result in C_{10h} symmetry. It is a great example of the complexity of carbon clusters. Much care must be taken when investigating the geometry of carbon clusters with high symmetry.

It is our hope that the present findings based on the high level calculation shed light on the electronic states as well as molecular structures of fullerenes, endohedral fullerenes and carbon rings, and, in particular, that our suggestion of possible applications of charge separated and caged-electron states of endohedral fullerenes will inspire further investigations.

Chapter 7

Acknowledgements

As an old saying goes, all good things must come to an end. After so many years in Heidelberg, now it is the end of my time as a PhD student of Heidelberg University. It’s time to thank the one who helped me in these years. My supervisor Prof. Lorenz S. Cederbaum is the first person whom I should thank. His advice always inspires me, encourages me and illuminates my way to pursue interesting findings. Over these years, I learned unforgettable lessons from his patience, rigorous and curious in science studies. Honestly speaking, it is a great honor to work with him.

Prof. Jochen Schirmer is the next person whom I should thank. After months of discussion and hundreds of emails, finally I finished this thesis with the help of Jochen’s valuable advice. In fact Jochen plays a more important role in my projects. With his great insight, he is the first one who finds the clue of caged-electron state. Without him, it may take several years until someone else discovers this attractive phenomenon. It is very lucky for me to have a chance to learn from him and work with him.

Moreover, I have to thank Prof. Horst Köppel and Prof. Hans-Dieter Meyer. Although I am not their student, still they are always gladly answering every stupid question I asked. I really learn a lot from them about their own fields, namely, conical intersection and MCTDH. It is great for me to learn from their decades' experience.

Additionally, I should not forget Dr. Shachar Klaiman and Dr. Evgeniy V. Gromov. They are the two post-doctors who I worked with. Their selfless guidance helps me transformed from a master student into a PhD student. Also I won’t forget their valuable contributions as my co-workers in those projects. I am so grateful for their help in these years.

Now it is time to thank my colleagues and friends in the group. For example, I would not forget the company of Dr. Victor Despré and Dr. Raphael Beinke, as we share the same office. I guess that is the reason why Victor knows me better than anyone else in the group. I also would like to thank Dr. Chong Yang (from IWR), Dr. Nikolay Golubev, Priv.-Doz. Dr. Alexander Kuleff, and Dr. Nikolai Kryzhevoi, who gave me valuable advice of the thesis. Of course, I would not forget Prof. Oriol Vendrell, as the founding father of our virtual tea time, and our technical supporter Dr. Markus Schröder. Also, I would not forget the happiness of tea time, Christmas dinner and other activities, with the accompany of previous and present team members. Due to the limited of space, I cannot write everyone’s name here, but trust me, the greatest lesson I learned here, is that only great companies can form an efficient science group.

Also, I realize that I have to thank my friends knew in China and Germany. When I feel lonely in Heidelberg, it’s their messages and phone calls, sometimes from thousands miles away, helps me pull myself together. It is your emotional support helps me overcome my difficulties.

Last but not least, I thank my family for the financial support, which protects me from disturbance and encourage me focusing on my own thesis.

Acknowledgements

Bibliography

[1] H. W. Kroto, J. R. Heath and S. C. O'Brien. C_{60}: Buckminsterfullerene [J]. *nature*, 1985, **318**, 162.

[2] R. F. Curl. Dawn of fullerenes: Conjecture and experiment (Nobel Lecture) [J]. *Angewandte Chemie International Edition in English*, 1997, **36**, 1566.

[3] R. D. Johnson, G. Meijer, and D. S. Bethune. C_{60} has icosahedral symmetry [J]. *Journal of the American Chemical Society*, 1990, **112**, 8983.

[4] Y. Ma, S. Y. Wang, J. Hu J, J. Zhang, J. Lin, S. Yang, and X. Song. Identification of Four C_{40} Isomers by Means of a Theoretical XPS/NEXAFS Spectra Study [J]. *The Journal of Physical Chemistry A*, 2018, **122**, 4750.

[5] M. Bodner, J. Patera, and M. Szajewska. Breaking of icosahedral symmetry: C_{60} to C_{70} [J]. *PloS one*, 2014, **9**, e84079.

[6] P. W. Fowler and A. Ceulemans. Electron deficiency of the fullerenes [J]. *The Journal of Physical Chemistry*, 1995, **99**, 508.

[7] T. Sternfeld, C. Thilgen, Z. Chen, S. Siefken, P. V. Schleyer, W. Thiel, F. Diederich, and M. Rabinovitz. Fullerene Anions of Different Sizes and Shapes: A ^{13}C NMR and Density-Functional Study [J]. *The Journal of organic chemistry*, 2003, **68**, 4850.

[8] A. Dreuw and L. S. Cederbaum. Multiply charged anions in the gas phase [J]. *Chemical reviews*, 2002, **102**, 181.

[9] J. Simons and K. D. Jordan. Ab initio electronic structure of anions [J]. *Chemical Reviews*, 1987, **87**, 535.

[10] J. Simons. Molecular anions [J]. *The Journal of Physical Chemistry A*, 2008, **112**, 6401.

[11] W. H. Green, S. M. Gorun, G. Fitzgerald, P. W. Fowler, A. Ceulemans, and B. C. Titeca. Electronic structures and geometries of C_{60} anions via density functional calculations [J]. *The Journal of Physical Chemistry*, 1996, **100**, 14892.

[12] H. Zettergren, M. Alcamí, and F. Martín. First-and second-electron affinities of C_{60} and C_{70} isomers [J]. *Physical Review A*, 2007, **76**, 043205.

[13] M. H. N. Janjanpour, M. Vakili, S. Daneshmehr, K. Jalalierad, and F. Alipour. Study of the Ionization Potential, Electron Affinity and HOMO-LUMO Gaps in the Small Fullerene Nanostructures [J]. *Chemical Review and Letters*, 2018, **1**, 45.

[14] S. Tsukamoto, M. Nakaya, V. Caciuc, N. Atodiresei, and T. Nakayama. Local dimerization and dedimerization of C_{60} molecules under a tip of scanning tunneling microscope: A first-principles study [J]. *Carbon*, 2020, **159**, 638.

[15] N. L. Nguyen, G. Borghi, A. Ferretti, I. Dabo, and N. Marzari. First-principles photoemission spectroscopy and orbital tomography in molecules from Koopmans-compliant functionals [J]. *Physical review letters*, 2015, **114**, 166405.

[16] Prakash Verma, A. Perera, and J. A. Morales. Massively parallel implementations of coupled-cluster methods for electron spin resonance spectra. I. Isotropic hyperfine coupling tensors in large radicals [J]. *The Journal of chemical physics*, 2013, **139**, 174103.

[17] D. M. Guldi and M. Prato. Excited-state properties of C_{60} fullerene derivatives [J]. *Accounts of chemical research*, 2000, **33**, 695.

[18] M. Feng, J. Zhao, and H. Petek. Atomlike, hollow-core–bound molecular orbitals of C_{60} [J].

Science, 2008, **320**, 359.

[19] H. Guo, C. Zhao, Q. Zheng, Z. Lan, O. V. Prezhdo, W. A. Saidi and J. Zhao. Superatom molecular orbital as an interfacial charge separation state [J]. *The journal of physical chemistry letters*, 2018, **9**, 3485.

[20] J. Zhao, M. Feng, J. Yang, and H. Petek. The superatom states of fullerenes and their hybridization into the nearly free electron bands of fullerites [J]. *ACS nano*, 2009, **3**, 853.

[21] M. Feng, J. Zhao, T. Huang, and H. Petek. The electronic properties of superatom states of hollow molecules [J]. *Accounts of chemical research*, 2011, **44**, 360.

[22] S. Hu, J. Zhao, Y. Jin, J. Yang, H. Petek and J. Hou. Nearly free electron superatom states of carbon and boron nitride nanotubes. *Nano letters*, 2010, **10**, 4830.

[23] J. R. Heath, S. C. O'Brien, Q. Zhang, Y. Liu, R. F. Curl, H. W. Kroto, F. K. Tittel, and R. E. Smalley. Lanthanum complexes of spheroidal carbon shells [J]. *Journal of the American Chemical Society*, 1985, **107**, 7779.

[24] A. A. Popov, S. Yan, and L. Dunsch. Endohedral fullerenes [J]. *Chemical reviews*, 2013, **113**, 5989.

[25] Y. He and Y. Li. Fullerene derivative acceptors for high performance polymer solar cells [J]. *Physical chemistry chemical physics*, 2011, **13**, 1970.

[26] F. D'Souza, R. Chitta, A. S. D. Sandanayaka, N. K. Subbaiyan, L. D'Souza, Y. Araki, and O. Ito. Supramolecular Carbon Nanotube-Fullerene Donor−Acceptor Hybrids for Photoinduced Electron Transfer [J]. *Journal of the American Chemical Society*, 2007, **129**, 15865.

[27] E. Castro, A. H. Garcia, G. Zavala, and L. Echegoyen. Fullerenes in biology and medicine [J]. *Journal of Materials Chemistry B*, 2017, **5**, 6523.

[28] G. O. Brink. Ionization of alkali atoms by electron bombardment [J]. *Physical Review*, 1962, **127**, 1204.

[29] E. F. Sheka. Donor–acceptor interaction and fullerene C_{60} dimerization [J]. *Chemical physics letters*, 2007, **438**, 119.

[30] K. Ohkubo, Y. Kawashima, and S. Fukuzumi. Strong supramolecular binding of $Li^+@C_{60}$ with sulfonated meso-tetraphenylporphyrins and long-lived photoinduced charge separation [J]. *Chemical Communications*, 2012, **48**, 4314.

[31] Y. Hou, X. Zhang, K. Chen, D. Liu, Z. Wang, Q. Liu, J. Zhao and A. Barbon. Charge separation, charge recombination, long-lived charge transfer state formation and intersystem crossing in organic electron donor/acceptor dyads [J]. *Journal of Materials Chemistry C*, 2019, **7**,12048.

[32] J. Lu, X. Zhang, and X. Zhao. Electronic structures of endohedral $Ca@C_{60}$, $Sc@C_{60}$ and $Y@C_{60}$ [J]. *Solid state communications*, 1999, **110**, 565.

[33] M. L. Tiago, P. R. C. Kent, R. Q. Hood, and F. A. Reboredo. Neutral and charged excitations in carbon fullerenes from first-principles many-body theories [J]. *The Journal of chemical physics*, 2008, **129**, 084311.

[34] I. D. Hands, J. L. Dunn, and C. A. Bates. Visualization of static Jahn-Teller effects in the fullerene anion C_{60}^- [J]. *Physical Review B*, 2010, **82**, 155425.

[35] M. Saito and Y. Okamoto. Second-order Jahn-Teller effect on carbon 4N+2 member ring clusters [J]. *Physical Review B*, 1999, **60**, 8939.

[36] E. Rashed and J. L. Dunn. Interactions between a water molecule and C_{60} in the endohedral fullerene $H_2O@C_{60}$ [J]. *Physical Chemistry Chemical Physics*, 2019, **21**, 3347.

[37] M. Saito and Y. Miyamoto. Vibration and vibronic coupling of C_{20} isomers: Ring, bowl, and

cage clusters [J]. *Physical Review B*, 2002, **65**, 165434.

[38] K. Kaiser, L. M. Scriven, F. Schulz, P. Gawel, L. Gross, and H. L. Anderson. An sp-hybridized molecular carbon allotrope, cyclo[18] carbon [J]. *Science*, 2019, **365**, 1299.

[39] É. Brémond, Á. J. Pérez-Jiménez, C. Adamo, and J. C. Sancho-García. sp-hybridized carbon allotrope molecular structures: An ongoing challenge for density-functional approximations [J]. *The Journal of Chemical Physics*, 2019, **151**, 211104.

[40] R. O. Jones. Density functional study of carbon clusters C_{2n} ($2\leqslant n\leqslant 16$). I. Structure and bonding in the neutral clusters [J]. *The Journal of chemical physics*, 1999, **110**, 5189.

[41] C. Neiss, E. Trushin, and A. Görling. The Nature of One-Dimensional Carbon: Polyynic versus Cumulenic [J]. *ChemPhysChem*, 2014, **15**, 249

[42] J. Čížek. On the correlation problem in atomic and molecular systems. Calculation of wavefunction components in Ursell-type expansion using quantum-field theoretical methods [J]. *The Journal of Chemical Physics*, 1966, **45**, 4256.

[43] M. Nooijen and R. J. Bartlett. Equation of motion coupled cluster method for electron attachment [J]. *The Journal of chemical physics*, 1995, **102**, 3629.

[44] E. Schrödinger. An undulatory theory of the mechanics of atoms and molecules [J]. *Physical review*, 1926, **28**, 1049.

[45] M. Born and R. Oppenheimer. Zur quantentheorie der molekeln [J]. *Annalen der physik*, 1927, **389**, 457.

[46] V. Fock. Konfigurationsraum und zweite Quantelung [J]. *Zeitschrift für Physik*, 1932, **75**, 622.

[47] J. C. Slater. A simplification of the Hartree-Fock method [J]. *Physical review*, 1951, **81**, 385.

[48] R. K. Nesbet. Configuration interaction in orbital theories [J]. *Proceedings of the Royal Society of London. Series A. Mathematical and Physical Sciences*, 1955, **230**, 312.

[49] L. S. Cederbaum. The multistate vibronic coupling problem [J]. *The Journal of Chemical Physics*, 1983, **78**, 5714.

[50] A. Hellman, B. Razaznejad, and B. I. Lundqvist. Potential-energy surfaces for excited states in extended systems [J]. *The Journal of chemical physics*, 2004, **120**, 4593.

[51] R. O. Jones and O. Gunnarsson. The density functional formalism, its applications and prospects [J]. *Reviews of Modern Physics*, 1989, **61**, 689.

[52] P. J. Knowles and H.-J. Werner. Internally contracted multiconfiguration-reference configuration interaction calculations for excited states [J]. *Theoretica chimica acta*, 1992, **84**, 95.

[53] K. R. Shamasundar, G. Knizia, and H.-J. Werner. A new internally contracted multi-reference configuration interaction method [J]. *The Journal of chemical physics*, 2011, **135**, 054101.

[54] S. Gozem, A. I. Krylov, and M. Olivucci. Conical intersection and potential energy surface features of a model retinal chromophore: Comparison of EOM-CC and multireference methods [J]. *Journal of chemical theory and computation*, 2013, **9**, 284.

[55] M. Saitow, A. J. Dutta, and F. Neese. Accurate Ionization Potentials, Electron Affinities and Electronegativities of Single-Walled Carbon Nanotubes by State-of-the-Art Local Coupled-Cluster Theory [J]. *Bulletin of the Chemical Society of Japan*, 2018, **92**, 170.

[56] B. Peng, N. Govind, E. Aprà, M. Klemm, J. R. Hammond, and K. Kowalski. Coupled cluster studies of ionization potentials and electron affinities of single-walled carbon nanotubes [J]. *The Journal of Physical Chemistry A*, 2017, **121**, 1328.

[57] G. E. Scuseria, C. L. Janssen, and H. F. Schaefer III. An efficient reformulation of the closed-shell coupled cluster single and double excitation (CCSD) equations [J]. *Journal of Chemical*

Physics, 1988, **89**, 7382.

[58] R. J. Bartlett and G. D. Purvis. Many-body perturbation theory, coupled-pair many-electron theory, and the importance of quadruple excitations for the correlation problem [J]. *International Journal of Quantum Chemistry*. 1978, **14**, 561.

[59] K. Raghavachari, G. W. Trucks, J. A. Pople, and M. Head-Gordon. A fifth-order perturbation comparison of electron correlation theories [J]. *Chemical Physics Letters*, 1989, **157**, 479.

[60] D. I. Lyakh, V. F. Lotrich, and R. J. Bartlett. The 'tailored' CCSD (T) description of the automerization of cyclobutadiene [J]. *Chemical Physics Letters*, 2011, **501**, 166.

[61] G. D. Purvis III and R. J. Bartlett. A full coupled-cluster singles and doubles model – the inclusion of disconnected triples [J]. *Journal of Chemical Physics*. 1982, **76**, 1910.

[62] T. J. Lee, A. P. Rendell, and P. R. Taylor. Comparison of the Quadratic Configuration Interaction and Coupled-Cluster Approaches to Electron Correlation Including the Effect of Triple Excitations [J]. *Journal of Physical Chemistry*, 1990, **94**, 5463.

[63] R. O. Ramabhadran and K. Raghavachari. Extrapolation to the gold-standard in quantum chemistry: Computationally efficient and accurate CCSD (T) energies for large molecules using an automated thermochemical hierarchy [J]. *Journal of chemical theory and computation*, 2013, **9**, 3986.

[64] J. D. Watts, J. Gauss, and R. J. Bartlett. Coupled-cluster methods with noniterative triple excitations for restricted open-shell Hartree–Fock and other general single determinant reference functions. Energies and analytical gradients [J]. *The Journal of chemical physics*, 1993, **98**, 8718.

[65] E. Dalgaard and H. J. Monkhorst. Some aspects of the time-dependent coupled-cluster approach to dynamic response functions [J]. *Physical Review A*, 1983, **28**, 121.

[66] R. Kobayashi, H. Koch, and P. Jørgensen. Calculation of frequency-dependent polarizabilities using coupled-cluster response theory [J]. *Chemical physics letters*, 1994, **219**, 30.

[67] H. Sekino and R. J. Bartlett. A linear response, coupled-cluster theory for excitation energy [J]. *International Journal of Quantum Chemistry*, 1984, **26**, 255.

[68] H. Koch and P. Jørgensen. Coupled cluster response functions [J]. *The Journal of Chemical Physics*, 1990, **93**, 3333.

[69] K. Kowalski and P. Piecuch. The active-space equation-of-motion coupled-cluster methods for excited electronic states: Full EOMCCSDt [J]. *The Journal of Chemical Physics*, 2001, **115**, 643.

[70] A. I. Krylov, C. D. Sherrill, and M. Head-Gordon. Excited states theory for optimized orbitals and valence optimized orbitals coupled-cluster doubles models [J]. *The Journal of Chemical Physics*, 2000, **113**, 6509.

[71] J. F. Stanton and R. J. Bartlett. The equation of motion coupled-cluster method. A systematic biorthogonal approach to molecular excitation energies, transition probabilities, and excited state properties [J]. *The Journal of chemical physics*, 1993, **98**, 7029.

[72] S. V. Levchenko and A. I. Krylov. Equation-of-motion spin-flip coupled-cluster model with single and double substitutions: Theory and application to cyclobutadiene [J]. *The Journal of chemical physics*, 2004, **120**, 175.

[73] H. Nakatsuji. Cluster expansion of the wavefunction. Electron correlations in ground and excited states by SAC (symmetry-adapted-cluster) and SAC CI theories [J]. *Chemical Physics Letters*, 1979, **67**, 329.

[74] H. Nakatsuji, K. Ohta, and K. Hirao. Cluster expansion of the wave function. Electron correlations in the ground state, valence and Rydberg excited states, ionized states, and electron

attached states of formaldehyde by SAC and SAC–CI theories [J]. *The Journal of Chemical Physics*, 1981, **75**, 2952.

[75] A. B. Trofimov, G. Stelter, and J. Schirmer. A consistent third-order propagator method for electronic excitation [J]. *The Journal of Chemical Physics*, 1999, **111**, 9982.

[76] J. H. Starcke, M. Wormit, and A. Dreuw. Nature of the lowest excited states of neutral polyenyl radicals and polyene radical cations [J]. *The Journal of chemical physics*, 2009, **131**, 144311.

[77] J. Schirmer and A. B. Trofimov. Intermediate state representation approach to physical properties of electronically excited molecules [J]. *The Journal of chemical physics*, 2004, **120**, 11449.

[78] J. F. Stanton. Coupled-cluster theory, pseudo-Jahn–Teller effects and conical intersections [J]. *The Journal of Chemical Physics*, 2001, **115**, 10382.

[79] I. Shavitt and R. J. Bartlett. Many-body methods in chemistry and physics: MBPT and coupled-cluster theory [M]. *Cambridge university press*, 2009; pp 442.

[80] S. Hirata, M. Nooijen, and R. J. Bartlett. High-order determinantal equation-of-motion coupled-cluster calculations for electronic excited states [J]. *Chemical Physics Letters*, 2000, **326**, 255-262.

[81] M. Musiał and R. J. Bartlett. Addition by subtraction in coupled cluster theory. II. Equation-of-motion coupled cluster method for excited, ionized, and electron-attached states based on the n CC ground state wave function [J]. *The Journal of chemical physics*, 2007, **127**, 024106.

[82] M. Musiał and R. J. Bartlett. Equation-of-motion coupled cluster method with full inclusion of connected triple excitations for electron-attached states: EA-EOM-CCSDT [J]. *The Journal of chemical physics*, 2003, **119**, 1901.

[83] P. U. Manohar, J. F. Stanton, and A. I. Krylov. Perturbative triples correction for the equation-of-motion coupled-cluster wave functions with single and double substitutions for ionized states: Theory, implementation, and examples [J]. *The Journal of chemical physics*, 2009, **131**, 114112.

[84] P. Pulay. in Modern Electronic Structure Theory; D. R. Yarkony, Ed [M]. World Scientific, Singapore, 1995, Vol. **2**; pp 1191.

[85] A. C. Scheiner, G. E. Scuseria, J. E. Rice, T. J. Lee, and H. F. Schaefer III. Analytic evaluation of energy gradients for the single and double excitation coupled cluster (CCSD) wave function: Theory and application [J]. *The Journal of chemical physics*, 1987, **87**, 5361.

[86] M. Kállay, J. Gauss, and P. G. Szalay. Analytic first derivatives for general coupled-cluster and configuration interaction models [J]. *The Journal of chemical physics*, 2003, **119**, 2991.

[87] J. F. Stanton. Many-body methods for excited state potential energy surfaces. I. General theory of energy gradients for the equation-of-motion coupled-cluster method [J]. *The Journal of chemical physics*, 1993, **99**, 8840.

[88] J. F. Stanton and J. Gauss. Analytic energy derivatives for ionized states described by the equation-of-motion coupled cluster method [J]. *The Journal of chemical physics*, 1994, **101**, 8938-8944.

[89] J. F. Stanton and J. Gauss. Analytic energy gradients for the equation-of-motion coupled-cluster method: implementation and application to the HCN/HNC system [J]. *The Journal of chemical physics*, 1994, **100**, 4695.

[90] E. A. Rohlfing, D. M. Cox, and A. Kaldor. Production and characterization of supersonic carbon cluster beams [J]. *The Journal of chemical physics*, 1984, **81**, 3322.

[91] J. Brant, H. Lecoanet, M. Hotze, and M. Wiesner. Comparison of electrokinetic properties of colloidal fullerenes (n-C_{60}) formed using two procedures [J]. *Environmental science & technology*,

2005, **39**, 6343.

[92] D. Toffoli and P. Decleva. Strong oscillations in the nondipole corrections to the photoelectron angular distributions from C_{60} [J]. *Physical Review A*, 2010, **81**, 061201.

[93] J. O. Johansson, G. G. Henderson, F. Remacle, and E. E. B. Campbell. Angular-resolved photoelectron spectroscopy of superatom orbitals of fullerenes [J]. *Physical review letters*, 2012, **108**, 173401.

[94] X.-B. Wang, C.-F. Ding, and L.-S. Wang. High resolution photoelectron spectroscopy of C_{60}^{-} [J]. *The Journal of chemical physics*, 1999, **110**, 8217.

[95] V. Buntar and H. W. Weber. Magnetic properties of fullerene superconductors [J]. *Superconductor Science and Technology*, 1996, **9**, 599.

[96] A. F. Hebard, M. Rosseinky, R. C. Haddon, D. W. Murphy, S. H. Glarum, T. Palstra, A. P. Ramirez and A. R. Kortan. Superconductivity at 18 K in Potassium-doped C_{60} [J]. *Nature*, 1991, **350**, 600.

[97] J. H. Schön, C. Kloc, and B. Batlogg. High-temperature superconductivity in lattice-expanded C_{60} [J]. *Science*, 2001, **293**, 2432.

[98] J. Stinchcombe, A. Penicaud, P. Bhyrappa, P. D. W. Boyd, and C. A. Reed. Buckminsterfulleride (1-) salts: synthesis, EPR, and the Jahn-Teller distortion of C_{60} [J]. *Journal of the American Chemical Society*, 1993, **115**, 5212.

[99] F. Negri, G. Orlandi, and F. Zerbetto. Quantum-chemical investigation of Franck-Condon and Jahn-Teller activity in the electronic spectra of Buckminsterfullerene [J]. *Chemical physics letters*, 1988, **144**, 31.

[100] J. L. Dunn, H. S. Alqannas, and A. J. Lakin. Jahn–Teller effects and surface interactions in multiply-charged fullerene anions and the effect on scanning tunneling microscopy images [J]. *Chemical Physics*, 2015, **460**, 14.

[101] K. Ohkubo, Y. Kawashima, H. Sakai, T. Hasobe, and S. Fukuzumi. Enhanced photoelectrochemical performance of composite photovoltaic cells of $Li^{+}@C_{60}$–sulphonated porphyrin supramolecular nanoclusters [J]. *Chemical Communications*, 2013, **49**, 4474.

[102] H. Ueno, H. Kawakami, K. Nakagawa, H. Okada, N. Ikuma, S. Aoyagi, K. Kokubo, Y. Matsuo, and T. Oshima. Kinetic Study of the Diels–Alder Reaction of $Li^{+}@C_{60}$ with Cyclohexadiene: Greatly Increased Reaction Rate by Encapsulated Li^{+} [J]. *Journal of the American Chemical Society*, 2014, **136**, 11162.

[103] S. Aoyagi, E. Nishibori, H. Sawa, K. Sugimoto, M. Takata, Y. Miyata, R. Kitaura, H. Shinohara, H. Okada, T. Sakai, Y. Ono, K. Kawachi, K. Yokoo, S. Ono, K. Omote, Y. Kasama, S. Ishikawa, T. Komuro and H. Tobita. A layered ionic crystal of polar $Li@C_{60}$ superatoms [J]. *Nature chemistry*, 2010, **2**, 678.

[104] X.-J. Zhang, M.-Q. Long, K.-Q. Chen, Z. Shuai, Q. Wan, B. S. Zou and Z. Zhang. Electronic transport properties in doped C_{60} molecular devices [J]. *Applied Physics Letters*, 2009, **94**, 073503.

[105] T. Okazaki, Y. F. Lian, Z. N. Gu, K. Suenaga, and H. Shinohara. Isolation and spectroscopic characterization of Sm-containing metallofullerenes [J]. *Chemical Physics Letters*, 2000, **320**, 435.

[106] A. Rosén and B. Wästberg. Calculations of the ionization thresholds and electron affinities of the neutral, positively and negatively charged C_{60}—"follene-60" [J], *The Journal of chemical physics*, 1989, **90**, 2525.

[107] C. Brink, L. H. Andersen, P. Hvelplund, P. D. Mathur, and J. D. Voldstad. Laser photodetachment of C_{60}^{-} and C_{70}^{-} ions cooled in a storage ring [J], *Chemical Physics Letters*, 1995,

233, 52.

[108] G. Chen, R. G. Cooks, E. Corpuz, and L. T. Scott. Estimation of the electron affinities of C_{60}, corannulene, and coronene by using the kinetic method [J]. *Journal of the American Society for Mass Spectrometry*, 1996, **7**, 619.

[109] T. T. Clikeman, S. H. M. Deng, A. A. Popov, X.-B. Wang, S. H. Strauss, and O. V. Boltalina. Fullerene cyanation does not always increase electron affinity: an experimental and theoretical study [J]. *Physical Chemistry Chemical Physics*, 2015, **17**, 551.

[110] D.-L. Huang, P.-D. Dau, H.-T. Liu, and L.-S. Wang. High-resolution photoelectron imaging of cold C_{60}^- anions and accurate determination of the electron affinity of C_{60} [J]. *The Journal of chemical physics*, 2014, **140**, 224315.

[111] V. G. Zakrzewski, O. Dolgounitcheva, and J. V. Ortiz. Electron propagator calculations on the ground and excited states of C_{60}^- [J]. *The Journal of Physical Chemistry A*, 2014, **118**, 7424.

[112] V. K. Voora, L. S. Cederbaum, and K. D. Jordan. Existence of a correlation bound s-type anion state of C_{60} [J]. *The journal of physical chemistry letters*, 2013, **4**, 849.

[113] S. Klaiman, E. V. Gromov, and L. S. Cederbaum. Extreme correlation effects in the elusive bound spectrum of C_{60}^-[J]. *The Journal of Physical Chemistry Letters*, 2013, **4**, 3319.

[114] S. Klaiman, E. V. Gromov, and L. S. Cederbaum. All for one and one for all: Accommodating an extra electron in C_{60} [J]. *Physical Chemistry Chemical Physics*, 2014, **16**, 13287.

[115] E. V. Gromov, S. Klaiman, and L. S. Cederbaum. How many bound valence states does the C_{60}^- anion have? [J]. *Physical Chemistry Chemical Physics*, 2016, **18**, 10840.

[116] J. O. Johansson and E. E. B. Campbell. Probing excited electronic states and ionization mechanisms of fullerenes [J]. *Chemical Society Reviews*, 2013, **42**, 5661.

[117] L. Zoppi, L. Martin-Samos, and K. K. Baldridge. Buckybowl superatom states: a unique route for electron transport? [J]. *Physical Chemistry Chemical Physics*, 2015, **17**, 6114.

[118] E. V. Gromov, S. Klaiman, and L. S. Cederbaum. Influence of caged noble-gas atom on the Superatom and valence states of C_{60}^- [J]. *Molecular Physics*, 2015, **113**, 2964.

[119] H. Prinzbach, A. Weiler, P. Landenberger, F. Wahl, J. Wörth, L. T. Scott, M. Gelmont, D. Olevano, and B. V. Issendorff. Gas-phase production and photoelectron spectroscopy of the smallest fullerene, C_{20} [J], *Nature*, 2000, **407**, 60.

[120] F. A. Gianturco, G. Y. Kashenock, R. R. Lucchese, and N. Sanna. Low-energy resonant structures in electron scattering from C_{20} fullerene [J]. The Journal of chemical physics, 2002, 116, 2811.

[121] G. Galli, F. Gygi, and J. C. Golaz. Vibrational and electronic properties of neutral and negatively charged C_{20} clusters [J]. *Physical Review B*, 1998, **57**, 1860.

[122] B. N. Plakhutin and A. V. Arbuznikov. Spectrum of states in icosahedral structures with g^N electronic configuration (n= 1–7). 2. Ab initio calculation of the C_{20} (I_h) molecule and its anions [J]. *Journal of structural chemistry*, 1997, **38**, 501.

[123] C. Zhang, W. Sun, and Z. Cao. Most stable structure of fullerene [20] and its novel activity toward addition of alkene: A theoretical study [J]. *The Journal of chemical physics*, 2007, **126**, 144306.

[124] Y. Jin, A. Perera, V. F. Lotrich, and R. J. Bartlett. Coupled cluster geometries and energies of C_{20} carbon cluster isomers–A new benchmark study [J]. *Chemical Physics Letters*, 2015, **629**, 76.

[125] T. H. Dunning. Jr. Gaussian basis sets for use in correlated molecular calculations. I. The atoms boron through neon and hydrogen [J]. *The Journal of chemical physics*, 1989, **90**, 1007.

[126] M. J. Frisch, M. Head-Gordon, and J. A. Pople. Direct MP2 gradient method [J]. *Chemical Physics Letters*, 1990, **166**, 275.

[127] P. J. Stephens, F. J. Devlin, C. F. Chabalowski, and M. J. Frisch. Ab initio calculation of vibrational absorption and circular dichroism spectra using density functional force fields [J]. *The Journal of physical chemistry*, 1994, **98**, 11623.

[128] M. J. Frisch, G. W. Trucks, H. B. Schlegel, G. E. Scuseria, M. A. Robb, J. R. Cheeseman, G. Scalmani, V. Barone, B. Mennucci, and G. A. Petersson, et al., Gaussian 09, Revision D.01, Gaussian, Inc, Wallingford CT, 2013.

[129] H.-J. Werner, P. J. Knowles, G. Knizia, F. R. Manby, M. Schütz, P. Celani, W. Györffy, D. Kats, T. Korona, R. Lindh, A. Mitrushenkov, G. Rauhut, K. R. Shamasundar, T. B. Adler, R. D. Amos, A. Bernhardsson, A. Berning, D. L. Cooper, M. J. O. Deegan, A. J. Dobbyn, F. Eckert, E. Goll, C. Hampel, A. Hesselmann, G. Hetzer, T. Hrenar, G. Jansen, C. Ko¨ppl, Y. Liu, A. W. Lloyd, R. A. Mata, A. J. May, S. J. McNicholas, W. Meyer, M. E. Mura, A. Nicklaß, D. P. O'Neill, P. Palmieri, D. Peng, K. Pflüger, R. Pitzer, M. Reiher, T. Shiozaki, H. Stoll, A. J. Stone, R. Tarroni, T. Thorsteinsson and M. Wang, MOLPRO is a package of ab initio programs, 2012.

[130] P. O. Widmark, P. A. Malmqvist, and B. Roos. Density matrix averaged atomic natural orbital (ANO) basis sets for correlated molecular wave functions [J], Theoretica chimica acta, 1990, 77, 291.

[131] CFOUR, a quantum chemical program package written by J. F. Stanton, J. Gauss, L. Cheng, M. E. Harding, D. A. Matthews, P. G. Szalay with contributions from A. A. Auer, R. J. Bartlett, U. Benedikt, C. Berger, D. E. Bernholdt, Y. J. Bomble, O. Christiansen, F. Engel, R. Faber, M. Heckert, O. Heun, C. Huber, T.-C. Jagau, D. Jonsson, J. Jusélius, K. Klein, W. J. Lauderdale, F. Lipparini, T. Metzroth, L. A. Mück, D. P. O'Neill, D. R. Price, E. Prochnow, C. Puzzarini, K. Ruud, F. Schiffmann, W. Schwalbach, C. Simmons, S. Stopkowicz, A. Tajti, J. Vázquez, F. Wang, J. D. Watts and the integral packages MOLECULE (J. Almlöf and P. R. Taylor), PROPS (P. R. Taylor), ABACUS (T. Helgaker, H. J. Aa. Jensen, P. Jørgensen, and J. Olsen), and ECP routines by A. V. Mitin and C. van Wüllen. For the current version, see http://www.cfour.de.

[132] Z. Wang, K. Lian, S. Pan, and X. Fan. A path from I_h to C_1 symmetry for C_{20} cage molecule [J]. Journal of computational chemistry, 2005, 26,1279.

[133] J. C. Rienstra-Kiracofe, G. S. Tschumper, H. F. Schaefer III, S. Nandi, and G. B. Ellison. Atomic and molecular electron affinities: photoelectron experiments and theoretical computations [J]. *Chemical reviews*, 2002, **102**, 231.

[134] TURBOMOLE V 6.2, a development of University of Karlsruhe and Forschungszentrum Karlsruhe GmbH, 1989–2007, TURBOMOLE GmbH, since 2007, available from http:// www.turbomole.com, 2010.

[135] T. Debnath, J. K. Saha, T. Banu, T. Ash, and A. K. Das. Structural and thermodynamic aspects of $Li_n@C_x$ endohedral metallofullerenes: a DFT approach [J]. *Theoretical Chemistry Accounts*, 2016, **135**, 167.

[136] G.-Z. Zhu, Y. Liu, Y. Hashikawa, Q.-F. Zhang, Y. Murata, and L.-S. Wang. Probing the interaction between the encapsulated water molecule and the fullerene cages in $H_2O@C_{59}N^-$ and $H_2O@C_{60}^-$ [J]. *Chemical science*, 2018, **9**, 5666.

[137] E. Brocławik and A. Eilmes. Density functional study of endohedral complexes $M@C_{60}$ (M= Li, Na, K, Be, Mg, Ca, La, B, Al): electronic properties, ionization potentials, and electron affinities [J]. *The Journal of chemical physics*, 1998, **108**, 3498.

[138] H. Shinohara. Endohedral metallofullerenes [J]. *Reports on Progress in Physics*, 2000, **63**, 843.

[139] L.-S. Wang, J. M. Alford, Y. Chai, M. Diener, and R. E. Smalley. Photoelectron spectroscopy and electronic structure of Ca@C_{60} [J]. *Zeitschrift für Physik D Atoms, Molecules and Clusters*, 1993, **26**, 297.

[140] O. V. Boltalina, I. N. Ioffe, I. D. Sorokin, and L. N. Sidorov. Electron affinity of some endohedral lanthanide fullerenes [J]. *The Journal of Physical Chemistry A*, 1997, **101**, 9561.

[141] X. H. Chen and G. Roth. Superconductivity at 8K in samarium-doped C_{60} [J]. *Physical Review B*, 1995, **52**, 15534.

[142] H. Gergeroglu, S. Yildirim, and M. F. Ebeoglugil. Nano-carbons in biosensor applications: an overview of carbon nanotubes (CNTs) and fullerenes (C_{60}) [J]. *SN Applied Sciences*, 2020, **2**, 1.

[143] A. Nakagawa, M. Nishino, H. Niwa, K. Ishino, Z. Wang, H. Omachi, K. Furukawa, T. Yamaguchi, T. Kato, S. Bandow, J. Rio, C. Ewels, S. Aoyagi, and H. Shinohara. Crystalline functionalized endohedral C_{60} metallofullerides [J]. *Nature communications*, 2018, **9**, 3073.

[144] C. Z. Gao, P. Wopperer, P. M. Dinh, E. Suraud, and P.-G. Reinhard. On the dynamics of photo-electrons in C_{60} [J]. *Journal of Physics B: Atomic, Molecular and Optical Physics*, 2015, **48**, 105102.

[145] J. L. Segura, N. Martín, and D. M. Guldi. Materials for organic solar cells: the C_{60}/π-conjugated oligomer approach [J]. *Chemical Society Reviews*, 2005, **34**, 31.

[146] N. L. Bill, M. Ishida, S. Bälhring, J. M. Lim, S. Lee, C. M. Davis, V. M. Lynch, K. A. Nielsen, J. O. Jeppesen, K. Ohkubo, S. Fukuzumi, D. Kim, and J. L. Sessler. Porphyrins fused with strongly electron-donating 1, 3-dithiol-2-ylidene moieties: redox control by metal cation complexation and anion binding [J]. *Journal of the American Chemical Society*, 2013, **135**, 10852.

[147] Z. Slanina, F. Uhlík, S.-L. Lee, and L. Adamowicz. Quantum-chemical calculations of model systems of interest in fullerene-based superconductivity [J]. *Journal of low temperature physics*, 2003, **131**, 1259.

[148] H. Ueno, S. Aoyagi, Y. Yamazaki, K. Ohkubo, N. Ikuma, H. Okada, T. Kato, Y. Matsuo, S. Fukuzumi, and K. Kokubo. Electrochemical reduction of cationic $Li^+@C_{60}$ to neutral $Li^+@C_{60}^-$: isolation and characterisation of endohedral [60] fulleride [J]. *Chemical science*, 2016, **7**, 5770.

[149] M. Pavanello, A. F. Jalbout, B. Trzaskowski, and L. Adamowicz. Fullerene as an electron buffer: Charge transfer in Li@C_{60} [J]. *Chemical physics letters*, 2007, **442**, 339.

[150] T. Kamimura, K. Ohkubo, Y. Kawashima, S. Ozako, K. Sakaguchi, S. Fukuzumi, and F. Tani. Long-lived photoinduced charge separation in inclusion complexes composed of a phenothiazine-bridged cyclic porphyrin dimer and fullerenes [J]. *The Journal of Physical Chemistry C*, 2015, **119**, 25634.

[151] Z. Wang, X. Ke, Z. Zhu, F. Zhu, M. Ruan, H. Chen, R. Huang, and L. Zheng. A new carbon solid made of the world's smallest caged fullerene C_{20} [J]. *Physics Letters A*, 2001, **280**, 351.

[152] G. v. Von Helden, M. T. Hsu, N. G. Gotts, P. R. Kemper, and M. T. Bowers. Do small fullerenes exist only on the computer? Experimental results on $C^{=/-}{}_{20}$ and $C^{+/-}{}_{24}$ [J]. *Chemical physics letters*, 1993, **204**, 15.

[153] I. Spagnolatti, M. Bernasconi, and G. Benedek. Ab-initio Study of Electron-Phonon Interaction in Cluster-Assembled Carbon Materials [J]. *Europhysics Letters*, 2002, **59**, 572.

[154] X.-B. Wang, H.-K. Woo, and L.-S. Wang. Vibrational cooling in a cold ion trap: Vibrationally resolved photoelectron spectroscopy of cold C_{60}^- anions[J]. *The Journal of chemical physics*, 2005, **123**, 051106.

[155] Y.-F. Yang, S. Klaiman, E. V. Gromov, and L. S. Cederbaum. Bound electronic states of the smallest fullerene C_{20}^{-} anion [J]. *Physical Chemistry Chemical Physics*, 2018, **20**, 17434.

[156] H. Li, B. Mignolet, Z. Wang, K. J. Betsch, K. D. Carnes, I. Ben-Itzhak, C. L. Cocke, F. Remacle, and M. F. Kling. Transition from SAMO to Rydberg state ionization in C_{60} in femtosecond laser fields [J]. *The journal of physical chemistry letters*, 2016, **7**, 4677.

[157] Y. P. An, C. L. Yang, M. S. Wang, X. G. Ma, and D. H. Wang. First-principles study of transport properties of endohedral $Li@C_{20}$ metallofullerene [J]. *Current Applied Physics*, 2010, **10**, 260.

[158] Y. P. An, C. L. Yang, M. S. Wang, X. G. Ma, and D. H. Wang. Geometrical and Electronic Properties of the Clusters of C_{20} Cage Doped with Alkali Metal Atoms [J]. *Journal of Cluster Science*, 2011, **22**, 31.

[159] J.-D. Chai and M. Head-Gordon. Long-range corrected hybrid density functionals with damped atom–atom dispersion corrections [J]. *Physical Chemistry and Chemical Physics*, 2008, **10**, 6615.

[160] M. J. Frisch, G. W. Trucks, H. B. Schlegel, G. E. Scuseria, M. A. Robb, J. R. Cheeseman, G. Scalmani, V. Barone, B. Mennucci, G. A. Petersson, H. Nakatsuji, M. Caricato, X. Li, H. P. Hratchian, A. F. Izmaylov, J. Bloino, G. Zheng, J. L. Sonnenberg, M. Hada, M. Ehara, K. Toyota, R. Fukuda, J. Hasegawa, M. Ishida, T. Nakajima, Y. Honda, O. Kitao, H. Nakai, T. Vreven, J. A. Montgomery, Jr., J. E. Peralta, F. Ogliaro, M. Bearpark, J. J. Heyd, E. Brothers, K. N. Kudin, V. N. Staroverov, R. Kobayashi, J. Normand, K. Raghavachari, A. Rendell, J. C. Burant, S. S. Iyengar, J. Tomasi, M. Cossi, N. Rega, J. M. Millam, M. Klene, J. E. Knox, J. B. Cross, V. Bakken, C. Adamo, J. Jaramillo, R. Gomperts, R. E. Stratmann, O. Yazyev, A. J. Austin, R. Cammi, C. Pomelli, J. W. Ochterski, R. L. Martin, K. Morokuma, V. G. Zakrzewski, G. A. Voth, P. Salvador, J. J. Dannenberg, S. Dapprich, A. D. Daniels, Ö. Farkas, J. B. Foresman, J. V. Ortiz, J. Cioslowski, and D. J. Fox, GAUSSIAN 09, Revision E.01, Gaussian, Inc., Wallingford, CT, 2009.

[161] D. Manna and T. K. Ghanty. Theoretical prediction of icosahedral $U@C_{20}$ and analogous systems with high HOMO–LUMO gap [J]. *The Journal of Physical Chemistry C*, 2012, **116**, 16716.

[162] N. N. Breslavskaya, A. A. Levin, and A. L. Buchachenko. Endofullerenes: size effects on structure and energy [J]. *Russian chemical bulletin*, 2004, **53**, 18.

[163] F. Meng, Z. Zhou, P. Zhang, M. Jiang, X. Xu, Y. Wang, J. Gou, D. Hui, and D. Die. Encapsulation of an f-block metal atom/ion to enhance the stability of C_{20} with the I_h symmetry [J]. *Physical Chemistry and Chemical Physics*, 2015, **17**, 4328.

[164] J. Hernández-Rojas, J. Bretón, and J. M. Gomez Llorente. On the rotational spectra of endohedral atoms at fullerenes: the off-centre case [J]. *Chemical physics letters*, 1995, **237**, 115.

[165] P. R. Taylor, E. Bylaska, J. H. Weare, and Ryoichi, Kawai. C_{20}: fullerene, bowl or ring? New results from coupled-cluster calculations [J]. *Chemical physics letters*, 1995, **235**, 558.

[166] F. Diederich and M. Gómez-López. Supramolecular Fullerene' Chemistry [J]. *Chemical Society Reviews*, 1999, **28**, 263.

[167] C. A. Reed, K.-C. Kim, R. D. Bolskar, and L. J. Mueller. Taming Superacids: Stabilization of the Fullerene Cations HC_{60}^{+} and $C_{60}^{\cdot+}$ [J]. *Science*, 2000, **289**, 101.

[168] N. Iwahara, T. Sato, K. Tanaka, and L. F. Chibotaru. Vibronic Coupling in C_{60}^{-} Anion Revisited: derivations from Photoelectron Spectra and DFT Calculations [J]. *Physical Review B*, 2010, **82**, 245409.

[169] V. Averbukh and L. S. Cederbaum. Interatomic Electronic Decay in Endohedral Fullerenes [J]. *Physical Review Letters*, 2006, **96**, 053401.

[170] T. Erb, U. Zhokhavets, G. Gobsch, S. Raleva, B. Stühn, P. Schilinsky, C. Waldauf, and C. J. Brabec. Correlation Between Structural and Optical Properties of Composite Polymer/Fullerene Films for Organic Solar Cells [J]. *Advanced Functional Materials*, 2005, **15**, 1193.

[171] A. Pivrikas, N. S. Sariciftci, G. Juška, and R. Österbacka. A Review of Charge Transport and Recombination in Polymer/Fullerene Organic Solar Cells [J]. *Progress in Photovoltaics: Research and Applications*, 2007, **15**, 677.

[172] H. Hoppe, N. Arnold, N. S. Sariciftci, and D. Meissner. Modeling the Optical Absorption Within Conjugated Polymer/Fullerene-based Bulk-heterojunction Organic [J]. *Solar energy materials and solar cells*, 2003, **80**, 105.

[173]H. Hoppe and N. S. Sariciftci. Organic Solar Cells: An Overview [J]. *Journal of materials research*, 2004, **19**, 1924.

[174] S. Xiong, F. Yang, H. Jiang, J. Ma, and X. Lu. Covalently Bonded Polyaniline/Fullerene Hybrids with Coral-like Morphology for High-performance Supercapacitor [J]. *Electrochimica acta*, 2012, **85**, 235.

[175] V. Yong and T. H. Hahn. Synergistic Effect of Fullerene-capped Gold Nanoparticles on Graphene Electrochemical Supercapacitors [J]. *Advances in Nanoparticles*. 2013, **2**, 1.

[176] H. Wang, X. Yan, and G. Piao. A High-performance Supercapacitor Based on Fullerene C_{60} Whisker and Polyaniline Emeraldine Base Composite [J]. *Electrochimica acta*, 2017, **231**, 264.

[177] F. D'Souza and O. Ito. Supramolecular Donor-acceptor Hybrids of Porphyrins/Phthalocyanines with Fullerenes/Carbon Nanotubes: Electron Transfer, Sensing, Switching, and Catalytic Applications [J]. *Chemical Communications*, 2009, **33**, 4913.

[178] B. S. Sherigara, W. Kutner, and F. D'Souza. Electrocatalytic Properties and Sensor Applications of Fullerenes and Carbon Nanotubes [J]. *Electroanalysis: An International Journal Devoted to Fundamental and Practical Aspects of Electroanalysis*, 2003, **15**, 753.

[179] B. Li and Z. Xu. A Nonmetal Catalyst for Molecular Hydrogen Activation with Comparable Catalytic Hydrogenation Capability to Noble Metal Catalyst [J]. *Journal of the American Chemical Society*, 2009, **131**, 16380.

[180] S. Chakravarty, M. P. Gelfand, and S. Kivelson. Electronic Correlation Effects and Superconductivity in Doped Fullerenes [J]. *Science*, 1991, **254**, 970.

[181] K. V. Grigorishin. The Role of Electron-vibron Interaction and Local Pairing in Conductivity and Superconductivity of Alkali-doped Fullerides. [J]. *Physica C: Superconductivity and its Applications*, 2019, **562**, 56.

[182] M. Menelaou, Y. Takabayashi, H. E. Okur, R. H. Zadik, and K. Prassides. Structural and Electronic Response of Overexpanded Superconducting Fullerides Close to the Mott Insulator Boundary [J]. *International Journal of Modern Physics B*, 2018, **32**, 1840020.

[183] R. Arita, T. Koretsune, S. Sakai, R. Akashi, Y. Nomura, and W. Sano. Nonempirical Calculation of Superconducting Transition Temperatures in Light-Element Superconductors [J]. *Advanced Materials*, 2017, **29**, 1602421.

[184] I. Lahiri and C. Wonbong. Carbon Nanostructures in Lithium Ion Batteries: past, present, and future [J]. *Critical Reviews in Solid State and Materials Sciences*, 2013, **38**, 128.

[185] R. Tellgmann, N. Krawez, S.-H. Lin, I. V. Hertel, and E. E. B. Campbell. Endohedral Fullerene Production [J]. *Nature*, 1996, **382**, 407.

[186] I. Jeon, H. Ueno, S. Seo, K. Aitola, R. Nishikubo, A. Saeki, H. Okada, G. Boschloo, S. Maruyama, and Y. Matsuo. Lithium-Ion Endohedral Fullerene ($Li^+@C_{60}$) Dopants in Stable

Perovskite Solar Cells Induce Instant Doping and Anti-Oxidation [J]. *Angewandte Chemie International Edition*, 2018, **57**, 4607.

[187] Y. Kawashima, K. Ohkubo, and S. Fukuzumi. Enhanced Photoinduced Electron-transfer Reduction of Li@C_{60} in Comparison with C_{60} [J]. *The Journal of Physical Chemistry A*, 2012, **116**, 8942.

[188] S. Fukuzumi, K. Ohkubo, Y. Kawashima, D. S. Kim, J. S. Park, A. Jana, V. M. Lynch, M. Vincent, D. Kim, and J. L. Sessler. Ion-Controlled On-Off Switch of Electron Transfer from Tetrathiafulvalene Calix[4]pyrroles to Li^+@C_{60} [J]. *Journal of the American Chemical Society*, 2011, **133**, 15938.

[189] H. J. Chandler, M. Stefanou, E. E. B. Campbell, and R. Schaub. Li@C_{60} as A Multi-state Molecular Switch [J]. *Nature communications*, 2019, **10**, 2283.

[190] Y. Kawashima, K. Ohkubo, and S. Fukuzumi. Efficient Charge Separation in Li@C_{60} Supramolecular Complexes with Electron Donors [J]. *Chemistry–An Asian Journal*, 2015, **10**, 44.

[191] Y. Kawashima, K. Ohkubo, M. Kentaro, and S. Fukuzumi. Electron Transfer in a Supramolecular Complex of Zinc Chlorin Carboxylate Anion with Li^+@C_{60} Affording the Long-Lived Charge-Separated State [J]. *The Journal of Physical Chemistry C*, 2013, **117**, 21166.

[192] Y.-F. Yang, E. V. Gromov, and L. S. Cederbaum. Charge Separated States of Endohedral Fullerene Li@C_{20} [J]. *The Journal of chemical physics*, 2019, **151**, 114306.

[193] H. Ueno, I. Jeon, H. S. Lin, A. Thote, T. Nakagawa, H. Okada, S. Izawa, M. Hiramoto, H. Daiguji, S. Maruyama, and Y. Matsuo. Li@C_{60} endohedral fullerene as a supraatomic dopant for C_{60} electron-transporting layers promoting the efficiency of perovskite solar cells [J]. *Chemical Communications*, 2019, **55**, 11837.

[194] A. J. Stasyuk, O. A. Stasyuk, M. Solà, and A. A. Voityuk. Hypsochromic solvent shift of the charge separation band in ionic donor-acceptor Li^+@$C_{60}\subset$[10]CPP [J]. *Chemical Communications*, 2019, **55**, 11195.

[195] Y. Zhao and D. G. Truhlar. The M06 suite of density functionals for main group thermochemistry, thermochemical kinetics, noncovalent interactions, excited states, and transition elements: two new functionals and systematic testing of four M06-class functionals and 12 other functionals [J]. *Theoretical Chemistry Accounts*, 2008, **120**, 215.

[196] R. Polly, H.-J. Werner, F. R. Manby, and P. J. Knowles. Fast Hartree-Fock Theory Using Local Density Fitting Approximations [J]. *Molecular Physics*, 2004, **102**, 2311.

[197] K. Hedberg, L. Hedberg, D. S. Bethune, C. A. Brown, H. C. Dorn, R. D. Johnson, and M. De Vries. Bond Lengths in Free Molecules of Buckminsterfullerene, C_{60}, from Gas-Phase Electron Diffraction [J]. *Science.* 1991, **254**, 410412.

[198] E. Bohl, K. P. Sokół, B. Mignolet, J. O. F. Thompson, J. Olof Johansson, F. Remacle, and E. E. B. Campbell. Relative photoionization cross sections of super-atom molecular orbitals (SAMOs) in C_{60} [J]. *The Journal of Physical Chemistry A*, 2015, **119**, 11504.

[199] M. Feng and H. Petek. Scrutinizing the Endohedral Space: Superatom States and Molecular Machines. In Endohedral Fullerenes: Electron Transfer and Spin; Popov, A. A., Ed [M]. Springer International Publishing: Switzerland, 2017; pp 123−157.

[200] B. Mignolet, J. O. Johansson, E. E. B. Campbell, and F. Remacle. Probing Rapidly-Ionizing Super-Atom Molecular Orbitals in C_{60}: A Computational and Femtosecond Photoelectron Spectroscopy Study [J]. *ChemPhysChem*, 2013, **14**, 3332.

[201] B. P. Prascher, D. E. Woon, K. A. Peterson, T. H. Dunning. Jr., and A. K. Wilson. Gaussian

basis sets for use in correlated molecular calculations. VII. Valence, core-valence, and scalar relativistic basis sets for Li, Be, Na, and Mg [J]. *Theoretical Chemistry Accounts*, 2011, **128**, 69.

[202] D. S. Sabirov and E. Osawa. Information entropy of fullerenes [J]. *Journal of chemical information and modeling*, 2015, **55**, 1576.

[203] A. C. Tang, F. Q. Huang, and R. Z. Liu. Electronic structures of fullerenes C_n with I_h symmetry and $n = 20k^2$ [J]. *Physical Review B*, 1996, **53**, 7442.

[204] F. D'Souza and O. Ito. Photosensitized electron transfer processes of nanocarbons applicable to solar cells [J]. *Chemical Society Reviews*, 2012, **41**, 86.

[205] S. Fukuzumi, K. Ohkubo, and T. Suenobu. Long-lived charge separation and applications in artificial photosynthesis [J]. *Accounts of chemical research*, 2014, **47**, 1455.

[206] Y. Kawashima, K. Ohkubo, V. M. Blas-Ferrando, H. Sakai, E. Font-Sanchis, J. Ortíz, F. Fernández-Lázaro, T. Hasobe, Á. Sastre-Santos, and S. Fukuzumi. Near-infrared photoelectrochemical conversion via photoinduced charge separation in supramolecular complexes of anionic phthalocyanines with $Li^+@C_{60}$ [J]. *The Journal of Physical Chemistry B*, 2015, **119**, 7690.

[207] G. von Helden, P. R. Kemper, N. G. Gotts, and M. T. Bowers. Isomers of small carbon cluster anions: linear chains with up to 20 atoms [J]. *Science*, 1993, **259**, 1300.

[208] G. Von Helden, N. G. Gotts, and M. T. Bowers. Experimental evidence for the formation of fullerenes by collisional heating of carbon rings in the gas phase [J]. *Nature*, 1993, **363**, 60.

[209] J. Hunter, J. Fye, and M. F. Jarrold. Annealing C_{60}^+: synthesis of fullerenes and large carbon rings [J]. *Science*, 1993, **260**, 784.

[210] M. A. Wilson, L. S. K. Pang, G. D. Willett, K. J. Fisher, and I. G. Dance. Fullerenes—preparation, properties, and carbon chemistry [J]. *Carbon*, 1992, **30**, 675.

[211] C. H. Kiang. Carbon rings and cages in the growth of single-walled carbon nanotubes [J]. The *Journal of Chemical Physics*, 2000, **113**, 4763.

[212] A. Van Orden and R. J. Saykally. Small carbon clusters: spectroscopy, structure, and energetics [J]. *Chemical reviews*, 1998, **98**, 2313.

[213] S. Arulmozhiraja and T. Ohno. CCSD calculations on C_{14}, C_{18}, and C_{22} carbon clusters [J]. *The Journal of chemical physics*, 2008, **128**, 114301.

[214] T. Heaton-Burgess and W. Yang. Structural manifestation of the delocalization error of density functional approximations: C_{4N+2} rings and C_{20} bowl, cage, and ring isomers [J]. *The Journal of chemical physics*, 2010, **132**, 234113.

[215] K. Remya and C. H. Suresh. Carbon rings: a DFT study on geometry, aromaticity, intermolecular carbon–carbon interactions and stability [J]. *RSC advances*, 2016, **6**, 44261.

[216] J. Lu, S. Re, Y. Choe, S. Nagase, Y. Zhou, R. Han, L. Peng, X. Zhang, and X. Zhao. Theoretical identification of C_{20} carbon clusters: Prevalence of the monocyclic isomer and existence of the smallest fullerene and bowl isomer [J]. *Physical Review B*, 2003, **67**, 125415.

[217] J. M. L. Martin, J. El-Yazal, and J. P. François. On the structure and vibrational frequencies of C_{20} [J]. *Chemical physics letters*, 1996, **248**, 345.

[218] W. An, Y. Gao, S. Bulusu, and X. C. Zeng. Ab initio calculation of bowl, cage, and ring isomers of C_{20} and C_{20}^- [J]. *The Journal of chemical physics*, 2005, **122**, 204109.

[219] W. R. Lee, C. Lee, J. Kang, S. S. Park, Y. G. Hwang, and K. H. Lee. Uptake Effects of Two Electrons for Relative Stability and Atomic Structures of Carbon Cluster Isomers of C_{20}: ab initio Methods [J]. *Bulletin of the Korean Chemical Society*, 2009, **30**, 445.

Bibliography

[220] H. Prinzbach, F. Wahl, A. Weiler, P. Landenberger, J. Wörth, L. T. Scott, M. Gelmont, D. Olevano, F. Sommer, and B. von Issendorff. C_{20} Carbon Clusters: Fullerene–Boat–Sheet Generation, Mass Selection, Photoelectron Characterization [J]. *Chemistry–A European Journal*, 2006, **12**, 6268.

[221] F. Lépine, A. R. Allouche, B. Baguenard, Ch. Bordas, and M. Aubert-Frécon. Computed electron affinity of carbon clusters C_n up to n=20 and fragmentation energy of anions [J]. *The Journal of Physical Chemistry A*, 2002, **106**, 7177.

[222] T. Zimmermann, H. Köppel, and L. S. Cederbaum. On the bilinear vibronic coupling mechanism [J]. *The Journal of chemical physics*, 1985, **83**, 4697.

[223] H. Köppel, F. X. Gadea, G. Klatt, J. Schirmer, and L. S. Cederbaum. Multistate vibronic coupling effects in the K-shell excitation spectrum of ethylene: Symmetry breaking and core-hole localization [J]. *The Journal of chemical physics*, 1997, **106**, 4415.

[224] H. Köppel, W. Domcke, L. S. Cederbaum. Multimode molecular dynamics beyond the Born-Oppenheimer approximation [J]. Advances in chemical physics, 1984, **57**, 246.

[225] L. S. Cederbaum, H. Köppel, and W. Domcke. Multimode vibronic coupling effects in molecules [J]. *International Journal of Quantum Chemistry*, 1981, **20**, 251.

[226] M. Saito and O. Sugino. Vibrational fine structures in photoelectron spectra of carbon ring clusters [J]. *Physical Review B*, 2000, **61**, 12674.

[227] J. D. Watts and R. J. Bartlett. A theoretical study of linear carbon cluster monoanions, C_n^-, and dianions, C_n^{2-} (n= 2–10) [J]. *The Journal of chemical physics*, 1992, **97**, 3445.

[228] M. G. Giuffreda, M. S. Deleuze, and J. P. François. Structural, Rotational, Vibrational, and Electronic Properties of Carbon Cluster Anions C_n^-(n=3−13) [J]. *The Journal of Physical Chemistry A*, 2002, **106**, 8569.

List of Papers

Results presented in this work:

1) Y.-F. Yang, S. Klaiman, E. V. Gromov, and L. S. Cederbaum. Bound Electronic States of the smallest Fullerene C_{20}^{-} anion [J]. *Physical Chemistry Chemical Physics*, 2018, **20**, 17434.

2) Y.-F. Yang, E. V. Gromov, and L. S. Cederbaum. Charge Separated States of Endohedral Fullerene Li@C_{20} [J]. *The Journal of chemical physics*, 2019, **151**, 114306.

3) Y.-F. Yang, E. V. Gromov, and L. S. Cederbaum. Caged-Electron States in Endohedral Li Fullerenes [J]. *The journal of physical chemistry letters*, 2019, **10**, 7617.

4) Y.-F. Yang, and L. S. Cederbaum. Bound States and Symmetry Breaking of the ring C_{20}^{-} anion (in preparation)

Papers published prior PhD:

1) Y.-F. Yang, Z.-H. Cui, and Y.-H. Ding. Bottom-up substitution assembly of $AuF_{4-n}{}^{0,-}$+ n PO_3 (n= 1–4): a theoretical study of novel oxyfluoride hyperhalogen molecules and anions $AuF^{4-n}(PO3)_n^{0,-}$ [J]. *Molecular Physics*, 2014, **112**, 1589.

2) Y.-F. Yang, Z.-H. Cui, and Y.-H. Ding. Structures and electron affinity of $XO_3^{0,-}$, $XOF_4^{0,-}$ and $XO_2F_2^{0,-}$ (X= P, As, Sb, Bi): a theoretical study of novel superhalogen formulae and exceptions of superhalogen formulae [J]. *Molecular Physics*, 2015, **113**, 640.

Eidesstattliche Versicherung gemäß §8 der Promotionsordnung der Naturwissenschaftlichen-Mathematischen Gesamtfakultät der Universität Heidelberg

1. Bei der eingereichten Dissertation zu dem Thema "Electronic States of Fullerenes Anions and Endohedral Fullerenes" handelt es sich um meine eigenständig erbrachte Leistung.

2. Ich habe nur die angegebenen Quellen und Hilfsmittel benutzt und mich keiner unzulässigen Hilfe Dritter bedient. Insbesondere habe ich wörtlich oder sinngemäß aus anderen Werken übernommene Inhalte als solche kenntlich gemacht.

3. Die Arbeit oder Teile davon habe ich bislang nicht an einer Hochschule des In- oder Auslands als Bestandteil einer Prüfungs- oder Qualifikationsleistung vorgelegt.

4. Die Richtigkeit der vorstehenden Erklärungen bestätige ich.

5. Die Bedeutung der eidesstattlichen Versicherung und die strafrechtlichen Folgen einer unrichtigen oder unvollständigen eidesstattlichen Versicherung sind mir bekannt.

Ich versichere an Eides statt, dass ich nach bestem Wissen die reine Wahrheit erklärt und nichts verschwiegen habe.

________________ ________________

Ort, Datum Unterschrift